TECHNISCHE UNIVERSITÄT MÜNCHEN

Lehrstuhl für Biologische Bildgebung

Hybrid Fluorescence Molecular Tomography and X-ray CT
Methods and Applications

Angelica B.F. Ale

Vollständiger Abdruck der von der Fakultät für Elektrotechnik und Informationstechnik der Technischen Universität München zur Erlangung des akademischen Grades eines

Doktors der Naturwissenschaften (Dr. rer. nat.)

genehmigten Dissertation.

Vorsitzender: Univ.-Prof. Dr.-Ing. Eckehard Steinbach
Prüfer der Dissertation:

1. Univ.-Prof. Vasilis Ntziachristos, Ph.D.
2. Univ.-Prof. Dr. rer. nat. Hendrik Dietz

Die Dissertation wurde am 10.11.2011 bei der Technischen Universität München eingereicht und durch die Fakultät für Elektrotechnik und Informationstechnik am 16.04.2012 angenommen.

Abstract

Fluorescence Molecular Tomography (FMT) is a pre-clinical imaging method, aimed at in-vivo visualization of the fluorescence distribution inside small animals. Fluorescence agents that give information on disease biomarkers can be used to deliver insight on disease progression and treatment effects. FMT systems employ a near-infrared laser for illumination and sensitive CCD cameras for light detection. A reconstruction technique is applied in order to recover the 3d fluorescence distribution. The reconstruction is complicated by the scattering and absorbing nature of light in the near-infrared range. Furthermore, FMT offers molecular contrast, but no anatomical reference. In order to improve imaging performance, optical tomography can be complemented with another imaging modality. Combination with X-ray CT (XCT) is a sensible choice because XCT provides anatomical contrast and has construction characteristics similar to fluorescence tomography. A CCD based hybrid FMT system for 360° imaging combined with XCT was built at our institute, offering an accurately co-registered and information-rich hybrid data set, with many new imaging possibilities compared to stand-alone FMT and XCT.

The aim of this work was the development of improved methods for reconstruction of the fluorescence distribution by exploiting the new capabilities of the hybrid FMT-XCT system. We focussed on the development of methods that do not rely on user input and do not bias the solution. This is particularly important in fluorescence tomography, because generally no accurate prior knowledge exists on the fluorescence bio-distribution. We developed a practical method that is applicable under a wide range of experimental conditions.

The developed method uses the X-ray CT information in the forward light propagation model in the form of optical attenuation properties determined for each anatomical region. The inversion method is a two step proce-

dure. In the first step, a reconstruction of the fluorescence distribution is obtained by inverting the forward light propagation model. Based on the result from the first inversion, a set of parameters is defined that are correlated with the amount of fluorescence reconstructed in each anatomical region. These parameters are translated to regularization parameters that build up a structural penalty matrix. In the second step, a sequential inversion of the forward model is performed using the structural penalty matrix, resulting in the reconstruction of the fluorescence distribution. Additionally, the X-ray CT information was used in a pre-processing step in the reconstruction method, in the form of an X-ray CT based background fluorescence subtraction. During post-processing, the X-ray CT information was used to visualize the reconstruction of the fluorescence distribution together with the anatomical information provided by X-ray CT resulting in images with a high information density.

We performed phantom experiments, ex-vivo and in-vivo mouse experiments in parallel with the development of the hybrid methods. Results were validated using invasive post-mortem planar fluorescence imaging. We applied the developed methods to study a subcutaneous breast cancer model, imaged using a variety of fluorescent probes. We show results of two longitudinal studies of cancer progression: a study of a transgenic mouse model of lung cancer and a brain cancer study using fluorescent proteins. We performed an imaging study of an osteogenesis imperfecta mouse model, and finally we describe a study of apoptosis after myocardial infarction.

We observed that besides the benefit of anatomical guidance, the hybrid system resulted in the most accurate FMT performance offered to-date. FMT-XCT is expected to evolve as an important method for delivering advanced XCT and FMT performance. The increased accuracy and contrast that comes with this approach could find diverse biomedical applications in drug development, studying disease growth or observing patho-physiological mechanisms over time.

Contents

1

Introduction

Pre-clinical imaging is aimed at understanding disease progression and development of new drugs and treatments. In pre-clinical imaging studies, animals are imaged, usually mice, serving as a model for human disease. There are many invasive and non-invasive imaging modalities that can be used to investigate a certain disease. Many imaging techniques that are suited for whole-body in-vivo imaging of small animals are derived from clinical methods: Magnetic Resonance Imaging (MRI), in which a magnetic field is applied that affects the magnetic properties of water, Positron Emission Tomography (PET), based on the detection of radiation emitted by an injected radio-isotope, Single Photon Emission Computed Tomography (SPECT), which is similar to PET but uses a different type of radiation, X-ray Computed tomography (X-ray CT) in which X-ray radiation from a source outside of the body is detected on the other side, and Ultrasound (US) that uses sound waves that are reflected by the structures in the body. In this research, we are concerned with a different type of imaging methods: optical imaging, based on light. Optical imaging is a versatile modality which has as advantages that it is less harmful to the body, it does not involve radioactive materials and system components are relatively cheap. In particular, we will use Fluorescence Molecular Tomography, a non-invasive optical imaging method that uses near-infrared fluorescence as agent for detection of specific aspects of a disease [Ntziachristos et al., 2005].

Fluorescence Molecular Tomography (FMT) is a method aimed at in-vivo visualization of the fluorescence distribution inside a small animal, mice in this research. First a fluorescent agent is injected into the mouse. Light in

the near-infrared range (650-950 nm) is directed towards the mouse to excite the fluorochromes. The fluorochromes will subsequently emit photons at a different wavelength (Figure 1.1). The different wavelength makes it possible to detect the fluorescent signal specifically. Light in the near-infrared is used because in this range tissue absorption is minimal and light can penetrate to a considerable depth of max. 6 cm, enough to image mice, which have a diameter of about 2 cm.

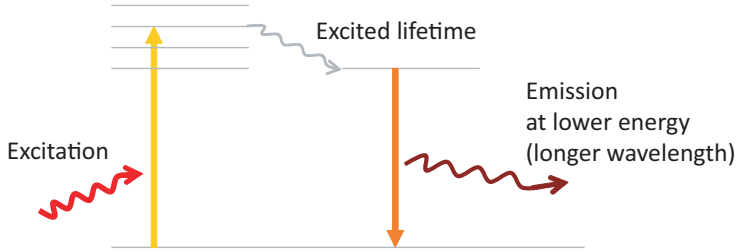

Figure 1.1: Principle of fluorescence. The laser excites the fluorescent agent. After the fluorescence lifetime, the fluorescent agent emits photons at a longer wavelength.

The fluorescent agents can be used to monitor biological processes inside the mouse. The simplest type of agents are the fluorescent dyes. After injection they will circulate through the bloodstream and give general information on for example the distribution of the dye through the body and about the vasculature. Disease specific information can be obtained when the fluorophore is connected to another substance that targets a biological element, this combination is termed a fluorescent probe. Fluorescent probes can target for example elements that are on the outer surface of only certain cells that play a role in disease, such as cancer cells, or they can target other components that accumulate for example in case of an inflammation. A most sophisticated group of agents are the fluorescent proteins. These agents involve modified cells that can produce a fluorescent protein. This approach can be used to visualize almost any type of cell [Weissleder and Ntziachristos, 2003].

A difficulty of imaging in the near-infrared range is that the light is diffused by the tissue [Jacques and Pogue, 2008]. Unlike for example X-ray imaging, where the light travels along almost straight lines through the tissue, and a projection of the inside is directly visible, in the near-infrared range light is scattered and absorbed underway (Figure 1.2). We will denote the degree of scattering and absorption in the medium as optical properties in

the following. In order to overcome the difficulties associated with diffusion, the technique has evolved from systems based on epi-luminescence geometries to full 360 degree trans-illumination systems with CCD camera based detection.

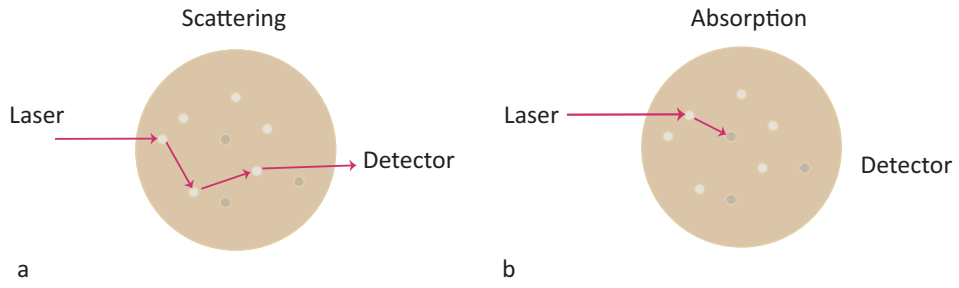

Figure 1.2: Light in the near-infrared range suffers from a) scattering and b) absorption.

In epi-illumination setup (see Figure 1.3) source and detector are at the same side of the subject. With this setup, light from fluorescent sources that are a few millimeters under the skin can be captured. Drawbacks of

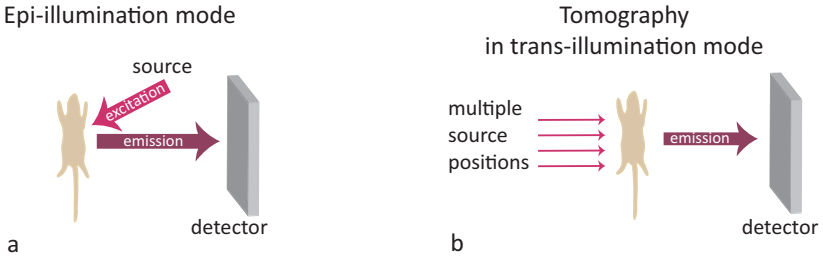

Figure 1.3: Fluorescence imaging setups. a) Epi-illumination. b) Tomography in trans-illumination mode.

epi-illumination setups are the difficulty of distinguishing between depth and signal strength, and due to the limited penetration depth it can only resolve fluorescent sources that are close to the surface at the side from which the mouse is imaged. More information on the subject is obtained from an acquisition setup in trans-illumination mode, in which source and detector are placed on different sides of the subject and light is measured that has penetrated the complete animal. The optimal setup for fluorescence imaging is tomography in trans-illumination mode, in which the subject is illumi-

nated from multiple source positions and from multiple sides. This makes it possible to resolve the 3d inside fluorescence distribution in the subject, by combining all data from different angles [Ntziachristos, 2006].

Early systems for fluorescence tomography used fibers to direct the light towards the mouse and fibers to detect the light as well, while the mouse was submersed in a chamber filled with a fluid with the same optical properties as the mouse. This resulted in a limited amount of source and detector combinations that could be used to acquire data. In order to be able to obtain as much information as possible, the systems evolved towards free-space technology, where the source fibers were replaced by collimated laser beams, and the detector fibers were replaced by a CCD camera. The positioning of the mouse in the free-space systems has evolved as well (Figure 1.4). At

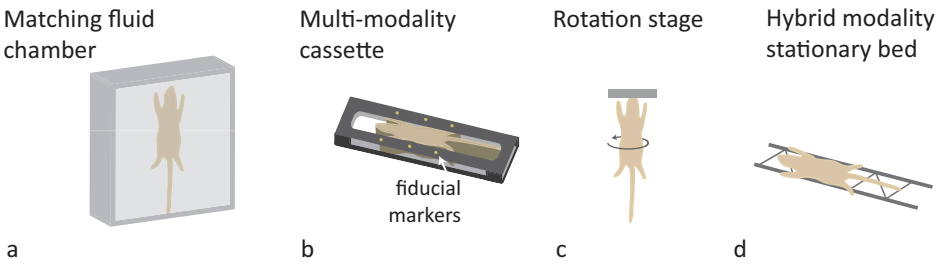

Figure 1.4: Free space mouse positioning development. a) Imaging chamber with matching fluid. b) Multi-modality cassette. c) Rotational stage for 360 degree illumination. d) Mouse bed with strings for 360 degree illumination.

first the mouse was submersed in a rectangular chamber with a matching fluid, such that the mouse could be modelled as a rectangular slab [Graves et al., 2003]. In a commercially available system for FMT (FMT2500, VisEN Medical), the mouse is placed in an imaging chamber, which also enables slab modelling. Free-space implementations have used a rotational stage that could rotate the mouse 360 degrees, such that much more information could be obtained. The last image shows the mouse bed of the system that we will describe below. In this case the instrumentation rotates around the bed, while the mouse can stay relatively comfortable in a natural position on the mouse bed. The improvements in system configuration enabled FMT to deliver molecular contrast with sub-millimeter resolution [Ntziachristos et al., 2005; Deliolanis et al., 2009; Ntziachristos, 2010; Leblond et al., 2010],

and has demonstrated quantification and volumetric imaging performance superior to epi-illumination imaging [Ntziachristos et al., 2002a,b; Kepshire et al., 2009b; Milstein et al., 2003; Baeten et al., 2009].

A typical acquisition sequence in fluorescence molecular tomography consists of three steps, 1) acquisition of a white light image of the mouse, 2) a measurement of the light transmitted at the excitation wavelength, and 3) a measurement of the light transmitted at the fluorescence wavelength. The measurements at different wavelengths can be obtained by placing different filters in front of the CCD camera. In Figure 1.5 a set of acquisition images is displayed. The white light image is used to position the laser source. The emission (fluorescence) image shows the signal from the fluorescent agent, in this case a fluorescent dye in the lungs of the mouse. The excitation image shows the light distribution through the mouse. The excitation measurement can be used to normalize the emission data for the light distribution (normalized=emission/excitation), and reduce background signals and noise. In Figure 1.5d, the effect of the normalization is visible, compared to Figure 1.5b it is much more apparent that the fluorescence signal is coming from the lung area. The acquired normalized images are used to reconstruct the fluorescence distribution inside the mouse. The reconstruction consists mainly of modelling the light propagation through the mouse, and inverting the model to find an estimate of the fluorescence distribution that matches the acquisition data.

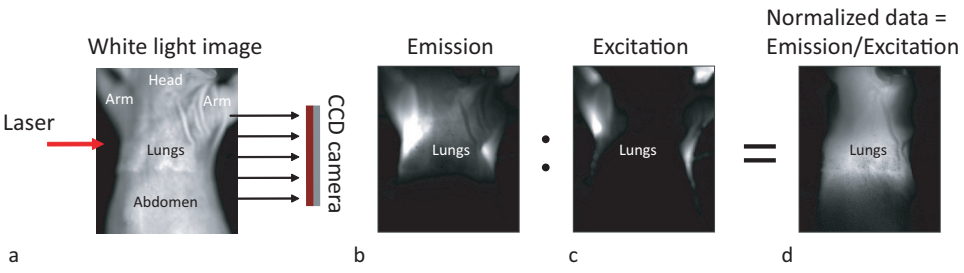

Figure 1.5: A measurement consists of three acquisition steps: Acquisition of a) a white light image for source placement, b) the excitation image at the wavelength of the laser, and c) the emission image at the wavelength of the fluorochrome. The normalized image (d) is used as input for the reconstruction.

Due to photon diffusion in tissue as described above, FMT resolution is limited to about 1 mm which varies with tissue depth and is affected by

the spatial heterogeneity of tissue optical properties. Another limitation of FMT is that it does not provide any anatomical information that could indicate the exact location of the recovered fluorescence signals. A promising direction for further improvement of the performance of FMT is the combination with another imaging modality, preferably a high resolution modality. The second imaging modality could deliver different contrast and at the same time reduce the complexity of the optical tomography inverse problem and improve its imaging performance [Chang et al., 1997; O'Leary et al., 1996]. The suggestion of hybrid imaging is not unique to optical tomography [Cherry, 2009; Giovanella and Lucignani, 2010]. The combination of Positron Emission Tomography (PET) and X-ray Computed Tomography (XCT) [Riklund, 2010; Freudenberg et al., 2007; Levine and Julian, 2009; Nahrendorf et al., 2008; Kaufmann and Di Carli, 2009; Kinahan et al., 2003] or Single Photon Emission Computed Tomography (SPECT) and XCT [Golestani et al., 2010; Bockisch et al., 2009; Townsend, 2008] are widely utilized examples of hybrid imaging today whereas hybrid Magnetic Resonance Imaging (MRI) and PET have also been recently developed [Judenhofer et al., 2008; Wehrl et al., 2010].

The first step in combining FMT with another modality was co-registration: the registration of two data-sets with two systems, that are afterwards combined. Ntziachristos et al. [Ntziachristos et al., 2005; Ntziachristos, 2009] co-registered FMT in trans-illumination with MRI, and used the MRI anatomical information to localize a fluorescent signal. The next step in combining imaging systems was the development of multi-modality cassettes that can be used to acquire data with multiple systems, while keeping the animal in place and facilitating co-registration by the use of fiducial markers (Figure 1.4b). The latest development in FMT systems is the development of hybrid systems, in which FMT is combined with another modality in one single housing.

The most straightforward benefit of truly hybrid systems over a combination of stand-alone modalities is the seamless co-registration of images, which facilitates the accurate superposition of information content. Accurate co-registration comes with two major benefits. First, it allows the fusion of the images produced by the two modalities, so that a hybrid image is generated that contains higher information, for instance molecular activity obtained from one modality superimposed on an anatomical image from another,

which allows better understanding on the exact location of the molecular activity. Second, a hybrid system allows for improving the images from one modality based on information obtained from the other modality. In PET-XCT systems for example, the PET accuracy and resolution is improved by using high energy (511-keV) photon attenuation maps calculated from the XCT images [Kinahan et al., 2003]. Compared to PET or SPECT, the use of attenuation correction concepts in optical imaging of diffuse media can lead to significantly higher imaging performance improvements. This is because, compared to the high energy modalities, near-infrared photons are affected more strongly by tissue optical properties; therefore anatomically guided correction can lead to more substantial improvements over stand-alone implementations.

In response, several methods have been suggested to consider the use of anatomical information as a form of prior information, in order to improve optical tomography of tissues [Intes et al., 2004; Guven et al., 2005; Srinivasan et al., 2004; Hiltunen et al., 2008; Yalavarthy et al., 2007b] and correspondingly different scanners were developed to facilitate such improvement. Ntziachristos et al. [2000] described a hybrid MRI - time-resolved system employed for clinical breast cancer imaging. Zhang et al. [2005] described a frequency domain optical imaging system, integrated with a tomosynthesis digital mammography system whereas Davis et al. [2008] developed a spectrometer-based tomographic imaging system coupled with MRI. Other hybrid systems have been reported as well, including a fiber-based fluorescence tomography system coupled with micro-CT [Kepshire et al., 2009a]. Generally, previous systems employed fiber based detection in order to allow an adaptation of the optical measurements in existing XCT or MRI systems. However, the use of fibers reduces the number of measurements available to the optical inversion method. Mathematically this can be described as an incomplete data set since it does not sample all the spatial frequencies available to the measurement. This under-sampling may significantly compromise the optical imaging performance by worsening the ill-posed nature of the inverse problem. For this reason, a hybrid FMT-XCT system was recently engineered to eliminate compromises in the optical detection.

The system that we used for all imaging studies in this research was a prototype hybrid FMT and XCT system that was developed at our institute [Schulz et al., 2010]. The system was the first available prototype worldwide

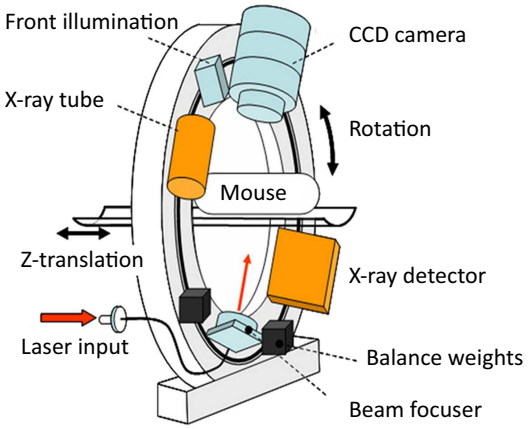

Figure 1.6: Design of the hybrid FMT-XCT prototype.

that integrated FMT and XCT into one hybrid system. It was developed as part of the European Project FMT-XCT FP7 (www.fmt-xct.eu). The design of the system (Figure 1.6), shows a rotating gantry onto which all instrumentation is mounted: free-space X-ray CT instrumentation on one axis of the gantry, and free-space FMT instrumentation on the axis perpendicular to it, both in trans-illumination set-up. The materialization of the design in the first prototype is shown in Figure 1.7. The basis of the system was a commercial micro-CT system (eXplore Locus, GE HealthCare), which had a rotating gantry with an outer diameter of ≈1 m. Full 360° data sets could be acquired for both modalities. Two acquisition sequences were implemented: simultaneous FMT and XCT acquisition during one rotation of the gantry, and sequential acquisition of FMT and XCT data using two rotations of the gantry. In most experiments we employed the sequential acquisition mode, mainly because of the limited flexibility of the X-ray CT acquisition software. The field of view of the XCT image was approximately 8 cm by 3.5 cm. The resolution of the reconstructed XCT volume was set to 95 μm.

FMT illumination consisted of two diode laser sources with a wavelength of respectively 680 nm and 750 nm (B&W Tek, Newark, DE, USA). Detection of the optical signal was performed using a back-illuminated CCD camera with a field of view consisting of 512 x 512 pixels, cooled to -70° for optimal sensitivity. Configuration of the acquisition included the selection of a number of desired projection angles with set increments and the distance between sources in transversal and longitudinal direction. The ac-

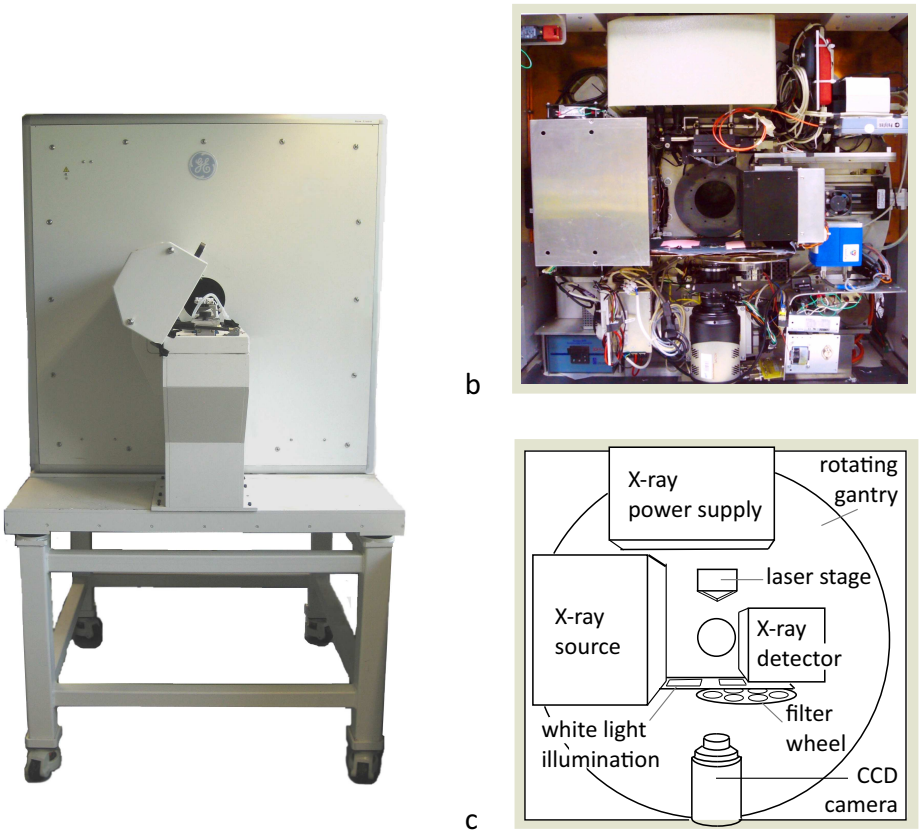

Figure 1.7: Hybrid FMT-XCT prototype. a) External view of the hybrid FMT-XCT system housing. The cover that enables mouse placement is opened. b) Photograph of the instrumentation inside the hybrid FMT-XCT system. c) Schematic of the instrumentation, main components are indicated.

quisition sequence started by rotating the gantry to the desired projection angle (Figure 1.8), after which one white light image of the mouse was acquired. An automatic routine was implemented to determine the boundaries of the mouse based on the white light image, which were used to center the defined source pattern along the middle of the mouse. Subsequently images at excitation and emission wavelength were acquired. Electromechanical linear stages (Thorlabs, Newton, NJ, USA) were used to scan a system of lenses so that a collimated laser beam could be mildly focused at each desired source position. Spectral selection was based on a six-position filter wheel positioned in front of the CCD camera lens with filters for excitation and emission wavelengths. For each source position in the grid, the laser power was set to an optimal value for the acquisition of the excitation image using

automatic gain control (AGC) in order to maximize the dynamic range of the system. After acquiring the excitation image, the laser power was kept constant and the emission image was acquired. The illumination time for the emission image was increased depending on strength of the fluorescence signal to a maximum of around 6 seconds. Each source position generated 2 x 512 x 512 data pairs, considering the 512 x 512 independent detectors established by the CCD camera and the two spectral measurements performed per fluorochrome. Total scan times were determined by the number of source positions; for a typical 18 projection FMT acquisition, collecting 15 source positions, ≈25 minute scans could be obtained, whereas the scan time for 21 source positions was close to 1 hour.

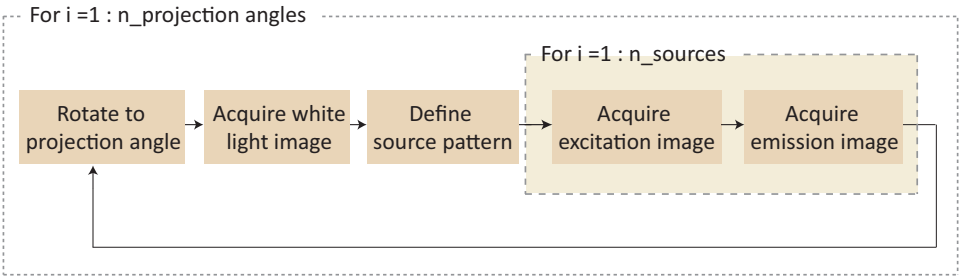

Figure 1.8: Flowchart of main steps in the FMT acquisition sequence.

We validated the performance of the non-invasive FMT-XCT system by comparing reconstruction results with invasive ex-vivo imaging. The main validation modality used in this work was planar ex-vivo imaging of slices of the mice with the cryoslicer, a multispectral epi-fluorescence system developed at our institute [Sarantopoulos et al., 2011]. The cryoslicer was a combination of a cryostat and a planar imaging system, consisting of a white light source and a sensitive CCD camera in epi-illumination setup. Motorized filter wheels were placed in front of the CCD camera for wavelength selection. It could take slices of mice that were frozen to -80° and embedded in O.C.T. (Optimal Cutting Temperature) medium, and for each slice acquire three types of planar images: RGB images, images at the excitation wavelength and images at the emission wavelength. Additional validation was performed by histological H&E staining of slices obtained with the cryoslicer, providing information at the cellular level. After H&E staining (Hematoxylin and Eosin) of a slice, nuclei of cells are colored blue, and other structures are colored in red, pink or orange. The H&E stained slices were

imaged using a Leica microscope and using a Leica Z16 macroscope that was part of a high-resolution zoom camera system that is currently under development at our institute by Karin Radrich.

1.1 Objectives and outline

The aim of this work was the development of methods for reconstruction of the fluorescence distribution inside small animals by using the new capabilities of the hybrid FMT-XCT system to full potential. The hybrid system opened up many possibilities for improvement of the FMT image quality by using data from both the FMT and X-ray CT modality. We followed an experimental approach. We performed ex-vivo and in-vivo mouse experiments in parallel with development of hybrid methods, and incorporated the experience gained from animal experiments in the development. This approach is different from a more theoretical approach that is based on simulations and phantom experiments with evaluation on in-vivo experiments after the development. With this experimental approach, we could deal directly with reconstruction problems that are encountered when using real data from actual in-vivo experiments. We developed a practical method that is applicable under a wide range of experimental conditions. Of particular interest was the use of both FMT and X-ray CT information in the same inversion scheme, in order to achieve optimal performance of the optical method. We developed a data-driven method in order to avoid user-introduced bias. We validated all reconstruction developments against ex-vivo cryoslicing, in order to ensure reliability of the results and correctness of the methods.

In **Chapter 2**, we give an overview of FMT methods, including background theory on the light propagation model and inversion techniques. **Chapter 3** describes the acquisition of hybrid FMT-XCT data. It is very important to obtain useful acquisition data, in order to be able to perform a good inversion. **Chapter 4** describes the inversion method that we used in detail. The first element of the reconstruction method that we investigated was the use of a structural penalty matrix that is based on the anatomical segmentation of the X-ray CT data. We considered several different implementations, and finally selected the penalty matrix that displayed the most consistent and robust performance for the largest application range. The selected structural penalty matrix was based on a set of weights corresponding to anatomical segments. In order not to bias the solution, we developed a data driven method for the calculation of these weights. Several approaches for the data

driven calculation were evaluated. **Chapter 5** describes the second element that we investigated in more detail: the use of prior information in the forward light propagation model by assigning different attenuation coefficients to different anatomical regions. We determined the optical coefficients for the thorax area and for the brain region, and these values were used for the reconstruction of corresponding animal studies. In order to increase the sensitivity of the reconstruction method in cases of a high level of background fluorescence, we implemented a background fluorescence correction based on the X-ray CT data, described in **Chapter 6**. We performed several phantom and mouse experiments to evaluate the quantitative performance of the implemented methods, described in **Chapter 7**.
In **Chapter 8** we apply the developed methods to several animal studies. We show results of studies involving cancer: a study of a 4T1 breast cancer model in combination with three different fluorescent probes, a longitudinal study of lung cancer progression in a genetically modified mouse model and imaging of brain cancer progression using fluorescent proteins. Additionally we show results of a mouse model of Osteogenesis Imperfecta, a disease that causes bones to break easily, and a study of apoptosis (cell death) after myocardial infarction.

2

FMT - forward model and inversion

2.1 Introduction

In this chapter, we outline the main steps in the estimation of the fluorescence distribution in FMT. The acquired FMT data (see also Chapter 3) consists of 2d images of light that was transmitted from a laser source through the imaged object and captured with the camera. Our aim is to find the 3d fluorescence distribution inside the object, based on the measured data. The estimation of the fluorescence distribution consists of two main steps: 1) forward modelling the light propagation through the object, and 2) inverting the forward model. We first describe the forward light propagation model that is often used in Fluorescence Molecular Tomography based on the diffusion equation in Section 2.2. In Section 2.3 we describe the inversion of the forward model. We introduce a certain class of inverse problems, the so-called ill-posed problems. The iterative method that we used for inversion is described as well. We used prior information to improve the estimation of the fluorescence distribution, this will be described in detail in later chapters.

2.2 Forward light propagation model

In order to obtain an accurate quantitative estimate of the fluorescence distribution, we employ a physical model of light propagation through tissue. In fluorescence tomography there are two sources of light with different fre-

quencies: the light source that is used to excite the fluorescent agent and the fluorescent agent that emits photons after being excited. In this research both light sources have wavelengths in the near-infrared range. As was described in Chapter 1, the light in this wavelength range is absorbed and scattered by the tissue and becomes diffuse within less than a millimeter. In the following, the absorption coefficient μ_a in [cm^{-1}] expresses absorption of photons and the scattering coefficient μ_s in [cm^{-1}] expresses the degree of scattering in the medium.

An accurate model for describing photon propagation in diffuse media is the radiative transfer model. Because the radiative transfer model is computationally intensive, we use an approximation to the radiative transfer model, the diffusion approximation [Arridge, 1999; Jacques and Pogue, 2008], which is often used for biomedical imaging. The diffusion approximation is valid when light propagation is nearly isotropic. In biological tissue, this approximation is assumed to hold because of the high scattering properties of tissue. The tissue has to be of sufficient thickness and the approximation holds after at least one scattering event has taken place [Ntziachristos et al., 2007].

The diffusion approximation can be derived from the principle of conservation of energy in a volume V:

$$\underbrace{\int_V \frac{1}{c}\frac{\partial \phi(\mathbf{r},t)}{\partial t} dV}_{change\ in\ V} = \underbrace{\int_{\partial V} \mathbf{j}(\mathbf{r},t)\cdot \hat{n} dS}_{flow} + \underbrace{\int_V (-\mu_a(\mathbf{r})\phi(\mathbf{r},t) + S(\mathbf{r},t) dV}_{production}. \tag{2.2.1}$$

The first term represents the change of the energy density, with $\phi(\mathbf{r},t)$ in [W cm^{-2}] the fluence rate at a position $\mathbf{r}$ in the medium, which expresses for a given point in space, the power incident on a small sphere divided by the cross-sectional area of the sphere, and c [cm s^{-1}] is the speed of light in the medium. The second term represents the flow of energy through the boundary ∂V of the volume, obtained from the inner product of the flux density vector $j(\mathbf{r},t)$ in [W cm^{-2}] and the direction $\hat{n}$ normal to the surface, integrated over the surface of the volume. The last term represents the production of energy, consisting of an absorption term, integrating $\mu_a(\mathbf{r})$ multiplied with the fluence rate over the volume, and a production term, in which $S(\mathbf{r},t)$ [W cm^{-3}], the power per unit volume produced by the sources, is integrated over the volume. The expression for an arbitrary volume is

found after applying Gauss' theorem to the surface integral:

$$\frac{1}{c}\frac{\partial\phi(\mathbf{r},t)}{\partial t} = -\nabla\mathbf{j}(\mathbf{r},t) - \mu_a(\mathbf{r})\phi(\mathbf{r},t) + S(\mathbf{r},t). \tag{2.2.2}$$

We now introduce Fick's law, which provides a description of the diffusion process:

$$\mathbf{j}(\mathbf{r},t) \approx -D(\mathbf{r})\nabla\phi(\mathbf{r},t). \tag{2.2.3}$$

The diffusion coefficient $D(\mathbf{r})$ can be estimated from the absorption and reduced scattering coefficient, making $D(\mathbf{r})$ space dependent,

$$D(\mathbf{r}) = \frac{1}{3[\mu_a(\mathbf{r}) + \mu_s'(\mathbf{r})]}. \tag{2.2.4}$$

The anisotropy in the medium g is incorporated in the reduced scattering coefficient $\mu_s'(\mathbf{r})$:

$$\mu_s'(\mathbf{r}) = (1-g)\mu_s(\mathbf{r}). \tag{2.2.5}$$

For isotropic media, $g = 0$, for biological tissue g is usually assumed to have a value around $g \approx 0.9$. Because in tissue scattering generally outweighs absorption by two orders of magnitude, the dependence of the diffusion coefficient on the absorption coefficient is often omitted.

Substituting Fick's law in Eq. 2.2.2 leads to an inhomogeneous diffusion equation [Patterson et al., 1989]:

$$\frac{1}{c}\frac{\partial\phi(\mathbf{r},t)}{\partial t} = \nabla D(\mathbf{r})\nabla\phi(\mathbf{r},t) - \mu_a(\mathbf{r})\phi(\mathbf{r},t) + S(\mathbf{r},t). \tag{2.2.6}$$

In steady state, the diffusion equation becomes:

$$-\nabla D(\mathbf{r})\nabla\phi(\mathbf{r}) + \mu_a(\mathbf{r})\phi(\mathbf{r}) = S(\mathbf{r}), \tag{2.2.7}$$

where $S(\mathbf{r})$ is the source term. For fluorescence imaging a set of two coupled diffusion equations is used. The first equation describes light propagation from a source S at a position $\mathbf{r}_s$ into the medium, at a wavelength ex that will excite a fluorochrome,

$$-\nabla D(\mathbf{r})\nabla\phi_{ex}(\mathbf{r}) + \mu_a(\mathbf{r})\phi_{ex}(\mathbf{r}) = S\delta(\mathbf{r}-\mathbf{r}_s), \tag{2.2.8}$$

and the second equation, describes the propagation of light emitted by the fluorochrome at the emission wavelength em:

$$-\nabla D(\mathbf{r})\nabla\phi_{em}(\mathbf{r}) + \mu_a(\mathbf{r})\phi_{em}(\mathbf{r}) = O(\mathbf{r})\phi_{ex}(\mathbf{r}), \tag{2.2.9}$$

where $O(\mathbf{r})$ accounts for the fluorescent source distribution.
Because $\phi_{ex}(\mathbf{r}) \gg \phi_{em}(\mathbf{r})$, we use the first-order Born approximation [Kak and Slaney, 2001] and write the following solution for the scattered field:

$$\phi_{em}(\mathbf{r}_d, \mathbf{r}_s) = \int G_{em}(\mathbf{r}_d, \mathbf{r}) O(\mathbf{r}) \phi_{ex}(\mathbf{r}, \mathbf{r}_s) \mathbf{dr}, \tag{2.2.10}$$

where $G_{em}(\mathbf{r}_d, \mathbf{r})$ is the Green's function solution to the diffusion equation that describes the light propagating from the fluorescent source at $\mathbf{r}$ to the detector at $\mathbf{r}_d$. Equation 2.2.10 represents the fluorescence measurement. For fluorescence tomography, Ntziachristos and Weissleder [2001] further developed this equation into the normalized Born approximation. Fluorescence measurements can always be referenced to excitation measurements obtained under identical experimental characteristics by use of different filter sets (see Chapter 1). In the normalized Born approximation, Equation 2.2.10 is divided by a measurement at the emission wavelength:

$$\frac{\phi_{em}(\mathbf{r}_d, \mathbf{r}_s)}{\phi_{ex}(\mathbf{r}_d, \mathbf{r}_s)} = \frac{\Theta}{\phi_{ex}(\mathbf{r}_d, \mathbf{r}_s)} \int G_{em}(\mathbf{r}_d, \mathbf{r}) n(\mathbf{r}) \phi_{ex}(\mathbf{r}, \mathbf{r}_s) \mathbf{dr}, \tag{2.2.11}$$

where Θ is a constant that accounts for system related factors, and $n(\mathbf{r})$ accounts for the fluorescence distribution. This normalization eliminates instrumentation related effects such as varying source intensities and detector sensitivities, and reduces the sensitivity of the reconstruction for errors in the optical properties that are used for forward model calculation [Soubret et al., 2005].

Analytical formulations of the Green's functions can be obtained under certain conditions. For example, when the source is a delta pulse $S(\mathbf{r}) = S\delta(\mathbf{r} - \mathbf{r}_s)$, optical properties are assumed to be homogeneous and the volume is infinite, the homogeneous solution to the diffusion equation can be written as:

$$\phi(|\mathbf{r} - \mathbf{r}_s|) = S \frac{e^{-\sqrt{\frac{\mu_a}{D}}|\mathbf{r}-\mathbf{r}_s|}}{4\pi D |\mathbf{r} - \mathbf{r}_s|}. \tag{2.2.12}$$

In this work, we are mainly concerned with inhomogeneous finite media and therefore the Green's functions are calculated numerically, using the Finite Element Method. The volume that needs to be modelled consists in reality of an infinite number of points inside the volume, and thus an infinite number of unknowns. Using the Finite Element Method [Huebner, 2001], the number of unknowns is decreased to a finite number by discretizing the volume in a finite number of elements. These elements can have arbitrary

shapes and are connected to each other by nodes, together forming the Finite Element Mesh. In this work the elements in the mesh had a cubical base shape, which were stretched and deformed to fit the shape of the imaged object. The values of the variables, in our case the photon fluence, were calculated only for the nodes and interpolated over the element using a predefined interpolation function. In this way the number of unknowns is reduced to the number of nodes. The Finite Element Method implementation was based on the Deal II framework [Bangerth et al., 2007]. After calculation of the node-based forward model, the nodes were mapped to cubic volume elements, which further reduced the amount of variables.

Using the discretizations described above, we obtain a linear expression for the forward model. The volume Ω that will be reconstructed is discretized in a number of cubic volume elements, termed voxels. For one source-detector pair this is formulated as:

$$\frac{\phi_{em}\left(\mathbf{r}_d, \mathbf{r}_s\right)}{\phi_{ex}\left(\mathbf{r}_d, \mathbf{r}_s\right)} = \sum_{\Omega} \left[\frac{G_{em}\left(\mathbf{r}_s, \mathbf{r}\right) G_{ex}\left(\mathbf{r}, \mathbf{r}_d\right)}{G_{ex}\left(\mathbf{r}_s, \mathbf{r}_d\right)} \Delta V \right] n\left(\mathbf{r}\right). \tag{2.2.13}$$

The right hand side is a sum over the voxels, $G_{ex}(\mathbf{r}_s, \mathbf{r})$ represents the Green's function describing the light propagating at the excitation wavelength from source position $\mathbf{r}_s$ to position $\mathbf{r}$ inside the volume, $G_{em}(\mathbf{r}, \mathbf{r}_d)$ the light propagation at the emission wavelength, and $G_{ex}(\mathbf{r}_s, \mathbf{r}_d)$ is the normalization term. The size of the voxels is included by the term ΔV and $n(\mathbf{r})$ is the unknown fluorochrome distribution.

2.3 Inversion of the forward model

An estimate of the unknown fluorescence distribution inside the medium can be found by inverting the forward model. For the total number of source-detector pairs (N_{data}), the linear expression 2.2.13 can be written as:

$$\mathbf{y} = \mathbf{W}\mathbf{x}. \tag{2.3.14}$$

The model matrix $\mathbf{W}$ is the discretization of the diffusion equation. The imaged object is divided in a finite number of voxels N_{voxels}, and the measured images are discretized in a number of data points. The raw images have 512×512 pixels, using all the pixels as data points would result in a huge data set that is not easy to process with a regular computer. Therefore we average over several pixels, resulting in a smaller number of data

points N_{data}. The model matrix $\mathbf{W}$ now constitutes a rectangular matrix of size $(N_{data} \times N_{voxels})$, the 3d fluorescence distribution $\mathbf{x}$ is a vector of size $(1 \times N_{voxels})$ and the data $\mathbf{y}$ is a vector of size $(1 \times N_{data})$, with $N_{data} > N_{voxels}$. There are two main difficulties in the FMT inversion problem: the data contains noise, and the problem is ill-posed.

The measurement data does not exactly correspond to our model, but contains for example noise introduced by the acquisition system. We can incorporate such deviations in Equation 2.3.14 by including a noise term $\mathbf{n}$:

$$\mathbf{W}\mathbf{x} + \mathbf{n} = \mathbf{y}. \tag{2.3.15}$$

The noise term makes it more difficult to find the fluorescence distribution $\mathbf{x}$, because we generally do not know $\mathbf{n}$ exactly. The second reason that the problem is difficult to solve is that it is ill-posed. A problem is called well-posed if it satisfies a set of conditions by Hadamard [1923], which in a simplified formulation can be stated as:

[1] a solution exists

[2] the solution is unique

[3] the inverse mapping is continuous

In case condition 1 does not hold, multiplication of $\mathbf{W}$ with any $\mathbf{x}$ will not result in $\mathbf{y}$. In case condition 2 does not hold, multiplication of $\mathbf{W}$ with $\mathbf{x}$ can result in $\mathbf{y}$, but multiplication with a different $\mathbf{x}$ can also result in $\mathbf{y}$. In case condition 3 does not hold, a small change in $\mathbf{y}$ may result in a big change in $\mathbf{x}$. A problem is called ill-posed if it is not well-posed. Our problem is ill-posed because due to diffusion, multiple photon paths can lead to the same acquisition data, so that condition 2 does not hold. Furthermore, condition 3 does not hold because a small change in the data can cause a large change in the estimate of the fluorescence distribution. The fact that our problem is ill-posed does not mean that we can not find a meaningful solution.

In the following we first describe the Singular Value Decomposition, which is an important tool for analyzing ill-posed problems. We describe a method to reduce the ill-posedness of the inversion by regularization. And finally we outline the iterative algorithm that we used for inversion, the LSQR algorithm.

2.3.1 Singular Value Decomposition

An inverse problem can be analyzed using the Singular Value Decomposition (SVD). An explicit generalized inverse $\mathbf{A}^\dagger$ of any matrix $\mathbf{A}$ can be calculated using the SVD. The SVD of a rectangular matrix $\mathbf{A}$ of size $(m \times n)$ results in the following decomposition:

$$\mathbf{A} = \mathbf{U}\mathbf{\Sigma}\mathbf{V}^T, \tag{2.3.16}$$

where $\mathbf{U}$ is an $(m \times m)$ orthogonal matrix, $\mathbf{\Sigma}$ is an $(m \times n)$ diagonal matrix with non-negative numbers on the diagonal, and $\mathbf{V}^T$ denotes the transpose of the orthogonal matrix $\mathbf{V}$ of size $(n \times n)$. The SVD is found by calculating the eigenvalues and eigenvectors of the square normal matrices $\mathbf{A}^T\mathbf{A}$ of size $(n \times n)$ and $\mathbf{A}\mathbf{A}^T$ of size $(m \times m)$. The square roots of the eigenvalues of $\mathbf{A}^T\mathbf{A}$ are called the singular values σ_i, these are placed in descending order on the diagonal of $\mathbf{\Sigma}$. The eigenvectors $\mathbf{v}_i$ of $\mathbf{A}^T\mathbf{A}$ form the matrix $\mathbf{V}$, and the eigenvectors $\mathbf{u}_i$ of $\mathbf{A}\mathbf{A}^T$ form the matrix $\mathbf{U}$. $\mathbf{U}$ and $\mathbf{V}$ are orthogonal matrices: the transpose of the matrix is equal to the inverse: $\mathbf{U}^T = \mathbf{U}^{-1}$ and $\mathbf{V}^T = \mathbf{V}^{-1}$. We can now form the inverse of the matrix based on the SVD:

$$\mathbf{A}^\dagger = \left(\mathbf{U}\mathbf{\Sigma}\mathbf{V}^T\right)^{-1} = \left(\mathbf{V}^T\right)^{-1}\mathbf{\Sigma}^{-1}\mathbf{U}^{-1} = \mathbf{V}\mathbf{\Sigma}^{-1}\mathbf{U}^T. \tag{2.3.17}$$

A solution to the inverse problem $\mathbf{x} = \mathbf{A}^\dagger\mathbf{b}$ in terms of the SVD can be written as:

$$\mathbf{x} = \sum_{i=1}^{k} \frac{\mathbf{u}_i^T\mathbf{b}}{\sigma_i}\mathbf{v}_i, \tag{2.3.18}$$

where k is the rank of $\mathbf{A}$ (the rank is equal to the number of non-zero singular values). In case the data contains noise ($\mathbf{b} = \mathbf{b}_{true} + \mathbf{n}$), the solution can be written as:

$$\mathbf{x} = \sum_{i=1}^{k} \left(\frac{\mathbf{u}_i^T\mathbf{b}_{true}}{\sigma_i} + \frac{\mathbf{u}_i^T\mathbf{n}}{\sigma_i} \right) \mathbf{v}_i. \tag{2.3.19}$$

The solution contains the singular values in the denominator, this indicates that small singular values have a large influence on the solution. It is often observed that the basis vectors $\mathbf{u}_i$ and $\mathbf{v}_i$ show oscillatory behavior that is related to the size of the singular values. Large singular values correspond to smooth basis vectors, while small singular values correspond to basis vectors with many zero crossings. The small singular values amplify the high frequency components of the noise in the data vector [Hansen, 1998; Tan and Jiang, 2008].

2.3.2 Regularization techniques

When there are many small singular values, the problem becomes underdetermined: there is not enough information to obtain a unique solution. In our model matrix, the singular values gradually decay towards zero. We need to use regularization in order to obtain a reliable estimate of $\mathbf{x}$. The aim of regularization is to stabilize the solution, and to choose a meaningful solution out of the many possible solutions [Hansen, 1998]. This is achieved by including additional information on the solution in the inversion problem, such as that the solution should be smooth, or it should not contain very large peaks which are generated by noise. Instead of trying to find a solution that exactly matches the noisy data, we allow a certain residual and minimize the difference between $\mathbf{Ax}$ and $\mathbf{b}$, without making it exactly zero:

$$\min \|\mathbf{Ax} - \mathbf{b}\|^2 . \tag{2.3.20}$$

Additionally, we apply a well known type of regularization called Tikhonov regularization, which takes the form:

$$\min \underbrace{\|\mathbf{Ax} - \mathbf{y}\|^2}_{\text{residual}} + \lambda^2 \underbrace{\|\mathbf{Lx}\|^2}_{\text{norm}} . \tag{2.3.21}$$

This is equivalent to solving:

$$\min \left\| \begin{bmatrix} \mathbf{A} \\ \lambda \mathbf{L} \end{bmatrix} \mathbf{x} - \begin{bmatrix} \mathbf{b} \\ 0 \end{bmatrix} \right\|^2 , \tag{2.3.22}$$

or in standard form:

$$\min \left\| \begin{bmatrix} \tilde{\mathbf{A}} \\ \lambda \mathbf{I} \end{bmatrix} \overline{\mathbf{x}} - \begin{bmatrix} \mathbf{b} \\ 0 \end{bmatrix} \right\|^2 , \tag{2.3.23}$$

where $\overline{\mathbf{x}} = \mathbf{Lx}$ and $\tilde{\mathbf{A}} = \mathbf{AL}^{-1}$.
The parameter λ determines the importance of the penalty term $\lambda^2 \|\mathbf{Lx}\|^2$ relative to the residual. The appropriate value of the regularization parameter is difficult to determine, even though many different methods have been developed [Kilmer and O'Leary, 2001]. In our case, we decided to choose the regularization parameter based on the L-curve criterion. The L-curve is a logarithmic plot of the norm against the residual, which often takes the shape of the letter L. It is assumed that the corner of the L-curve indicates

the optimal value of λ [Hansen, 1998]. The regularization matrix $\mathbf{L}$ can take many different forms. Often used matrices are for example finite difference approximations to the first or second derivative. In this research we employ the regularization matrix to include structural prior information, which will be described in Chapter 4.

2.3.3 The LSQR method

The dimensions of our problem are very large and it would take too much time and computational effort to solve it with an explicit method like the Singular Value Decomposition. Iterative methods can be used instead for inversion of large scale problems. Well-known iterative methods are for example the Conjugate Gradient method and the ART algorithm [Kak and Slaney, 2001], which is often used for tomographic imaging. In this research we use a method that is similar to SVD, but much more memory efficient: the LSQR method.

The LSQR method [Paige and Saunders, 1982a,b] is an iterative inversion method, that can be understood as an iterative Singular Value Decomposition. In each iteration, rows of the left and right matrices of basis vectors and elements of a bi-diagonal matrix are calculated. An approximation of the singular values, called Ritz values can be estimated for each iteration. After a large number of iterations, the Ritz values will converge towards the actual singular values of the matrix, but will not be identical. The LSQR algorithm is designed such that only matrix-vector multiplications are needed, resulting in a very memory efficient inversion method. The left, right and bi-diagonal matrices do not need to be stored completely, only two rows of the matrices are needed for each iteration, and preceding rows can be cleared. It generates a sequence of iteration vectors $\mathbf{x}^k$, with $k = 1, 2, 3$ the iteration number. In our case, we are trying to minimize an ill-conditioned linear system, for which the LSQR method is semi-convergent. This means that the vector $\mathbf{x}^k$ approaches the optimal solution after a limited number of iterations $k < n$ and if the iterations are not stopped, the method may converge to a worse solution corrupted by noise. The solution $\mathbf{x}^k$ can be understood as a regularized solution, with the iteration number k a regularization parameter. We summarize the LSQR method here, closely following the derivation in [Paige and Saunders, 1982a,b]. The two main steps in the LSQR algorithm are bi-diagonalization of the matrix $\mathbf{A}$ using a Lanczos process, and QR factorization of $\mathbf{A}$ using Givens rotations, explained below.

In the LSQR algorithm, a Lanczos process is used in a way that transforms the matrix $\mathbf{A}$ to a bi-diagonal matrix (values at the center diagonal and the diagonal below). For a starting vector $\mathbf{b}$ (the data vector) this bi-diagonalization procedure can be summarized as:

BIDIAG. I

1 $\beta_1 \mathbf{u}_1 = \mathbf{b}$
2 $\alpha_1 \mathbf{v}_1 = \mathbf{A}^T \mathbf{u}_1$
3 **for** k = 1 **to** number of steps
4 $\quad \beta_{k+1} \mathbf{u}_{k+1} = \mathbf{A}\mathbf{v}_k - \alpha_k \mathbf{u}_k$
5 $\quad \alpha_{k+1} \mathbf{v}_{k+1} = \mathbf{A}^T \mathbf{u}_{k+1} - \beta_{k+1} \mathbf{v}_k$

Using the following definitions:

$$\mathbf{U}_k = [\mathbf{u}_1, \mathbf{u}_2, ..., \mathbf{u}_k], \tag{2.3.24}$$

$$\mathbf{V}_k = [\mathbf{v}_1, \mathbf{v}_2, ..., \mathbf{v}_k], \tag{2.3.25}$$

and

$$\mathbf{B}_k = \begin{bmatrix} \alpha_1 & & & & \\ \beta_2 & \alpha_2 & & & \\ & \beta_3 & & & \\ & & \ddots & & \\ & & \ddots & \alpha_k & \\ & & & \beta_{k+1} & \end{bmatrix}, \tag{2.3.26}$$

the recurrence relations based on the bidiagonalization procedure can be written as:

RECURRENCE RELATIONS BIDIAG. I

1 $\mathbf{U}_{k+1} (\beta_1 \mathbf{e}_1) = \mathbf{b}$
2 $\mathbf{A}\mathbf{V}_k = \mathbf{U}_{k+1} \mathbf{B}_k$
3 $\mathbf{A}^T \mathbf{U}_{k+1} = \mathbf{V}_k \mathbf{B}_k^T + \alpha_{k+1} \mathbf{v}_{k+1} \mathbf{e}_{k+1}^T$

Where $\mathbf{e}_i$ is a vector with only zero entries, except for the i^{th} value in the vector, which is 1.
Using the bi-diagonalization procedure we can project the problem to a smaller subspace. If we suppose the solution at iteration k has the form $\mathbf{x}_k = \mathbf{V}_k \mathbf{y}_k$, and we define $\mathbf{r}_k = \mathbf{b} - \mathbf{A}\mathbf{x}_k$ to be the corresponding residual

at iteration k, then we can write $\mathbf{r}_k$ in terms of the quantities defined above as:

$$\mathbf{r}_k = \mathbf{U}_{k+1}\left(\beta_1 \mathbf{e}_1 - \mathbf{B}_k \mathbf{y}_k\right). \tag{2.3.27}$$

This leads to the projected problem:

$$\min \left\| \begin{bmatrix} \mathbf{B}_k \\ \lambda \mathbf{I} \end{bmatrix} \mathbf{y}_k - \begin{bmatrix} \beta_1 \mathbf{e}_1 \\ 0 \end{bmatrix} \right\|^2. \tag{2.3.28}$$

The projected problem can be solved using QR factorization. The QR factorization of a matrix $\mathbf{A}$ has the form:

$$\mathbf{A} = \mathbf{QR}, \tag{2.3.29}$$

where $\mathbf{R}$ is uppertriangular (values on main diagonal and above) with positive diagonal elements and $\mathbf{Q}$ is an orthogonal matrix ($\mathbf{Q}^T\mathbf{Q} = I$). The QR factorization can be obtained using Givens rotations. The Givens rotation matrix $\mathbf{G}$ is defined by [Salas et al., 2003]:

$$\mathbf{G}(i,j,\theta) = \begin{bmatrix} \cos\theta & -\sin\theta & \cdots & 0 & 0 \\ \sin\theta & \cos\theta & \cdots & 0 & 0 \\ 0 & 0 & 1 & 0 & 0 \\ \vdots & \vdots & & \ddots & \\ 0 & 0 & \cdots & 0 & 1 \end{bmatrix}, \tag{2.3.30}$$

with i and j indicating the columns and rows that contain the rotation. $\mathbf{G}(i,j,\theta)$ is an orthogonal matrix. Multiplication of a matrix $\mathbf{A}$ by the Givens rotation matrix $\mathbf{G}(i,j,\theta)$, makes the element a_{ji} zero if θ is chosen as:

$$\cos\theta = \frac{a_{ii}}{\sqrt{a_{ii}^2 + a_{ji}^2}} \quad \text{and} \quad \sin\theta = \frac{-a_{ji}}{\sqrt{a_{ii}^2 + a_{ji}^2}}. \tag{2.3.31}$$

We can make all elements below the diagonal zero using rotations, starting from the first non-zero element in the first column below the diagonal, proceeding from top to bottom, and then with the second column and further. This procedure results in an upper triangular matrix $\mathbf{R}$:

$$\underbrace{\mathbf{G}_{k,k+1}...\mathbf{G}_{2,3}\mathbf{G}_{1,2}}_{\mathbf{Q}_k}\mathbf{A} = \mathbf{R}. \tag{2.3.32}$$

In our case $\mathbf{Q}_k$ contains two sequential rotations, the first rotation eliminates λ, and the second rotation eliminates β_i, following:

$$\begin{bmatrix} \alpha_1 & & \beta_1 \\ \beta_2 & \alpha_2 & \\ & \beta_3 & \\ \lambda & & \\ & \lambda & \end{bmatrix} \rightarrow \begin{bmatrix} \tilde{\rho}_1 & & \tilde{\phi}_1 \\ \beta_2 & \alpha_2 & \\ & \beta_3 & \\ & & \psi_1 \\ & \lambda & \end{bmatrix} \rightarrow \begin{bmatrix} \rho_1 & \theta_2 & \phi_1 \\ & \bar{\rho}_2 & \bar{\phi}_2 \\ & \beta_3 & \\ & & \psi_1 \\ & \lambda & \end{bmatrix}$$

$$\begin{bmatrix} \rho_1 & \theta_2 & \phi_1 \\ & \tilde{\rho}_2 & \tilde{\phi}_2 \\ & \beta_3 & \\ & & \psi_1 \\ & & \psi_2 \end{bmatrix} \rightarrow \begin{bmatrix} \rho_1 & \theta_2 & \phi_1 \\ & \rho_2 & \phi_2 \\ & & \bar{\phi}_3 \\ & & \psi_1 \\ & & \psi_2 \end{bmatrix}.$$

After k iterations, the QR factorization takes the form:

$$Q_k \begin{bmatrix} \mathbf{B}_k & \beta_1 \mathbf{e}_1 \\ \lambda \mathbf{I} & 0 \end{bmatrix} = \begin{bmatrix} \mathbf{R}_k & \mathbf{f}_k \\ 0 & \bar{\phi}_{k+1} \\ 0 & q_k \end{bmatrix} = \begin{bmatrix} \rho_1 & \theta_2 & & & & \phi_1 \\ & \rho_2 & \theta_3 & & & \phi_2 \\ & & \ddots & \ddots & & \vdots \\ & & & \rho_{k-1} & \theta_k & \phi_{k-1} \\ & & & & \rho_k & \phi_k \\ & & & & & \bar{\phi}_{k+1} \\ & & & & & q_k \end{bmatrix}.$$

Based on the QR factorization, the solution can be found from:

$$\mathbf{R}_k \mathbf{y}_k = \mathbf{f}_k, \tag{2.3.33}$$

$$\mathbf{x}_k = \mathbf{V}_k \mathbf{R}_k^{-1} \mathbf{f}_k = \mathbf{D}_k \mathbf{f}_k, \tag{2.3.34}$$

where the columns of $\mathbf{D}_k = [\mathbf{d}_1, \mathbf{d}_2, ..., \mathbf{d}_k]$ are found from $\mathbf{R}_k^T \mathbf{D}_k^T = \mathbf{V}_k^T$ by forward substitution. With $\mathbf{d}_0 = \mathbf{x}_0 = 0$, this gives:

$$\mathbf{d}_k = \frac{1}{\rho_k} \left(\mathbf{v}_k - \theta_k \mathbf{d}_{k-1} \right), \tag{2.3.35}$$

$$\mathbf{x}_k = \mathbf{x}_{k-1} + \phi_k \mathbf{d}_k. \tag{2.3.36}$$

In each iteration k, we only have to construct the two rotations that operate on rows k and $n + k$, and on rows k and $k + 1$. These can be discarded

afterwards, leading to a very memory-efficient calculation. The necessary rotations in iteration k can be summarized in two simple recurrence relations. The first relation describes the step that rotates λ out:

$$\begin{bmatrix} \hat{c} & \hat{s} \\ \hat{s} & -\hat{c} \end{bmatrix} \begin{bmatrix} \bar{\rho}_k & 0 & \bar{\phi}_k \\ \lambda & 0 & 0 \end{bmatrix} = \begin{bmatrix} \tilde{\rho}_k & 0 & \tilde{\phi}_k \\ 0 & 0 & \psi_k \end{bmatrix}, \tag{2.3.37}$$

and the second relation describes the step that rotates β_{k+1} out:

$$\begin{bmatrix} c & s \\ s & -c \end{bmatrix} \begin{bmatrix} \tilde{\rho}_k & 0 & \tilde{\phi}_k \\ \beta_{k+1} & \alpha_{k+1} & 0 \end{bmatrix} = \begin{bmatrix} \rho_k & \theta_{k+1} & \phi_k \\ 0 & \bar{\rho}_{k+1} & \bar{\phi}_{k+1} \end{bmatrix}. \tag{2.3.38}$$

We formulate the implementation that was used in this research on the following page, which was originally programmed in Matlab by Damon Hyde and further adjusted.

2.4 Summary

In this chapter we described the forward model and inversion techniques used for the estimation of the 3d fluorescence distribution in Fluorescence Molecular Tomography. The forward model is based on the diffusion equation. The inversion method that we use is the LSQR method. We stabilize the problem with Tikhonov type regularization. The estimate of the fluorescence distribution can be improved by including additional information that is known on beforehand, so called prior information, in the forward model and inversion. In the following chapters we will describe the prior-based methods that we developed specifically for the hybrid FMT-XCT system. In this research we use prior information in the forward model in the form of heterogeneous optical properties of the medium, which will be described in Chapter 5. In the inversion we employ the regularization matrix to include structural prior information, which will be described in Chapter 4.

ALGORITHM LSQR

INITIALIZE

$\beta_1 = \|\mathbf{b}\|,\ \beta_1\mathbf{u}_1 = \mathbf{b}$

$\alpha_1 = \left\|\mathbf{A}^T\mathbf{u}_1\right\|,\ \alpha_1\mathbf{v}_1 = \mathbf{A}^T\mathbf{u}_1$

$\mathbf{w}_1 = \mathbf{v}_1,\ \overline{\phi}_1 = \beta_1,\ \overline{\rho}_1 = \alpha_1$

for k = 1 **to** number of iterations

BI-DIAGONALIZATION STEP

$\beta_{k+1} = \|\mathbf{A}\mathbf{v}_k - \alpha_k\mathbf{u}_k\|,\ \mathbf{u}_{k+1} = (\mathbf{A}\mathbf{v}_k - \alpha\mathbf{u}_k)/\beta$

$\alpha_{k+1} = \left\|\mathbf{A}^T\mathbf{u}_{k+1} - \beta_{k+1}\mathbf{v}_k\right\|,\ \mathbf{v}_{k+1} = (\mathbf{A}^T\mathbf{u}_{k+1} - \beta_{k+1}\mathbf{v}_k)/\alpha_{k+1}$

for i = 1 **to** number of λ

ROTATE λ OUT

$\widetilde{\rho}_k = \sqrt{\overline{\rho}_k^2 + \lambda^2}$

$\widehat{c}_k = \overline{\rho}_k/\widetilde{\rho}_k,\ \widehat{s}_k = \lambda/\widetilde{\rho}_k$

$\widetilde{\phi}_k = \widehat{c}_k\overline{\phi}_k,\ \psi_k = \widehat{s}_k\overline{\phi}_k$

ROTATE β OUT

$\rho_k = \sqrt{\widetilde{\rho}_k^2 + \beta_{k+1}^2}$

$c_k = \widetilde{\rho}_k/\rho_k,\ s_k = \beta_{k+1}/\rho_k$

$\theta_{k+1} = s_k\alpha_{k+1},\ \overline{\rho}_{k+1} = -c_k\alpha_{k+1}$

$\phi_k = c_k\widetilde{\phi}_k,\ \overline{\phi}_{k+1} = s_k\widetilde{\phi}_k$

UPDATE x AND w

$\mathbf{x}_k = \mathbf{x}_{k-1} + (\phi_k/\rho_k)\mathbf{w}_k$

$\mathbf{w}_{k+1} = \mathbf{v}_{k+1} - (\theta_{k+1}/\rho_k)\mathbf{w}_k$

3

FMT-XCT data acquisition

3.1 Introduction

Acquiring an optimal experimental data set is crucial for obtaining an accurate reconstruction of the fluorescence distribution inside a mouse. In this chapter we describe how we acquired data with the hybrid FMT-XCT system that was described in Chapter 1, and which parameters we used. The hybrid FMT-XCT system delivers planar white light images, trans-illumination images acquired at the emission and excitation wavelength, and a 3d X-ray CT volume. Visual inspection of the acquisition data can already provide a large amount of information on the experiment. We will give examples of the data and describe the features that can be recognized in the images.

3.2 Acquisition setup

The acquisition setup that was used for all experiments in this thesis is schematically represented in Figure 3.1. The acquisition was managed by two connected computers, one for the FMT acquisition, and one for XCT acquisition. Acquisition parameters were controlled by configuration software. Mice and phantoms were placed in the system using the animal bed slider. The cover of the animal bed slider could be opened on one side, after which the mouse or phantom could be placed on the mouse bed (Figure 3.2a). The bed consisted of two carbon rods of 3 mm diameter, 2.5 cm apart, with strings in a zig-zag pattern in between for holding the mouse or phantom (Figure 3.2b). The animal bed could automatically slide into the system controlled by the acquisition software. During in-vivo experiments,

isoflurane anesthesia was provided through tubes leading to an anesthesia cap that was placed over the nose of the mouse.

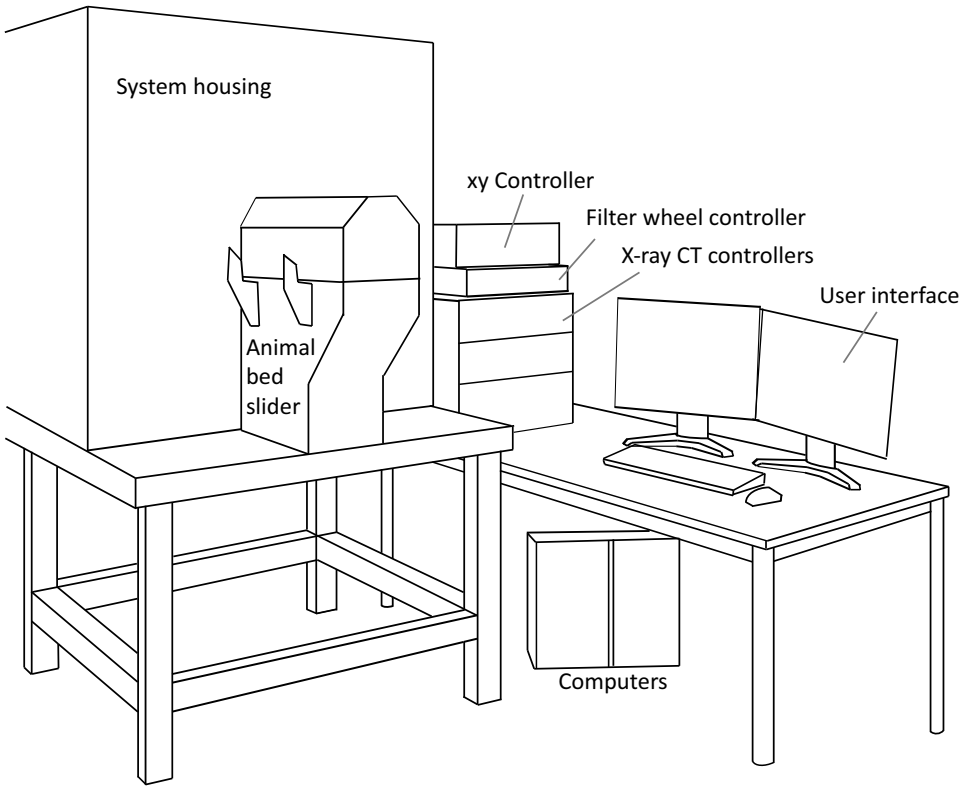

Figure 3.1: Acquisition setup. The system housing contained the rotating gantry with FMT-XCT instrumentation. External controllers were connected to two computers and the user interface. The mouse bed could be accessed by opening the cover of the animal bed slider.

The mice needed to be placed on the mouse bed in a position that was comfortable for the mouse in order to enable longitudinal experiments and optimal for our reconstruction method in order to obtain an accurate estimation of the fluorescence distribution. Skin flaps, wrinkles and air could not be accurately modelled with the diffusion approximation that is used for the reconstruction (see Chapter 2). We minimized the presence of air gaps and skin flaps between the arms and the body of the mouse by placing the arms as close to the animal as possible. Figure 3.3b displays the preferred mouse positioning for thorax imaging, this is a natural position for the mouse and at the same time the shape of the mouse is nearly cylindrical.

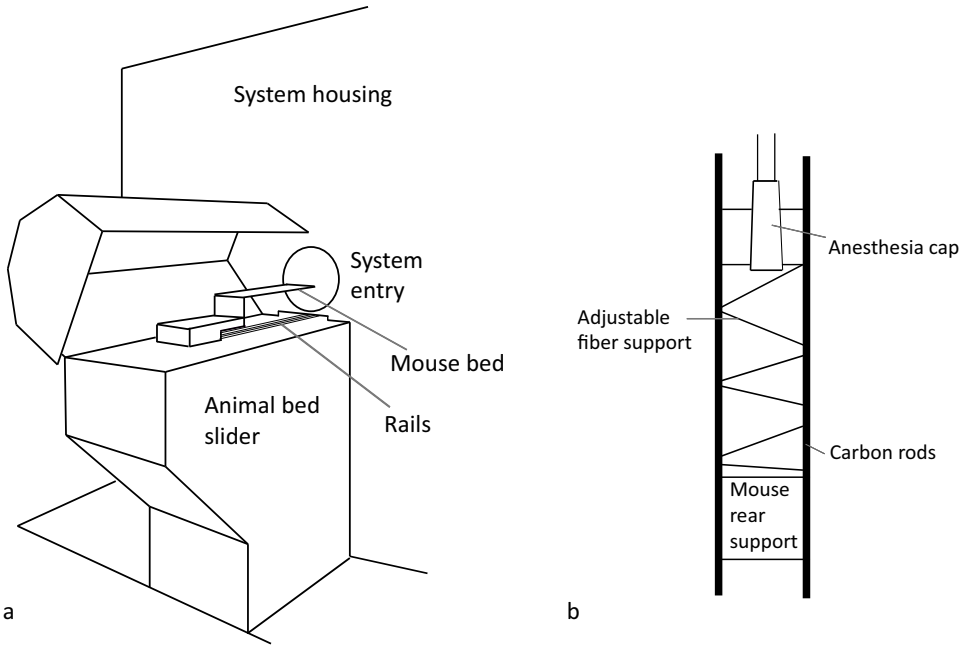

Figure 3.2: Animal bed slider. a) Slider. The mouse bed was mounted on rails that allowed the bed to automatically slide into the system through the system entry. b) Mouse bed. The mouse bed consisted of adjustable fibers on which the mouse could be placed in a comfortable position. The nose of the mouse was placed in the anesthesia cap. The mouse rear support increased mouse comfort and protected the system.

The strings of the bed were flexible and movable. We placed the strings in a configuration that left the main area of interest wire-free. Remaining areas with skin flaps or wrinkels after optimal positioning were excluded from the data that was used as input for the reconstruction.

A number of parameters could be changed before each acquisition. The values we used for most studies are summarized in Table 3.1. We scanned sources in a regular grid over the mouse surface, usually 3 positions in a row across the mouse, and several rows along the mouse. The number of rows depended on the size of the region of interest, and varied between 3 for a subcutaneous tumor to 8 for a thorax or abdomen scan. We usually scanned the source pattern for 18 projection angles of the gantry (every 20°). In [Lasser and Ntziachristos, 2007] it was shown that this amount of projection angles is optimal. The intrinsic illumination time was usually set to 0.1 s or 0.2 s. Depending on the signal strength, we set the base illumination time

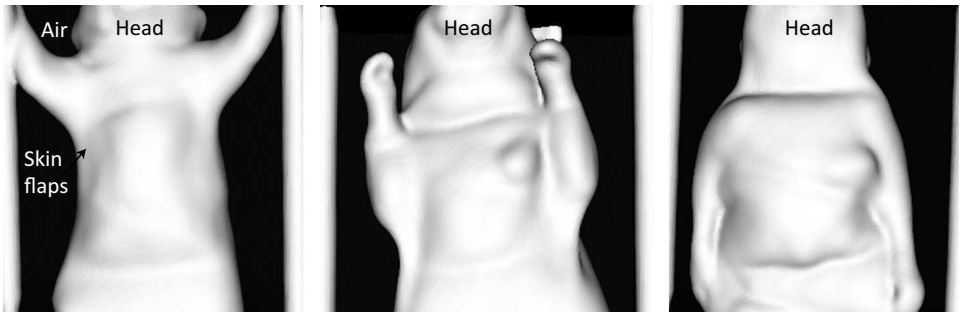

Figure 3.3: Optimal Mouse Placement. a) A mouse positioned with arms up and wide results in skin flaps that can not be accurately modelled with the diffusion equation. b) Optimal position, the mouse is comfortable and has a shape that fits the model. c) Position that fits the model as well, but can be less comfortable for the mouse.

for fluorescence acquisition between 0.2 s and 1 s. The total fluorescence acquisition time was automatically increased with the chosen increment to a maximum exposure time that we usually set to 6 s, and in some cases to 2 s.

Table 3.1: Acquisition parameters used for FMT-XCT experiments.

Parameter	Setting
Sources - spacing	Grid with 2 mm - 3 mm spacing, covering area of interest
Sources - n	9 - 24 sources (3x3 - 3x8)
Gantry angles	18 angles, every 20 degrees
Intrinsic illumination	0.1 s - 0.2 s
Fluorescence illumination	0.2 s - 1 s increments, until max. 2 s - 6 s

3.3 Examples of X-ray CT data

The acquired X-ray CT data was reconstructed into a 3d volume using software delivered with the GE micro-CT system (Microview, GE Medical Systems). The reconstruction of a 3d volume with a resolution of 95 μm took about 40 minutes per data set. Examples of slices through the X-ray CT volume are displayed in Figure 3.4. Figure 3.4a shows a healthy mouse. The lungs regularly have a dark grey appearance, the bones appear white

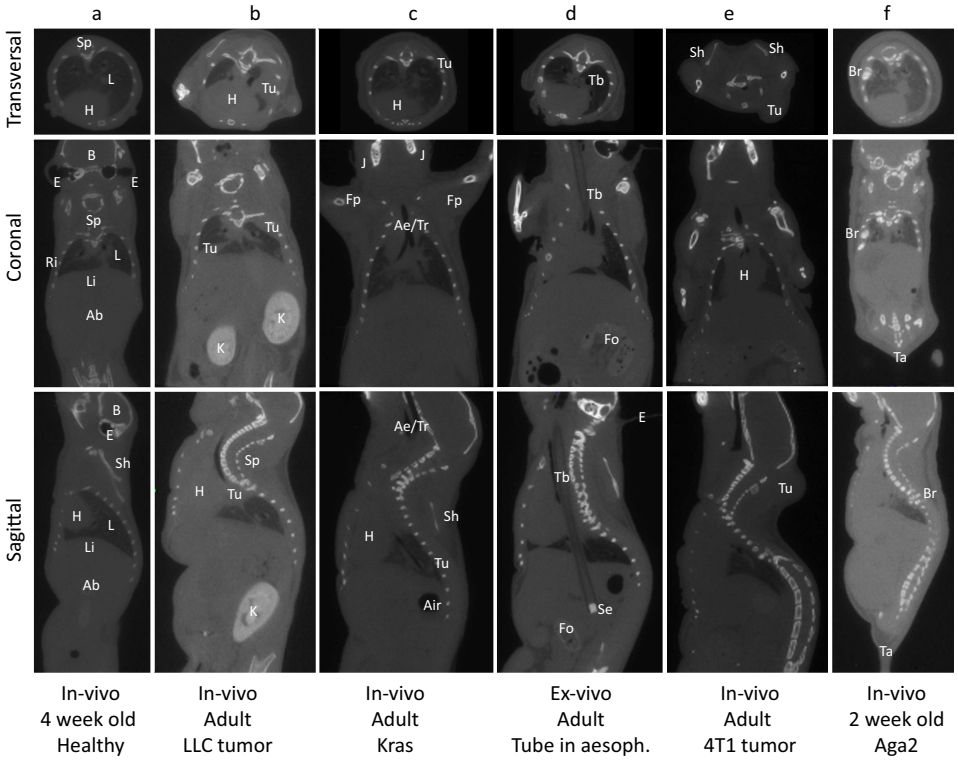

Figure 3.4: Examples of slices through the 3d X-ray CT volume. Sp=Spine, L=Lung, H=Heart, B=Brain, E=Ear, Ri=Ribcage, Li=Liver, Ab=Abdomen, Sh=Shoulderblades, Tu=Tumor, K=Kidney, J=Jaw, Fp=Front paw, Ae/Tr=Aesophagus and Trachea, Air=Air, Tb=Tube, Se=Tube sealant, Fo=Food, Br=Broken bones, Ta=Tail.

and remaining tissue including the heart appears light grey. Mouse b (Figure 3.4b) was injected with a CT contrast agent 15 minutes before imaging. The contrast agent washed out towards the kidneys, which appear much brighter here than in mouse a. This mouse has a xenograft lung tumor (LLC tumor cells were injected into the lungs, see Section 8.3). The relatively large tumors, indicated by Tu, have an appearance similar to muscle tissue. Mouse c is genetically modified to develop spontaneous lung tumors. These tumors are much smaller compared to mouse b, and can be recognized as small spots close to the borders of the lung area. Regions with air in the digestion system are observed in the abdomen. Mouse d has a tube in the aesophagus, filled with a mixture that matches the optical properties of tissue. Also in these X-ray CT images the mixture appears similar to tissue. The sealant at both ends of the tube appears white. Mouse e has a subcutaneous breast

and neck tumor, that can be recognized as elevated areas (indicated with Tu). Finally, mouse f is a 2 week old mouse with a genetic modification that causes bones to break easily. Areas of bone remodelling can be distinguished as areas of increased whiteness, indicated by Br (see Section 8.5).

We compared the effect of X-ray CT contrast agents on the visibility of the two heart chambers for the investigation of myocardial infarction (Section 8.6). We evaluated two different X-ray CT contrast agents (Figure 3.5). The first contrast agent we evaluated was Accupaque, an iodine based contrast agent, also known as Omnipaque (GE Healthcare, Buchler, Braunschweig, Germany). This contrast agent had the advantage that it was transparent, but washed out towards the kidneys in several minutes (Figure 3.5a-c). Because a typical X-ray CT acquisition took >15 minutes, we could only see the effect of the contrast agent in the heart area when the mouse was euthanized directly after injection of contrast agent (Figure 3.5d-f). The second contrast agent that we evaluated was ExiTron nano 12000 (Viscover), a metal-based contrast agent specifically designed for pre-clinical X-ray CT. This contrast agent is not transparent, but has a longer circulation time and resulted in a very good contrast in the heart (Figure 3.5g-i).

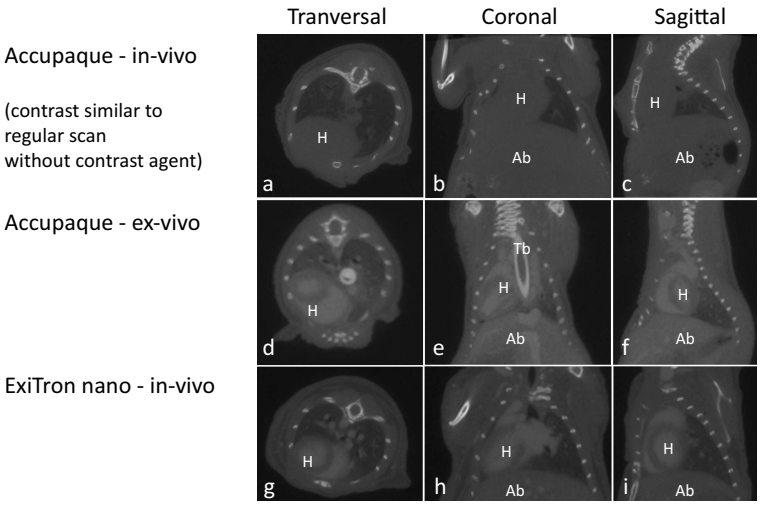

Figure 3.5: Comparison of the effect of X-ray CT contrast agents. a-c) Accupaque, in-vivo. d-f) Accupaque, ex-vivo. g-i) ExiTron nano 12000, in-vivo. (H=Heart, Ab=Abdomen, Tb=Tube.)

3.4 Examples of FMT data

White light images acquired at all of the 18 projection angles that we used for FMT acquisition are displayed in Figure 3.6. The rods and strings of the mouse bed are blocking part of the mouse from the field of view in projections 7-16. Acquisition data from the blocked areas of the mouse was excluded before reconstruction.

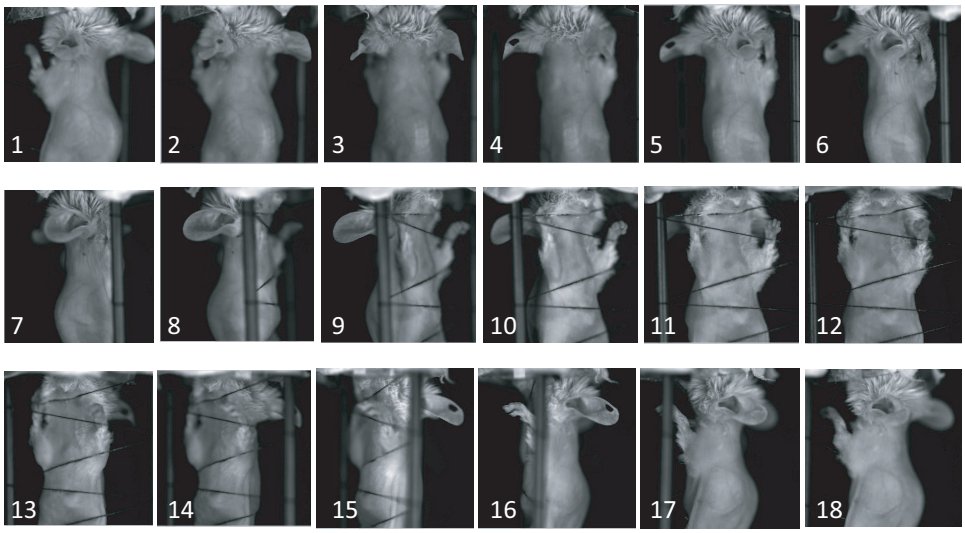

Figure 3.6: White light images for all 18 projection angles at which FMT data was acquired.

Figure 3.7 shows examples of normalized FMT trans-illumination acquisition images (emission/excitation) for six different experiments. It is often possible to roughly estimate where the brightest source of fluorescence is located based on the normalized trans-illumination images. Each image corresponds to one source position, scaling was applied for each image individually. We selected for each case an angle and source position that showed a clear signal from the region of interest. Figure 3.7a shows a normalized image of the thorax of a mouse with a tube with fluorescence inserted in the aesophagus (view from the front of the mouse, see Chapter 7). The tube can be easily identified. The signal is so strong that the mouse is almost not visible anymore although the mouse is visible in the other images (of mice which are all injected with a fluorescent probe). Figure 3.7b shows an image of a mouse with a heart infarct, injected with a probe targeting apoptosis (see Section 8.6). A signal from the heart area is distinguishable, but also a strong signal

from the liver area (view from the front). Figure 3.7c shows an image of the head of a mouse with a brain tumor that is expressing fluorescent proteins (see Section 8.4). The tumor on one side of the brain can be identified (view from the back). Figure 3.7d shows an image of the neck area of a mouse with a subcutaneous tumor and injected with a targeted fluorescent probe (view from the back, see Chapter 7). Figure 3.7e shows an image of a mouse injected with a probe targetting bone formation (view from the front, see Section 8.5). And finally Figure 3.7f shows a normalized image of a cylindrical phantom with two tubes inside, filled with two different concentrations of fluorescent dye (see Section 4.4).

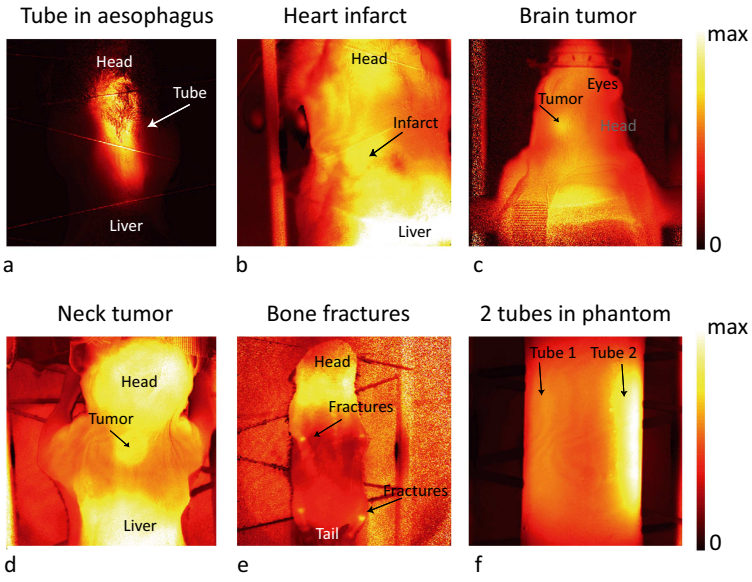

Figure 3.7: Examples of normalized FMT acquisition images. The area of interest is indicated with an arrow.

3.5 Summary and Conclusions

In this chapter we outlined the steps we followed during experiments. One of the important steps before starting the FMT-XCT acquisition was optimal mouse placement. A good mouse placement improves the agreement between the actual light propagation and the modelled light propagation through the mouse, which is part of the reconstruction.
We indicated several features that are distinguishable in the X-ray CT data

and that can be used to assess the condition of the mouse. We showed that the information content of the X-ray CT data can be improved using an appropriate contrast agent.
We described the parameters used for the acquisition of FMT images and compared trans-illumination images obtained with the FMT modality for several cases, which showed that each case has a considerably different appearance and a rough estimation of the location of the brightest source of fluorescence could be made. However, in order to find the exact fluorescence distribution inside a mouse, we need to perform a 3d reconstruction. How we perform an optimal 3d fluorescence reconstruction will be explained in the following chapters.

4

Inversion of hybrid FMT-XCT data

4.1 Introduction

The hybrid FMT-XCT inversion method that we developed employs the anatomical information obtained from the X-ray CT data for finding an improved estimate of the fluorescence distribution. We included the anatomical information obtained from the X-ray CT data in the inversion in the form of a structural regularization matrix. The basis for the formation of the matrix was an anatomical segmentation of the X-ray CT data. We investigated how to optimally formulate the structural regularization matrix based on a comparison of reconstructions of simulated data and experimental data acquired with the hybrid FMT-XCT system using different implementations of the regularization matrix (Section 4.2). The optimal matrix (Section 4.3) contained a set of parameters, for which we developed a data driven estimation method in order not to bias the solution (Section 4.4).

4.2 Evaluation of structural penalty matrices

In the methods we have investigated we included a priori information in the inverse problem using the regularization matrix $\mathbf{L}$:

$$\|\mathbf{W}\mathbf{x} - \mathbf{y}\|^2 + \lambda^2 \|\mathbf{L}\mathbf{x}\|^2 . \tag{4.2.1}$$

The use of structural penalty matrices has been introduced before for FMT as well as for estimation of the scattering and absorption coefficients in Diffuse Optical Tomography (DOT). Davis et al. [2007] described a method

that incorporated structural prior information of the internal tissue structure through a Laplacian-type regularization matrix, applied to both DOT and FMT reconstruction. The FMT reconstruction method was tested on phantom and simulation studies and resulted in significant improvements of the reconstruction. Lin et al. [2009] have shown quantitative results of recovery of fluorescence concentration using the same Laplacian-type structural prior combined with functional prior information applied to cylindrical phantom experiments. A different method was developed by Hyde et al. [2009a], who investigated the incorporation of structural information using Tikhonov-type priors to estimate the fluorescence concentration. The application of this method to the reconstruction of amyloid-β plaques in the brains of an Alzheimer's mouse model showed considerable improvements in the recovery of the true signal, compared to the stand-alone method using no structural priors [Hyde et al., 2010]. Finally, Intes et al. [2004] developed methods to include structural prior information in the DOT reconstruction in terms of a Bayesian framework.

In this chapter we describe the evaluation of different structural penalty matrices, some that were developed previously and several new combinations of the previously developed methods.

4.2.1 Anatomical segmentation of the X-ray CT volume.

The basis for including information from X-ray CT in the different steps of the hybrid method was a segmentation of the X-ray CT volume in anatomical regions. Several anatomical regions in the thorax could be segmented semi-automatically, while others were segmented manually.

Semi-automatic segmentation tools for the thorax region were developed by Marcus Freyer [Freyer et al., 2010], capable of segmenting bones, lungs and heart. Segmentation of the bones was fully automatic and consisted of thresholding the X-ray CT volume. The lungs were segmented in a semi-automatic way. Two transversal slices of the X-ray CT volume of the mouse were selected manually, corresponding to the beginning and end of the lung region. Seed points were placed by the algorithm in the indicated lung-area using the delimitations of the already segmented ribcage. The lung segment was formed by expanding the seed points during a pre-set number of iterations. Segmentation of the heart consisted of placing a pre-defined heart model in the cavity between segmented lungs and ribcage. The heart model

was moved from a starting position in all directions until it was not overlapping with the lung or bone segment. We modified the semi-automatic segmentation in several ways in order to optimize it for calculation of the forward model and inversion. We preferred to obtain well defined connecting regions, while the semi-automatic segmentation would result in several segments with small residual areas of undefined tissue in between. The heart model was often found to be too small, resulting in undefined spaces between heart, lungs and bones. Cavities would also exist inside the lung segments, at the place of blood vessels, large bronchi, aesophagus and tumors. In order to obtain continuous connecting segments, we applied morphological filling and dilation operations to the lung and heart segment. Segmentation of other segments than bone, lung and heart was not possible with the framework. We wrote a semi-manual segmentation routine for segmentation of the brain, subcutaneous tumors, and non-anatomical elements such as tubes.

The segmentation finally consisted of a 3d volume of the same size as the X-ray CT volume, in which all segments were indicated by different integers. The segmentation was used in the calculation of the forward model and inversion.

4.2.2 Evaluated methods

We evaluated six methods of constructing the regularization matrix $\mathbf{L}$: one method which does not depend on structural priors (method 1), and five methods that could be termed as soft priors (methods 2-6), summarized in Table 4.1. The matrices define different relationships between the voxels in the same or in different segments. To which segment the voxels belong is determined by mapping the segmentation of the XCT volume to the voxels. For the thorax the segmented regions were bone, heart, lungs and other tissue. The XCT image generally has a higher resolution (≈ 95 μm) than the FMT reconstruction (≈ 1 mm), consequently a voxel possibly belongs to multiple anatomical segments. The resolution of the XCT data is taken into account, by assigning voxels to potentially several neighboring segments through a segmentation matrix $C = c_{i,m}$ of size $N_{segments} \times N_{voxels}$, where $c_{i,m}$ is the volume percentage of voxel i that is contained in segment m [Hyde et al., 2009a]. As described above, the algorithm we used for inversion is the LSQR algorithm. This algorithm is particularly efficient in solving the problem for a large number of regularization parameters at a time in case the problem is formulated in standard form, i.e. with $\mathbf{L} = \mathbf{I}$. We

therefore transformed the problem of Equation 4.2.1 into standard form by substituting $\mathbf{x} = \mathbf{L}^{-1}\bar{\mathbf{x}}$, which is possible in case $\mathbf{L}$ is a square positive-definite matrix:

$$\left\|\mathbf{W}\mathbf{L}^{-1}\bar{\mathbf{x}} - \mathbf{y}\right\|^2 + \lambda^2 \left\|\bar{\mathbf{x}}\right\|^2. \tag{4.2.2}$$

The regularization parameter determines the significance of the penalty term in the total problem. For large values of λ, the minimum will mostly depend on the norm of the penalty and thus the solution will take the structure enforced by the regularization matrix; for small values of λ the regularization term has a limited effect on the position of the local minimum. The optimal regularization parameter λ is not known on before hand. Therefore we need to estimate the solution for a large number of regularization parameters. After minimizing Equation 4.2.2 for many different values of the regularization parameter, the optimal solution is selected based on a predetermined criterion such as the L-curve.

Table 4.1: Overview of evaluated regularization (or penalty) matrices.

Method	Effect on reconstruction
1. Standard Tikhonov	Smoothing towards zero
2. Weighted segments	More smoothing towards zero in regions with large weights, less in regions with small weights
3. Weighted segments with mean	More smoothing towards a predetermined mean in regions with large weights, less in regions with small weights
4. Laplace	Smoothing towards a mean value per region
5. Laplace + weighted segments	More smoothing towards a mean value per region in regions with large weights, less in regions with small weights
6. Local Laplace + weighted segm.	More smoothing towards a mean value among neighbors in regions with large weights, less in regions with small weights

1. Standard Tikhonov regularization

In standard Tikhonov regularization, the regularization matrix $\mathbf{L}$ is equal to the Identity matrix $\mathbf{I}$. This method does not depend on structural prior information.

2. Weighted segments regularization

In weighted segments regularization [Hyde et al., 2009a], the regularization matrix is a diagonal matrix. Each segment m is assigned a certain weight ω_m, enforcing stronger or weaker regularization per segment. Voxel weights α_i proportional to segment occupation are calculated by multiplying the weights by the segmentation matrix. The resulting vector of size $1 \times N_{voxels}$ is placed on the diagonal of the regularization matrix,

$$\mathbf{L} = \mathrm{diag}(\mathbf{C}\boldsymbol{\omega}). \tag{4.2.3}$$

For large values of λ the solution is forced towards zero, stronger for segments with large weights ω_m.

3. Weighted segments regularization with mean

The estimated concentration can additionally be forced towards a predetermined mean $\boldsymbol{\mu}$, for which Equation 4.2.1 changes to:

$$Q = \|\mathbf{W}\mathbf{x} - \mathbf{y}\|^2 + \lambda^2 \|\mathbf{L}\,(\mathbf{x} - \mathbf{C}\boldsymbol{\mu})\|^2 . \tag{4.2.4}$$

4. Laplace regularization

Laplace regularization [Yalavarthy et al., 2007a; Davis et al., 2007; Brooksby et al., 2005] is a method derived from the Laplace equation. This method smoothes the solution within individual segments, while allowing discontinuities across segment borders. The corresponding regularization matrix is given by

$$\mathbf{L}_{ij} = \begin{cases} -\frac{1}{N_m} & \text{i and j in the same segment,} \\ 1 & \text{i=j,} \\ 0 & \text{otherwise,} \end{cases} \tag{4.2.5}$$

with N_m the total number of voxels in segment m. In this case voxels can belong to one segment only. The multiplication $\mathbf{L}\mathbf{x}$ implicitly calculates an approximation of the difference between each voxel and the average over the other voxels in the same segment. For large values of λ, the solution within one segment is forced to an average value.

5. Laplace regularization with weighted segments

Combining Laplace regularization and weighted segments regularization leads to a smoothed form of Laplace regularization, with the segmentation matrix and weights added to 4.2.5:

$$L_{ij} = \begin{cases} -\alpha_i \sum_{n=1}^{M} \frac{c_{im} c_{jm}}{N_m} & \text{i and j in the same segment,} \\ \alpha_i \sum_{n=1}^{M} c_{im} & \text{i=j,} \\ 0 & \text{otherwise.} \end{cases} \tag{4.2.6}$$

The individual segments are now connected through the voxels at segment borders. For large values of the regularization parameter, the solution will again be forced to an average value.

6. Local Laplace regularization with weighted segments

A local form of Laplace regularization is created by connecting each voxel only to its neighbouring voxels proportional to segment occupation, instead of to the complete segment it is part of. Each regular voxel is connected to 26 neighbouring voxels:

$$L_{ij} = \begin{cases} -\alpha_i \sum_{n=1}^{M} \frac{c_{im} c_{jm}}{N_n} & \text{i and j neighbours,} \\ 1 & \text{i=j,} \\ 0 & \text{otherwise,} \end{cases} \tag{4.2.7}$$

with N_n the number of neighbours.

4.2.3 Evaluation based on simulations

We first evaluated the different structural penalty methods based on simulations. We examined two different scenarios of fluorescence bio-distribution in the lung. The first assumed a homogeneously distributed signal throughout the lung, which simulated spatially extended signals typical of inflammation responses in asthma or COPD (Chronic Obstructive Pulmonary Disease), referring to lung disease caused by inhalation of toxic particles, most commonly by smoking. The second assumed a localized fluorescence signal representative of diseases such as a solid tumor.

For the simulations we used the X-ray CT images from the BALB/c mouse that was also the subject of the ex-vivo experiment described below, as shown in Figures 4.1a,b. The semi-automatic segmentation framework described in Section 4.2.1 was used to segment the bones. Due to reduced contrast between lung and heart tissue, the segmentation of these two tissue types and remaining tissue could not be done using the segmentation

framework, but was obtained manually using known anatomical markers delineating the heart wall. The segmentation is shown in Figure 4.1c. Segment weights were manually set to 1 for the lung segment and 4 for the remaining segments. We assumed heterogeneous optical properties for different anatomical regions based on [Niedre et al., 2006], see Chapter 5.

Simulations were done using the Finite-Element-framework described in Section 2.2. The first step in the simulation was the creation of a forward model. A plane of Gaussian sources was created with a Full Width Half Maximum (FWHM) of 0.05 cm. The distribution of excitation light in the volume as a result of the sources was calculated by solving the forward model on the nodes of the mesh for the given source positions. This distribution was multiplied with the fluorescence distribution inside the volume. The sources for the emission light were calculated from the result. The distribution of emission light was calculated by solving the forward model on the nodes of the mesh for the fluorescent sources. Finally the excitation data set was obtained by evaluating the distribution of excitation light at a plane of Gaussian detectors, and the emission data set by evaluating the distribution of emission light at the same plane of Gaussian detectors. The number of nodes in the Finite Element Mesh used for the simulations was 64065, mapped into 3005 voxels of size $1 \times 1 \times 1$ mm^3. Measurements were assumed from 21432 source-detector pairs. The source-detector configuration was taken from the actual measurement. Additive Gaussian distributed noise was added to the simulated readings with a signal to noise ratio of 10.

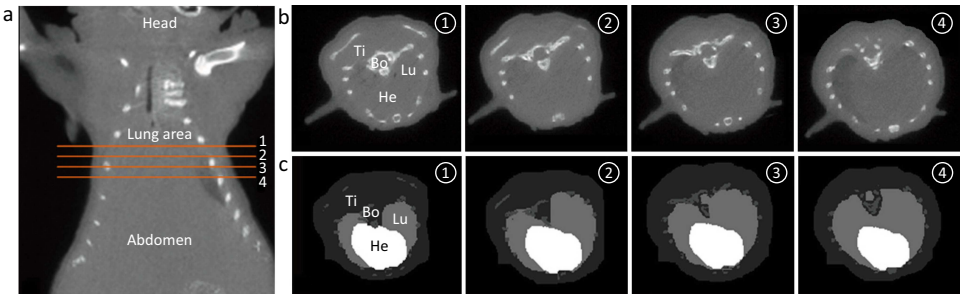

Figure 4.1: X-ray CT data and segmentation. a) Coronal slice. The lines indicate the positions of investigated slices. b) Transversal X-ray CT slices corresponding to the lines indicated in Figure a. c) Segmentation of the volume in bones (Bo), lungs (Lu), heart (He), and other tissue (Ti) for the same slices.

As error measure E between simulation and reconstruction we used the following definition:

$$E = \frac{\|\mathbf{x}_s - \mathbf{x}\|^2}{N_{voxels}}, \tag{4.2.8}$$

where $\mathbf{x}_s$ is the simulated fluorochrome distribution.

Two inclusions were simulated for the local simulation, one inclusion with a diameter of 3 mm and a smaller inclusion with a diameter of 2 mm (Figure 4.2a). The simulated fluorescence bio-distribution was mapped for visualization to the voxels for a slice of the reconstructed volume corresponding to position 4 (Figure 4.1a) and overlaid onto the corresponding slice of the X-ray CT volume. The results displayed in Figures 4.2b-f show a general improvement in the agreement of simulated and reconstructed fluorescence concentration when hybrid methods were used compared to the standard Tikhonov method (Figure 4.2b). Functional prior information in the form of optical properties was included in the Tikhonov reconstruction, as well as in all other reconstructions. The optical properties used for simulation were exactly equal to the optical properties used for reconstruction of the simulated data. Structural information based on the segmentation has been included in all methods except for the Tikhonov method. Reconstructions using respectively the weighted segments method, weighted segments+Laplace method and local Laplace method (Figures 4.2d-f) include the segmentation matrix that more accurately matches the reconstruction voxels to the anatomical regions.

Investigating the profiles corresponding to the localized signal, Figure 4.2g-l, we observe that each of the reconstruction methods resolved two inclusions, centred at the correct position. The size of the reconstructed inclusions is considerably overestimated by the standard Tikhonov method and the Laplace method. An improved estimation of size is seen in the profiles corresponding to the weighted segments method and the Laplace+weighted segments method, although also slightly overestimated. Reconstruction with the local Laplace method shows an improved size estimation compared to the standard Tikhonov method, comparable to the weighted segments and Laplace+weighted segments method. Of concern is the negative signal recovered by the local Laplace method in between the two inclusions, which has no physical explanation. Regarding quantification, it is observed that improved quantification goes in parallel with improved size estimation. Furthermore,

the error in quantification is larger for the small inclusion compared to the larger inclusion. Although both inclusions have the same maximum fluorescence concentration, each of the methods displays a lower concentration for the small inclusion. This can be partly attributed to the relative position of the profile with regard to the centre of the inclusion.

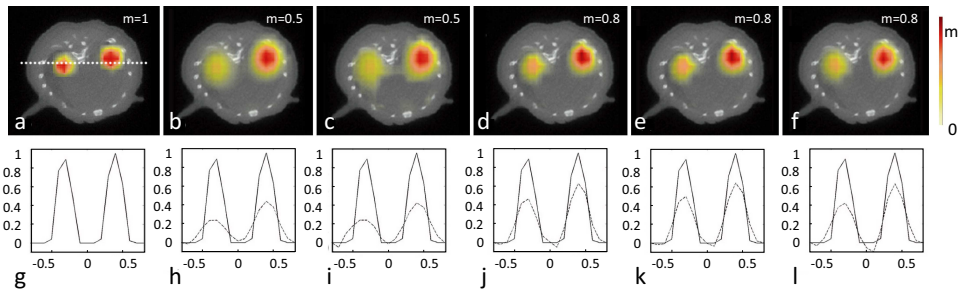

Figure 4.2: Reconstructions of simulated localized signal. a−f) Transversal slices and g−l) profiles. a,g) Simulated signal mapped to voxels. b,h) Tikhonov regularization. c,i) Laplace regularization. d,j) Laplace regularization with weighted segments. e,k) Weighted segments regularization. f,l) Local Laplace regularization with weighted segments.

In the simulation of the distributed fluorescence assumption, which is more challenging for the reconstruction, the simulated fluorescence concentration completely fills the lungs (Figure 4.3a). This implicates that the boundary of the lung area in this case exactly matches the shape of the simulated signal. The results of reconstructions together with profiles are shown in Figures 4.3b-f and h-l, in the same order as was described above. The reconstruction using the standard Tikhonov method has recovered signal in both lungs, but not at equal strength. The signal strength in the left lung is underestimated, the strength in the right lung is slightly overestimated. We attributed this to the difference in size of the two lungs. Analogous to the localized case, the left lung can be considered as the smaller inclusion. It is observed that reconstruction methods using structural information benefit from the exact knowledge of the shape of the fluorochrome concentration. The Laplace method has resolved approximately the correct signal strength, but a source of error with this method is the size of the voxels. In this method, voxels can be part of one segment only, consequently the structural information used in the reconstruction does not exactly match with the underlying anatomy. This results in the blocked shape of the reconstructed concentration. In

contrast, the three methods using the segmentation matrix result in concentration estimates that follow the simulated concentration borders quite accurately. Compared to weighted segments and Laplace+weighted segments, the local Laplace method shows a slightly smoother solution comparable to the smoothness of the Standard Tikhonov solution. However, this does not improve the accuracy of the result. Considering quantification and localization, the Laplace+weighted segments method displays the best result on both aspects.

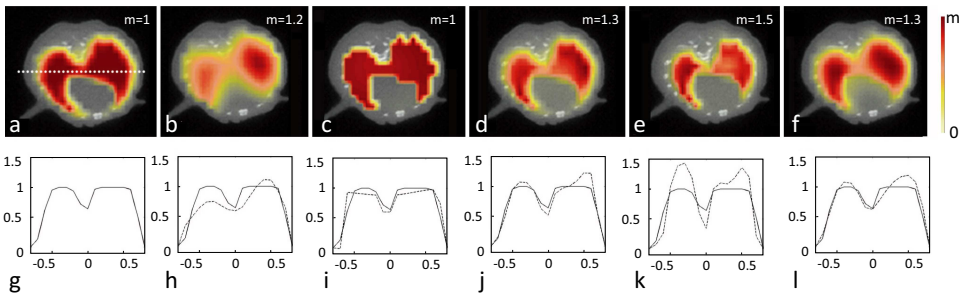

Figure 4.3: Reconstructions of simulated distributed signal. a−f) Transversal slices and g−l) profiles. a,g) Simulated signal mapped to voxels. b,h) Tikhonov regularization. c,i) Laplace regularization. d,j) Laplace regularization with weighted segments. e,k) Weighted segments regularization. f,l) Local Laplace regularization with weighted segments.

The results from the simulations (Figures 4.2-4.3) showed a general improvement in the agreement of simulated and reconstructed fluorescence concentration when hybrid methods were used compared to the standard Tikhonov method. Error estimates between simulation and reconstruction are displayed in Table 4.2. The total error between simulation and reconstruction was minimal for the Laplace+weighted segments method, with a total error of 0.23%. When the weighted segments and Laplace+weighted segments method are considered separately, we find that weighted segments performed equally good compared to Laplace+weighted segments for reconstructing localized objects, with an error of 0.08%, and the Laplace+weighted segments methods performed better when reconstructing distributed activity with an error of 0.15%.

The Laplace method was recently evaluated by Lin et al. [2009] on cylindrical phantom experiments, in which a finer grid was used compared to the

Table 4.2: Error estimates between simulation and reconstruction.

Simulation	Standard Tikhonov	Laplace	Laplace + weighted segments	Weighted segments	Local Laplace
Localized	0.12 %	0.13 %	0.08 %	0.08 %	0.09 %
Distributed	0.37 %	0.25 %	0.15 %	0.30 %	0.25 %
Total	0.49 %	0.38 %	0.23 %	0.38 %	0.34%

1 mm^3 voxels used in the current investigation, and in comparison a larger inclusion of 3.5 mm diameter in a cylindrical phantom of 41 mm diameter. Consequently, the inclusion border could exactly be followed by their fine grid, resulting in accurate reconstructions. These results can be compared to the results for the simulation of the distributed signal as described above. Approximately equal accuracy in quantification was obtained using the Laplace method, although the description of the signal shape is not exact due to the larger voxels. Furthermore, using the weighted segments method and the Laplace+weighted segments method, a fairly accurate result was obtained taking into account the correct segment border, while benefitting from the use of relatively large voxels which considerably reduces the problem size and increases the size of the volume that can be reconstructed within a short calculation time. Compared to the previous study in which the weighted segments method was applied successfully to reconstruction of plaques in the brain as described by Hyde et al. [2010], we observed results of similar accuracy in our simulations as well as in the ex-vivo experiments that are described below.

4.2.4 Evaluation based on ex-vivo mouse experiments

We evaluated the structural penalty matrices on two experimental ex-vivo mouse studies: a brain study and a lung study. All experimental data was acquired using the hybrid FMT-XCT system described in Chapter 1.

The first experiment on which the different structural prior matrices were evaluated was a study of fluorochrome in the brain area of a mouse. A mixture of 1 μM Alexa 750 fluorochrome (Invitrogen) and clinical CT contrast agent was stereotactically implanted in the brain of a euthanized nude mouse at a depth of 4 mm in the right brain lobe. The X-ray CT volume was segmented in three regions: bones, lesion and mixed tissue. The lesion was segmented based on the CT contrast agent in the brain (Figure 4.4a).

The result of the reconstruction without using any regularization (Figure 4.4b) shows a large number of artifacts. A slice of the reconstruction using standard Tikhonov regularization (Figure 4.4c) shows less artefacts and a more pronounced signal from the inclusion. The Laplace-regularized result (Figure 4.4d) shows improved co-localization and shape registration of the inclusion. Using the segment matrix and weights (Figures 4.4e-f) further improves shape registration. The values used for the mean and weights are displayed in the adjacent table. From the reconstructed images it was

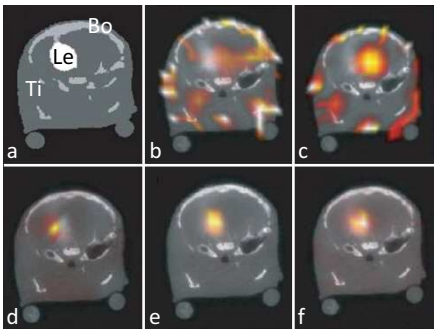

Parameters used in brain study

	Tissue	Bone	Lesion
Mean μ	0	0	4
Weight ω	3.3	3.3	1

Figure 4.4: Results from ex-vivo brain study. a) Segmentation of XCT volume into tissue (Ti), bone (Bo) and lesion (Le). b) Reconstruction without regularization. c) Tikhonov regularization. d) Laplace regularization. e) Weighted segments with mean. f) Laplace regularization with weighted segments.

seen that the background signal in the tissue was forced to the predetermined mean value of zero when the inversion was regularized with weighted segments with mean, while in the smoothed Laplace regularized reconstruction some background signal remains. Based on the above comparison, we concluded that in particular the weighted methods can significantly improve image quality. However, the inclusion of a mean had a relatively strong influence on the reconstruction, implicating a biased solution, and was therefore not investigated further.

For the ex-vivo lung study, we examined a nude mouse with Alexa 680 (Invitrogen) administered intra-tracheal in the lungs. The mouse was imaged with the hybrid FMT-XCT system and afterwards it was sliced in transversal slices using the cryoslicer described in Chapter 1. The image used as validation for the reconstructed images (Figure 4.5a) is a composite of the RGB cryoslice of the mouse reduced to greyscale, and the planar fluorescence image of the same slice (color), corresponding to position 3 in Figure

4.1a. In this image we can distinguish the spinal cord, sectioned ribs, the heart muscle and surrounding heart tissue. A large amount of fluorochrome filled the (as displayed) right lung, and a smaller concentration was present in the left lung. The concentration in the left lung was located near the centre of the mouse, and decreased towards the lung wall. The shape of the fluorescence signal of Figure 4.5a is recognized in the X-ray CT slice (slice 3 in Figure 4.1b), more specifically the cornered shape of the fluorescence signal in the left lung can be found in both images.

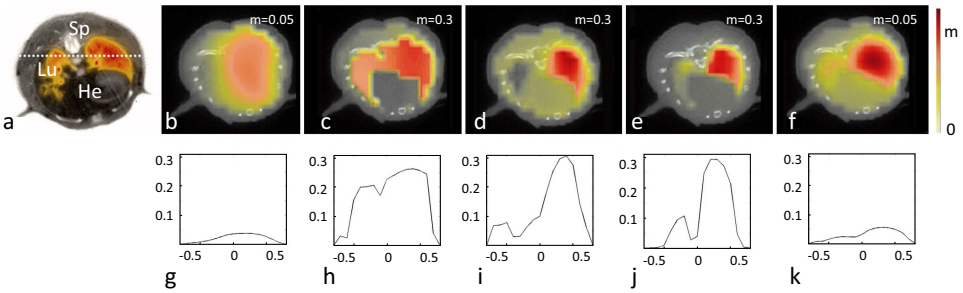

Figure 4.5: Reconstruction of ex-vivo lung study. a−f) Transversal slices and g−k) profiles. a) Cryoslice, RGB image in greyscale, planar fluorescence in color. (Sp=Spine, He=Heart, Lu=Lungs, dotted line indicates position of profiles.) b,g) Tikhonov regularization. c,h) Laplace regularization. d,i) Laplace regularization with weighted segments. e,j) Weighted segments regularization. f,k) Local Laplace regularization with weighted segments.

We observed that a subset of the methods that provided accurate results when using simulated data, did not perform equally well for the ex-vivo study. This difference can be explained mainly by the increased amount of noise, in the form of for example model mismatch and increased normalization error due to auto-fluorescence and scattering. Evaluating each of the reconstruction methods individually, it can be observed that the Tikhonov method and local Laplace method encounter difficulties in recovering the correct position and strength of the signal. This suggests that the local regularization properties of these methods affect their stability and increase the potential for measured data errors to negatively impact the reconstruction result. In the Laplace method on the other hand, a strong connection between voxels is contained. As is observed in Figure 4.5c, this results in a reconstruction that shows similar features as the validation image, Figure 4.5a. Although spatial resolution is low, the reconstruction does show a higher concentration in the right lung compared to the left lung. The reconstruction with the Laplace+weighted segments method shows a strong

signal in the right lung, the signal in the left lung is however partly negative, which can also be attributed to the increased noise in the data. The method that resulted in a reconstruction that corresponds best to the validation image was in this case the weighted segments method, which was found to perform very well under the current noise conditions.
Four slices of the validation experiment are displayed in Figure 4.6a, corresponding to the positions indicated in Figure 4.1a. In slice 1, the topmost slice, the lungs are small compared to lower slices, the heart muscle is not yet visible and we can distinguish shoulder bones. The difference in concentration between left and right lung is more apparent in this slice compared to slice 3. Downwards in the lungs we see the size of the lungs increasing, together with the size of the fluorescence signal. In the lowest slice, slice 4, the fluorescence concentration was widespread but decreased in magnification compared to slice 3. Reconstructions of the slices, as shown in Figure 4.6b show good agreement in 3d as well. The decrease in concentration and the broadening of the signal downward are observed in both validation images and reconstructions. Finally, in the coronal slice, Figure 4.6c it is seen that the signal is co-localized with the lung over the full length of the volume.

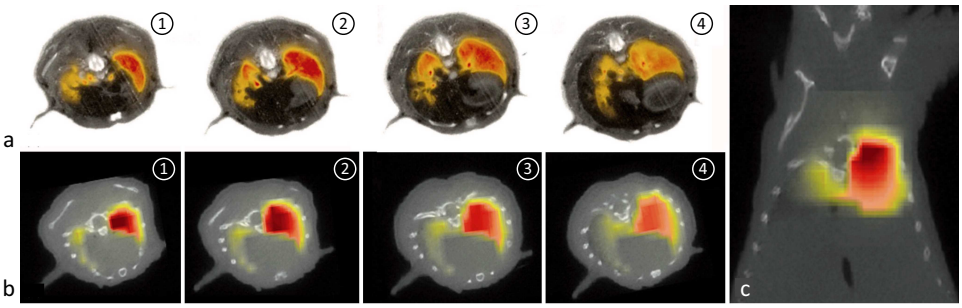

Figure 4.6: 3d FMT-XCT reconstruction and validation for ex-vivo lung study. a) Cryoslice images overlaid with normalized fluorescence image. b−c) Reconstruction using weighted segments regularization. b) Transversal slices. c) Coronal slice.

4.3 Optimal reconstruction method

The simulations and ex-vivo experiments have shown the performance of several hybrid reconstruction techniques that directly incorporate prior information in the FMT reconstruction. We demonstrated that it is possible to accurately resolve the location of the fluorescent bio-distribution using

hybrid FMT-XCT reconstruction techniques. The evaluated methods exhibited varying performance, however, especially for the experimental measurements of mice. Generally the weighted segments method showed good performance under localized and distributed contrast scenarios. Based on the results of the studies described above we selected the weighted segments matrix as the optimal structural penalty matrix. In the implementation described above, the segment weights that were used to calculate the values on the diagonal of the weighted segments matrix were set manually to 1 for the region of interest and about 4 for the remaining regions. The weights placed on the diagonal of the optimal structural penalty matrix are an important variable in the reconstruction method with significant influence on the reconstruction result. The manual assignment of weights introduced user bias. By assigning a low weight to the region of interest we would bias the solution towards our expectations of finding a large fluorescence signal in that region. In order to avoid user bias, we preferred to use a data-driven method to estimate the segment weights.
Hyde et al. [2010] estimated these weights by first performing a low resolution inversion. In the low resolution inversion, the segmentation was used to reduce one dimension of the weight matrix to the number of anatomical segments instead of the number of voxels, resulting in one estimated fluorescence concentration value for each anatomical segment. The values of the weights were calculated from these estimated segment concentrations. Because in most cases the fluorescent signal does not cover a complete anatomical segment, this approach works only in a limited amount of cases, or in cases in which prior information is available on the location of the fluorescence distribution. In this work we did not assume that prior information on the location of the fluorescence distribution is available, and took a different approach.
It is generally assumed that it is possible to obtain a rough indication of the fluorescence distribution also for stand-alone FMT, without using structural information in the inversion. Furthermore, we showed above that it is possible to obtain a rough indication of the fluorescence distribution using Standard Tikhonov regularization, which also does not use structural information in the inversion. Therefore we decided to base the calculation of segment weights on a first inversion that does not use structural information in the inversion, leading to the following reconstruction method:

[1] In the first step, an approximate estimate of the fluorescence distribution is calculated using a reconstruction method that does not use the

structural prior information in the inversion.

[2] The weights are calculated in a data-driven way based on the first reconstruction.

[3] The structural penalty matrix is formulated using the weights.

[4] A second inversion is performed using the structural penalty matrix, resulting in an estimate of the fluorescence distribution.

4.4 Calculation of weights

We evaluated several different approaches for the calculation of the first estimate of the fluorescence distribution and several methods for the calculation of weights based on the first estimate. The evaluation of the approaches is described below, illustrated with a phantom experiment.

4.4.1 Phantom experiment

The phantom experiment is an FMT-XCT measurement of a silicon phantom with two cavities (for phantom preparation see Section 7.2) containing cylindrical fluorescence sources with two different diameters, schematically displayed in Figure 4.7. We filled one cavity of the phantom with a mixture of Intralipid, agar, distilled water and Alexa 680 (Invitrogen) that mimicked the optical properties of the phantom. The concentration of Alexa 680 in the mixture was approximately 200 nm. We inserted the same mixture into a translucent tube with a diameter of 1 mm, and inserted that tube into the other cavity of the phantom. The space between the inserted translucent tube and the cavity wall was filled up with the same mixture without fluorochrome.

We created two different segmentations for the reconstruction. For the first segmentation (segmentation b) we manually segmented the two tubes based on the X-ray CT volume (Figure 4.8a), and added two additional cylindrical segments, making in total 4 cylindrical segments (Figure 4.8b). In the second segmentation (segmentation c) we mimicked an anatomical segmentation by creating a lung, heart and bone area. The two tubes were contained in the lung area and did not make up a separate segment (Figure 4.8c). The segmentation was constant over all slices of the phantom. Calculation of the forward model was done once; the same forward model was used for all

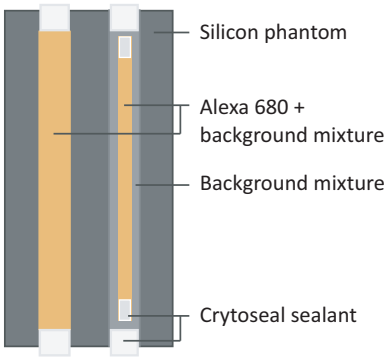

Figure 4.7: Phantom configuration. Silicon phantom with 2 cylindrical cavities. One cavity is filled with a fluorescent mixture (Alexa 680). A translucent tube with a smaller diameter is placed in the second cavity. The cavity is filled up with the same mixture without the fluorochrome.

inversions. We assigned optical properties $\mu_a = 0.2$ cm^{-1} and $\mu_s' = 12$ cm^{-1} to all segments for the calculation of the forward model. Detector separation was set to 0.8 mm, voxel size to 0.75 mm^3.

4.4.2 First inversion

For the first estimation of the fluorescence distribution we evaluated five different reconstruction methods, using three different inversion algorithms. The first method we evaluated was reconstruction using the ART algorithm. ART is a well-known reconstruction algorithm for tomographic problems [Kak and Slaney, 2001]. ART is based on successive projection of the estimate of the fluorescence distribution on hyperplanes defined by the rows of the weight matrix $\mathbf{W}$. The access order of the rows can be chosen in several different ways, here we applied fully randomized ART, with lambda parameter 0.5, 20 iterations and no initial solution. The result of reconstruction with ART is displayed in Figure 4.8d.
The second approach that we evaluated was published in Hyde et al. [2010]. The method actually does use the segmentation in the first step, but because it was presented in [Hyde et al., 2010] as part of the weighted segments method that includes the diagonal matrix described above, we include it here for completeness. This method involved the solution of a low resolution problem as an initial estimate of the fluorochrome distribution. Instead of calculating an estimation of the fluorescence distribution for each voxel, the volume was split up into the segments, and the weight matrix is summed for the rows that belonged to one segment, in this way arriving at a lower

dimensional weight matrix which, when inverted, returned one value per segment. Inversion was done using the MRNSD algorithm [Hyde et al., 2010], which applies to small dimensional problems and returns only non-negative solutions. We applied this method using both segmentations as described above. The result of reconstruction with segmentation b is displayed in Figure 4.8e, and the result of reconstruction with segmentation c in Figure 4.8f. The last method that we investigated was reconstruction using the LSQR method, as was described above, with the identity matrix as the regularization matrix ($\mathbf{L} = \mathbf{I}$). We performed 50 iterations, and calculated the solution for 200 values of the regularization parameter λ, the values were calculated relative to the norm of the weight matrix. We analyzed the result for two values of the regularization parameter: small ($\lambda_{45} = 0.0389$) and medium ($\lambda_{65} = 0.1966$), see Figure 4.8g and 4.8h.

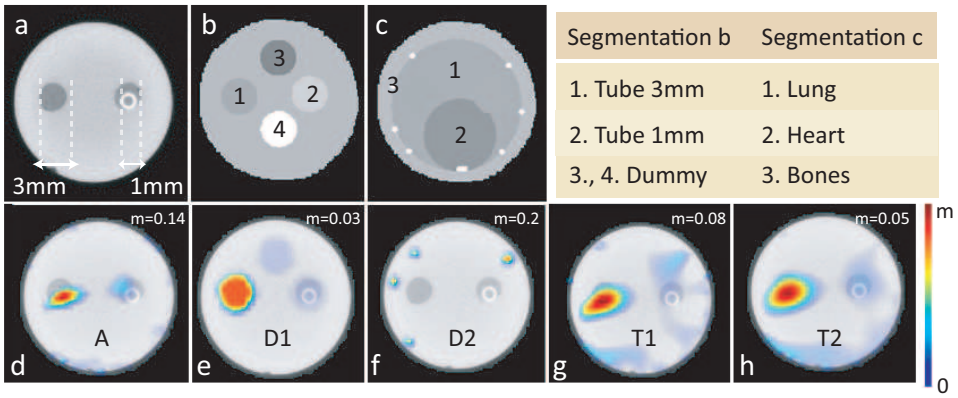

Figure 4.8: Reconstruction results using different methods for calculation of weights. a) XCT slice of phantom with two tubes of 3 mm diameter, one filled with a fluorescence mixture, and the second with a smaller tube that is filled with the fluorescence mixture. b) Segmentation b, containing four cylindrical segments. c) Segmentation c, which mimics a typical segmentation for the thorax region. Table) Legend for segmentations b and c. d−h) Reconstructed fluorescence distribution in color overlaid on XCT slice, reconstructed with d) ART, e) segmentation b and MRNSD, f) segmentation c and MRNSD, g) LSQR with a small regularization parameter and h) LSQR with a medium regularization parameter.

4.4.3 Calculation of weights based on first inversion

Weights were calculated based on each of the first estimates of the fluorescence distribution. The estimated fluorescence distribution consisted of a 3d voxelized volume with n slices in the z-direction along the phantom. Before

we calculated the weights, we eliminated sources of known error from the reconstructed volume: the top slice, bottom slice and the first line of voxels along the boundary were excluded, voxels with a negative value were set to zero. We set the range of the calculated weights between 1 and 4, because a signal/background ratio of 4/1 could reasonably be expected. The weight for the tissue not belonging to any segment was set to 4. We evaluated the weights calculated using three different measures: the sum, maximum and average in a segment using the segment matrix $\mathbf{C}$ and the reconstruction result $\mathbf{x}$:

$$\text{average}_{\text{segment}} = \frac{\mathbf{Cx}}{\sum \mathbf{C}}, \tag{4.4.9}$$

$$\max_{\text{segment}} = \max\left(\mathbf{Cx}\right), \tag{4.4.10}$$

$$\text{sum}_{\text{segment}} = \sum \mathbf{Cx}. \tag{4.4.11}$$

Using these values calculated for each segment, weights in the range 1 to 4 were calculated:

$$\mathbf{w} = \left[\frac{\mathbf{m}^{-1} - \min(\mathbf{m}^{-1})}{\max(\mathbf{m}^{-1} - \min(\mathbf{m}^{-1}))}\right] \times 3 + 1, \tag{4.4.12}$$

with $\mathbf{m}$ one of the measures described above. The values for the weights $\mathbf{w}$ calculated using the different options for $\mathbf{m}$ are displayed in Tables 4.3a-b. The aimed values for the weights are displayed in the last column. The low resolution reconstructions (D1 and D2) did not result in satisfying results. ART (A) showed a quite good performance, however when more model mismatch is introduced, ART becomes unstable and the chance of approaching a local minimum increases. On the other hand, the LSQR method (T1 and T2) gave reasonable results as well, especially for a medium value of the regularization parameter (T2). In the application section we have used the sum and average to calculate the weights using a medium regularization parameter (T2).

4.4.4 Calculation of the second inversion

The second inversion was calculated using the weights T2, calculated based on the LSQR algorithm with medium lambda and using the sum over the segments as the indicative measure. The reconstruction results with both segmentations are displayed in Figure 4.3d and 4.3e. The reconstruction

Table 4.3: Quantitative analysis of different methods for calculation of weights. a) Weights calculated based on segmentation b using different methods. b) Weights calculated based on segmentation c using different methods. c) Calculated ratios of value reconstructed for 3 mm tube over 1 mm tube. d) Final reconstruction using weights based on segmentation b, highlighted in Table a. e) Final reconstruction using weights based on segmentation c, highlighted in Table b.

		Sum			Max			Average			
Segmentation b	D1	A	T1	T2	A	T1	T2	A	T1	T2	Aim
1.	1	1	1	1	1	1	1	1	1	1	1
2.	4	1.03	1.24	1.04	1.23	2.29	1.35	1.03	1.24	1.04	1
3.	3.30	4	1.31	1.25	4	2.10	1.48	4	1.31	1.25	4
a 4.	4	4	4	4	4	4	4	4	4	4	4
Segmentation c	D2	A	T1	T2	A	T1	T2	A	T1	T2	Aim
1.	4	1	1	1	1	1	1	1	1	1	1
2.	4	4	1.05	1.05	4	1.63	1.24	4	2.24	2.29	4
b 3.	1	4	4	4	4	4	4	4	4	4	4
3mm/1mm	D1	A	T1	T2	A	T1	T2	A	T1	T2	Aim
initial	8.42	5.91	11.0	5.12	2.76	6.45	4.24	5.91	11.0	5.12	1
final-b			5.75	4.37		3.41	3.02		5.75	4.37	1
c final-c			8.05	3.61		4.64	3.18		8.05	3.61	1

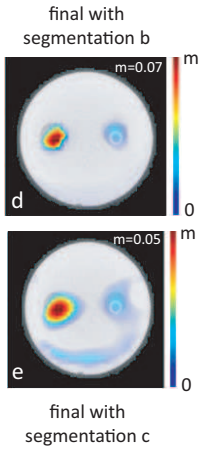

with segmentation b, in which we supposedly know what the location of the two tubes is, performed better than the reconstruction with segmentation c, in which we used only anatomical segments.

4.4.5 Quantification

Although the tubes in the experiment were filled with the same concentration of fluorochrome, they were not reconstructed with the same magnitude in any of the evaluated cases. As a quantitative measure, the maximum reconstructed value in the tube performed best, which has a value closer to 1 than the other measures. In the final reconstructions, the difference in quantification is proportional to the difference in diameter between the two tubes (3/1). A similar disagreement was observed for the small and large simulated inclusion in the local simulation that was used for the evaluation of structural penalty matrices and the ex-vivo lung experiment (Section 4.2). This indicates that when a quantitative measure is required, it is preferable to compare objects of equal size. Results of quantification experiments with objects of equal size are shown in Chapter 7.

4.5 Summary and Conclusions

In this chapter we developed an optimal inversion method for hybrid FMT-XCT. The LSQR inversion algorithm that we used in this research is a stable method, robust to noise, and it facilitates the use of a regularization matrix. We investigated how to best formulate the regularization matrix using the structural information that we obtained from the anatomical segmentation of the X-ray CT data. We evaluated different implementations on simulated data and experimental data of ex-vivo experiments acquired with the hybrid FMT-XCT system. We found that the penalty matrix that displayed the most consistent and robust performance for the largest application range was a diagonal matrix, filled with voxel weights that were based on a set of anatomical segment weights. Because a diagonal matrix is straightforward to invert, we could effortless transform the regularized problem into standard form, and enable fast inversion. We developed a data-driven method for the calculation of the segment weights in order not to bias the solution. As a measure for calculating the weights, we used the sum or average reconstructed value per segment, based on a first reconstruction that does not use structural information in the inversion. As a quantitative measure we identified the maximum value per segment as a good indicator, and found that it is important to compare objects of equal size.

5

Estimation of attenuation coefficients

5.1 Introduction

Light that propagates through a mouse is attenuated through scattering and absorption events. Biological tissue can have many different consistencies, and each tissue type has different attenuation properties. We include light attenuation properties in the calculation of the forward model (see Section 2.2) in order to increase the accuracy of the reconstruction. In this chapter we describe how we obtained the attenuation coefficients that were used for the calculation of the forward model.

The attenuation properties of biological tissue can be estimated in various ways. One way to obtain values for the attenuation coefficients is by a method termed Diffuse Optical Tomography (DOT). In DOT an inversion method is used to estimate the attenuation coefficients from measurements at the excitation wavelength. DOT could result in an accurate estimation of the optical properties, however, the problem is difficult to solve because it is ill-posed. In particular, it is impossible to obtain an estimate for both scattering and absorption coefficient simultaneously when operating in Continuous Wave (CW) mode (as in the hybrid FMT-XCT system). As a result the scattering coefficient is often held constant, while the absorption coefficient is estimated. Using these estimates leads only to improved reconstruction results if the absorption coefficient is heterogeneous and the scattering coefficient homogenous [Barber et al., 2010]. However in biological tissue

the scattering coefficient is heterogeneous as well. Several publications exist where other methods have been applied to estimate the absorption and scattering coefficient of anatomical regions for human or animal tissue [Cheong et al., 1990; Beek et al., 1997; Alexandrakis et al., 2005]. Optical properties determined for humans or other animals are not necessarily identical to the optical properties in mice. And even when the optical properties are estimated for mice using a certain method, it is not guaranteed that these optical properties will lead to optimal reconstruction results because the forward light propagation model can be based on approximations that are not consistent with the method chosen for the estimation of optical properties. Optical properties that are exactly correct for reconstruction of the fluorescence distribution are consequently not available in literature. Fortunately, the reconstruction method that we use is not very sensitive for small errors in the estimated optical properties. It has been shown that the normalized Born approximation [Ntziachristos and Weissleder, 2001] that we use in our reconstruction method reduces the effect of heterogeneous optical properties on the reconstruction of the fluorescence distribution considerably [Soubret et al., 2005]. Furthermore, in a recent paper by Hyde et al. [2009b] that examined the effect of optical properties on the reconstruction quality in the context of the normalized Born approximation using priors, it was shown that it is advantageous to use heterogeneous optical properties over homogeneous optical properties, and that using averaged published values for each tissue type in the murine chest offers reconstructions with 5% error increase for 15% optical property error. We considered this an acceptable error for the reconstructions, especially when considering the added benefit that no additional method needs to be implemented for measuring the optical properties for each individual mouse.
Therefore we use a table lookup method for the assignment of optical properties in this research, using a predetermined set of optical properties. We investigated the range of published values for optical properties and, using this range, searched for a set of optical properties that would lead to optimal reconstruction results.

5.2 First set of optical properties for the thorax region

The first set of optical properties that we used for reconstructions was derived from a paper by Niedre et al. [2006]. Niedre et al. performed an in-vivo study of the optical scattering and absorption properties for the thorax area of a mouse. The optical system used for estimating the properties was a

high-speed gated imaging system with a femto second laser source at 732 nm. With this system it was possible to acquire photon profiles as a function of time and radial position from the source. Similar profiles calculated with time-resolved diffusion theory were fitted against the measured profiles in order to find the attenuation coefficients. For estimation of the optical properties per organ, the calculated absorption and reduced scattering images of the mice were compared against coregistered MRI images of the same animal. The optical properties that were estimated with this method are displayed in Table 5.1. The midrange optical properties, used by Hyde et al. [2009b] based on [Niedre et al., 2006] are summarized in Table 5.1 as well, and these were used in the evaluation of structural penalty matrices (Section 4.2).

Table 5.1: Published values for optical properties of the thorax area. The first set of optical properties used for reconstructions consisted of the midrange optical properties published by Hyde et al. [2009b]

Publication	Coefficient	Tissue	Bone	Lung	Heart	Liver
Niedre et al. (2006)	μ_a [cm^{-1}]	0.3		0.2 - 0.3	0.3 - 0.4	0.4 - 0.6
	μ_s' [cm^{-1}]	10		25 - 35	20 - 25	10 - 15
Hyde et al. (2009)	μ_a [cm^{-1}]	0.3	0.1	0.25	0.35	0.5
	μ_s' [cm^{-1}]	10	20	30	23	13

5.3 Second set of optical properties for the thorax region

The second set of optical properties was a refinement of the first set of optical properties. In an investigation by Pyka et al. [2011], the effect of scattering in particular on the quality of the reconstruction was evaluated using simulations and phantom experiments. It was observed that the effect of errors in the assumed scattering coefficient is larger than the effect of absorption. Furthermore, it was observed that an overestimation of the scattering coefficient results in a smaller error in the reconstruction than an underestimation of the scattering coefficient. For the refinement of optical properties, datasets measured with hybrid FMT-XCT were reconstructed using different variations of optical properties, until a good match with the cryoslices was found. We took into account the findings described above, and varied only the reduced scattering coefficient, assuming that the changes

in the absorption coefficient have only a very small influence. In case the difference between reconstruction results was not evident, we took into account that an overestimation of the scattering coefficient results in a smaller error than an underestimation. The second set of optical properties is displayed in Table 5.2. We have set the attenuation coefficients for the liver equal to the heart region, because without the use of contrast agent, it is difficult to define the border between these two regions.

Table 5.2: Second set of optical properties used for reconstructions of the thorax area.

	Coefficient	Tissue	Bone	Lung	Heart	Liver
Refined properties	μ_a [cm^{-1}]	0.3	0.2	0.25	0.35	0.35
	μ_s' [cm^{-1}]	15	15	27.5	17.5	17.5

5.4 Wavelength dependence of optical properties

In the thorax area we have used identical optical properties for excitation and emission wavelength. The two wavelength ranges that we used in this research are 680-710 nm, and 750-800 nm. Including a difference in optical properties at excitation and emission wavelength could increase the accuracy of the forward problem. This difference is only relevant in case the optical properties are inhomogeneous throughout the volume. A difficulty with the implementation and accurate validation of the parameters is that the optical properties of mice are only known by approximation, and less is known about the exact variation of the optical properties with wavelength. Matcher et al. [1997] investigated the wavelength dependent optical properties of human tissue in-vivo in the range 760-900 nm. For the reduced scattering coefficient, they found a decrease with wavelength of less than 10% over the range 760-900 nm, or about 5% per 50 nm. We assumed that this value applies to both of the used wavelength ranges. To estimate the difference in absorption coefficient with wavelength we assumed that the absorption properties are correlated with the hemoglobin curves (see for example http://omlc.ogi.edu/spectra/hemoglobin/summary.html), assuming an oxygenation of 80%. For the range 680-710 nm, the absorption coefficient decreases quite steeply, while in the 750-800 nm range the absorption coefficient increases. We took these differences in optical properties

between wavelengths for the range 680-710 nm into account when estimating the optimal attenuation parameters for the brain region, described below.

5.5 Optical properties for the brain region

For the brain region we performed a similar variational analysis as was done for the thorax region, using a dataset that is part of the brain cancer study described in more detail in Section 8.4. For the estimation of optical properties, the brain was segmented in three anatomical regions: bone, brain (tissue inside skull) and remaining mixed tissue. We varied the scattering properties for the brain and mixed tissue segment, and the absorption coefficient for the brain segment. The results of several variations are displayed in Figure 5.1. The optical properties used for the calculation of the forward model are displayed above and below the transversal slices of the reconstruction. Italic green and red values indicate the value that is changed

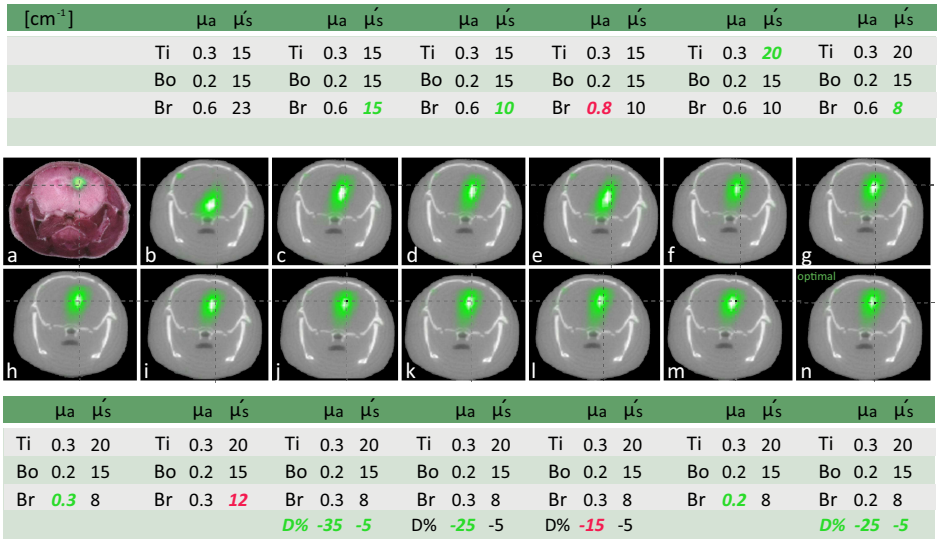

Figure 5.1: Optical property variations for estimation of the optimal absorption coefficient, reduced scattering coefficient and difference in coefficients between excitation and emission wavelength. a) Validation cryoslice. Planar fluorescence signal in green overlaid on RGB cryoslice. b-n) Transversal slices of FMT-XCT reconstruction. The optical properties displayed next to the slices were used for the calculation of the forward model. Italic green and red values indicate a changed value. Green values indicate a change with a positive effect, red values indicate a change with a negative effect.

compared to the previous reconstruction in the row. Green values indicate a change with a positive effect on the correspondence between cryoslice and estimated fluorescence distribution, while red values indicate a change with a negative effect. We started out with a highly scattering and absorbing brain segment ($\mu_s' = 23$ cm^{-1} and $\mu_a = 0.6$ cm^{-1}) [Raymond et al., 2009; Johns et al., 2005], but found through variation that the optimal parameters for FMT-XCT reconstruction of the brain area are actually a low reduced scattering and absorption coefficient ($\mu_s' = 8$ cm^{-1} and $\mu_a = 0.2$ cm^{-1}) for the brain segment. We found that the mixed tissue in this area is more scattering than the mixed tissue in the thorax region ($\mu_s' = 20$ cm^{-1}), which is possible because the tissue in the brain area has a different consistency. We assigned a scattering difference between excitation and emission wavelength of -5%, following published values as described above. We observed optimal reconstruction performance when an absorption difference of -25% was applied. For the study of brain cancer described in Section 8.4 we used the optical properties displayed in Table 5.3, corresponding to the reconstruction displayed in Figure 5.1n.

Table 5.3: Optical properties used for the reconstructions of the brain area.

	Brain	Bones	Mixed tissue	Emission wavelength
μ_a [cm^{-1}]	0.2	0.2	0.3	-25%
$\mu's$[cm^{-1}]	8	15	20	-5%

5.6 Summary and Conclusions

In this chapter we described the optical properties that we used for the reconstruction of the fluorescence distribution. We used two different sets of optical properties for the reconstruction of the thorax region; the second set was a refinement of the first set. The first set was used for the evaluation of structural penalty matrices, described in Section 4.2. The second set was used for the reconstructions of the applications in the thorax region, described in Chapter 8. We defined a set of parameters for reconstruction of the brain area using a mouse model with a very localized bright fluorescent signal in the brain produced by fluorescent proteins. In order to further refine the optical properties for the thorax region we could perform similar experiments with a localized bright target in the thorax area.

6

Hybrid background fluorescence correction

6.1 Introduction

In the previous chapters, we have discussed how the X-ray CT data can be used to form a structural penalty matrix to increase the accuracy of the estimated fluorescence distribution. We also described how to incorporate heterogeneous diffusion properties of small animals in the reconstruction algorithm in order to further improve reconstruction accuracy. Another difficulty when imaging in the near-infrared range is the presence of background fluorescence. In this chapter we describe how the X-ray CT information can be used to reduce the influence of background fluorescence.

Background fluorescence can originate from internal factors such as for example food and skin. An additional amount of background fluorescence is introduced with the use of targeted probes. Targeted fluorescent probes are already fluorescent upon injection. After circulation through the body, the probe will accumulate at the target site, for example a tumor, resulting in a larger concentration of probe at a specific site, while a remaining amount of probe will continue circulating through the body until it is secreted. The concentration of probe that remains in the circulation is generally very low (order 10 nM), it is however enough to cause artifacts in the reconstruction of the fluorescence distribution which can mask the actual target that is the subject of the imaging study. In order to overcome this limitation, different approaches for the reduction of the influence of background fluorescence on

the reconstruction result have been investigated in the past.
Methods were developed that constrained the inversion step of the reconstruction of the fluorescence distribution in the presence of background fluorescence [Chang et al., 1998], while other methods were based on preprocessing the measured data before use as input for the inversion [Deliolanis et al., 2011].
Gao et al. [2005] calculated a background fluorescence correction based on the normalized Born ratio for a slab geometry. All data points in a CCD image corresponding to a source position were plotted as a function of radial distance from the source, and a cubic polynomial was fit to the normalized Born values. This was repeated for all sources, and the average of the fitted polynomials as a function of distance was subtracted from the normalized Born values for each source. Improvements were shown in the reconstruction result in terms of artifact reduction, quantification and detectability of targets.
In a follow-up paper by Soubret and Ntziachristos [2006] several subtraction methods were evaluated using linear relationships that were derived from the Diffusion Equation combined with the normalized Born ratio, for a slab geometry. An underlying assumption in their work was that the background fluorescence level and the imaged object were both homogeneous. One of the schemes that they evaluated was a data pre-processing method, in which they assumed a linear relationship between the distance from the source to a detector and the measured normalized born values corresponding to the background fluorescence. A proportionality constant was calculated by a linear fit of the measured normalized born values.
In this chapter we extend the second scheme evaluated by Soubret et al. for the 360° acquisition geometry of the hybrid FMT-XCT system, and use the 3d anatomical information obtained from X-ray CT to increase accuracy of the subtraction scheme. The calculation of the distances between source and detector is based on the X-ray CT volume. For the calculation of the proportionality constant we use the same linear relationship between distance and background fluorescence. We use the calculated constant together with the X-ray CT volume to estimate full images which can be subtracted directly from the measured normalized CCD images. Furthermore we defined a data-driven estimation method for the calculation of the proportionality constant. The background fluorescence subtraction was implemented as a pre-processing step in the hybrid FMT-XCT reconstruction method.
We describe the steps in the subtraction method, show the result on quan-

tification using ex-vivo mouse measurements, and apply the method to an in-vivo study of mice with small lung tumors.

6.2 Expression for homogeneous background fluorescence

For the case of a homogeneous medium with a constant fluorescence level throughout the medium, Soubret and Ntziachristos [2006] have derived a linear relationship between the born ratio and the distance from source to detector, given by:

$$U^{nB}_{target}\left(\mathbf{r}_d, \mathbf{r}_s\right) = \left[U^{nB}_{target}\left(\mathbf{r}_d, \mathbf{r}_s\right)\right]_{measured} - a_{fit}\left\|\mathbf{r}_d - \mathbf{r}_s\right\|, \qquad (6.2.1)$$

where $\|\mathbf{r}_d - \mathbf{r}_s\|$ is the distance from a source at $\mathbf{r}_s$ to a detector at $\mathbf{r}_d$, a_{fit} is a constant proportional to the constant fluorescence level in the medium and $U^{nB}_{target}\left(\mathbf{r}_d, \mathbf{r}_s\right)$ is the data corrected for background fluorescence. The parameters that need to be estimated are the proportionality constant and the distance from source to detector. In this work we use the X-ray CT volume for the calculation of the distances and the complete set of 360° imaging data to estimate the proportionality constant in a data driven way.

6.3 Correction method

The correction method consisted of 1) the extraction of surfaces from the X-ray CT volume, 2) calculation of the distances from each source position to the other side of the volume, 3) an estimation of the proportionality factor, and 4) subtraction of images.

6.3.1 Calculation of distances

The calculation of the distance between source and detector was based on the 3d XCT volume acquired with the hybrid FMT-XCT system. For each gantry angle, first the front and back surface of the imaged medium were extracted from the XCT volume. For the calculation of the front and back surface, all points of the boundary of the XCT volume were projected onto the camera or source plane using a parallel projection and a factor for linear scaling between the coordinates in the XCT volume to the pixels in the camera image. The extracted surfaces were interpolated on a grid of 512×512 points corresponding to the pixels in the CCD camera image. The source position was projected onto the extracted surface at the side of the source.

The 3d Euclidean distance from that point to all points on the surface at the side of the detector was calculated. The 512×512 image of distances represents the term $\|\mathbf{r}_d - \mathbf{r}_s\|$ for each pixel in the camera image.

6.3.2 Automatic data driven calculation of a

One proportionality factor was calculated per studied mouse. The proportionality factor was calculated based on all images in an acquired data set. On average, 18 sources were scanned for 18 projection angles, resulting in a total of around 324 images. A region of interest in the image was used for the calculation of the proportionality factor. The region of interest was automatically selected as the area that was covered by the scanned sources, assuming this is an area that does not contain hair or other undesired sources of error. In case the mouse would contain only background fluorescence and no target, the following relationship holds:

$$a_{estimate} = \frac{\|\mathbf{r}_d - \mathbf{r}_s\|}{\left[U^{nB}_{target}(\mathbf{r}_d, \mathbf{r}_s)\right]_{measured}}. \tag{6.3.2}$$

We used the above relationship to determine the proportionality factor in the following way. First a histogram of $a_{estimate}$ was made for all points in the region of interest in all images of one dataset. This resulted in a histogram of the order of 10^7 datapoints. The bin for which the histogram shows a peak would be the value that occurs most over all images and can be used as a_{fit}:

$$a_{fit} = \text{bin}(\max(\text{hist})). \tag{6.3.3}$$

In this way, we arrive at a robust and fully data driven method to determine a_{fit}.

6.3.3 Subtraction of images

The last step in the background correction was the subtraction of the background images from the acquisition data, using the proportionality factor and Equation 6.3.2.

6.4 Example

The different steps in the calculation of the background fluorescence subtraction are illustrated in Figure 6.1. First the front and back surfaces of

the imaged mouse were calculated for each projection angle (Figure 6.1a), based on a scaled projection of the X-ray CT volume along the optical axis. The source positions were projected onto the surface at the side of the laser, and the 3d Euclidian distance was calculated from that point to the surface at the side of the detector, resulting in an estimate of the normalized background fluorescence (Figure 6.1c) in arbitrary units. The calculated image was divided by the original normalized acquisition image (Figure 6.1d). All points in a region of interest of the divided image were binned and saved for all sources of all projection angles. A histogram was formed out of all points (Figure 6.1e), and the maximum of this histogram was used as the subtraction factor. The normalized background fluorescence was subtracted from the acquired normalized background fluorescence for each source position, resulting in the corrected data (Figure 6.1f).

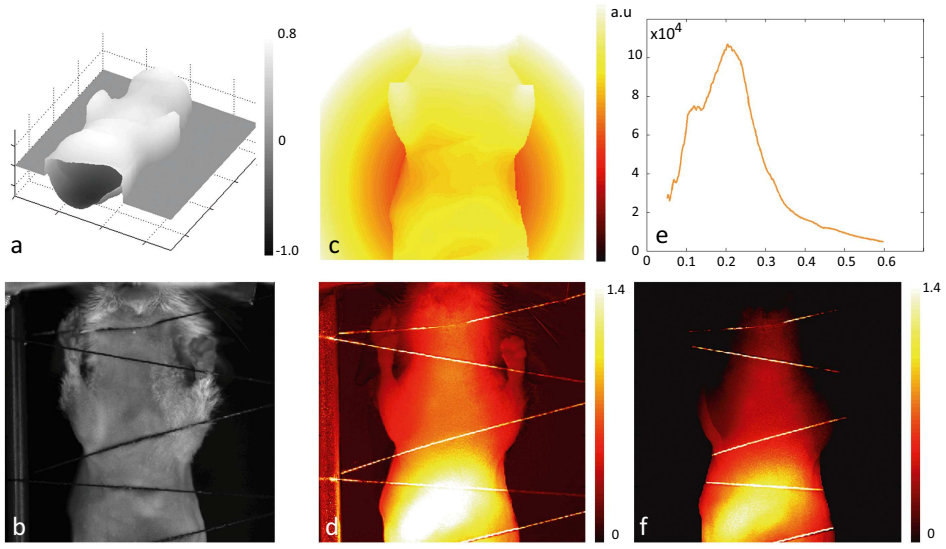

Figure 6.1: Steps in the calculation of a dataset corrected for background fluorescence. a) Example of calculated surfaces at the side of source and camera for one gantry angle (205°), units in cm. b) White light image of the mouse (chest side). c) Calculated background fluorescence image for one source based on the distances from source to camera surface. d) Normalized acquisition image. e) Histogram of background fluorescence / acquisition image per pixel in a region of interest on the mouse surface. f) Normalized acquisition image after subtraction of calculated background fluorescence image.

6.5 Effect on quantification

We evaluated the effect of background fluorescence subtraction on the quantitative properties of FMT-XCT using an ex-vivo study of a mouse with a fluorescent tube inserted in the aesophagus (Figure 6.2). The mouse was prepared by Nikolaos Deliolanis. The tube was filled with a mixture of Intralipid, India ink, water and 1) a high concentration fluorochrome (Figures 6.2a-d), 2) a low concentration of fluorochrome (Figures 6.2e-h) and 3) no fluorochrome (Figures 6.2i-l). Because the same mouse was used for all experiments and the mouse was not moved when interchanging the tube, the background fluorescence images (Figure 6.2m) only needed to be calculated once. The background corrected acquisition images for the two measurements involving a tube filled with fluorochrome (Figures 6.2b,f) show a clear indication of the tube, whereas the background corrected acquisition image of the control measurement shows almost no fluorescence signal leftover (Figure 6.2j). The background subtraction has a positive effect on the reconstructed images (Figures 6.2c-d, g-h, k-l). After background subtraction, the quantification of the values reconstructed for the tubes is not affected (Figure 6.2o), but the amount of artifacts due to the background fluorescence is reduced (arrows in Figures 6.2c-d, g-h, k-l). The reduction of artifacts is especially important in case the actual signal that we are looking for is small. This will be illustrated below for the in-vivo study of a lung cancer model.

6.6 In-vivo study of K-ras lung cancer model

In young K-ras mice of 4 weeks old, tumor targets are around 0.8 mm, which is close to the maximum resolution that is expected to be achievable (see Section 8.3). Not only are the targets in young K-ras mice relatively small, the targets are not easily distinguished from the background fluorescence level either. Figures 6.3a-b show cryoslicing results for a 4 week old K-ras mouse, two tumors are indicated with arrows. The corresponding FMT-XCT reconstructions with and without the background correction applied to the data are displayed in Figures 6.3c-f. There is a clear reduction in artifacts between the reconstructions based on uncorrected and corrected data for the 4 week old K-ras mouse. The resulting corrected reconstruction corresponds well with the validation image (Figure 6.3b).

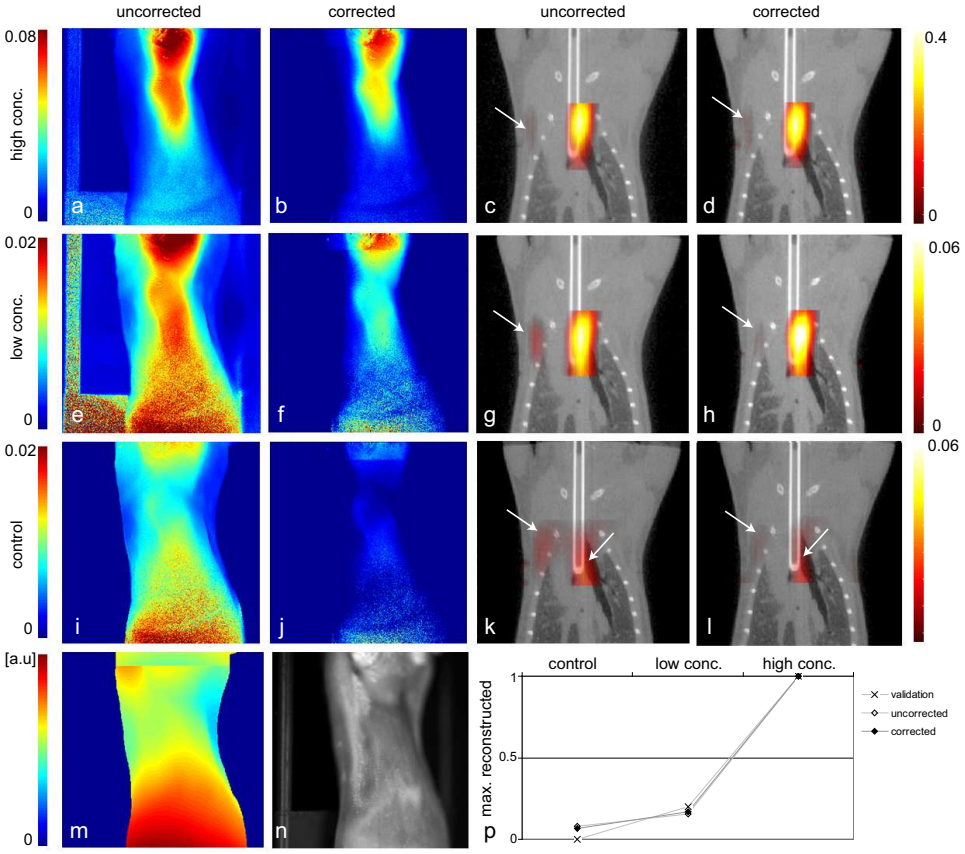

Figure 6.2: Background correction applied to mouse with tube in aesophagus, filled with a mixture containing a-d) fluorochrome in high concentration, e-h) fluorochrome in low concentration, i-l) no fluorochrome. a,e,i) Normalized acquisition image for one source. b,f,j) Background corrected normalized acquisition data. c,g,k) Reconstruction using uncorrected acquisition data and d,h,l) using corrected acquisition data (arrows indicate artifacts). m) Calculated background fluorescence image. n) White light image. p) Graph of maximum reconstructed values, normalized to high concentration fluorescence.

6.7 Summary and Conclusions

We presented an X-ray CT based method for the data-driven estimation of a background fluorescence correction for pre-processing of Fluorescence Molecular Tomography data before reconstruction of the fluorescence biodistribution. Application of the implemented data-driven correction for background fluorescence resulted in improved estimates of the fluorescence biodistribution ex-vivo and in-vivo. Results of the ex-vivo mouse study showed

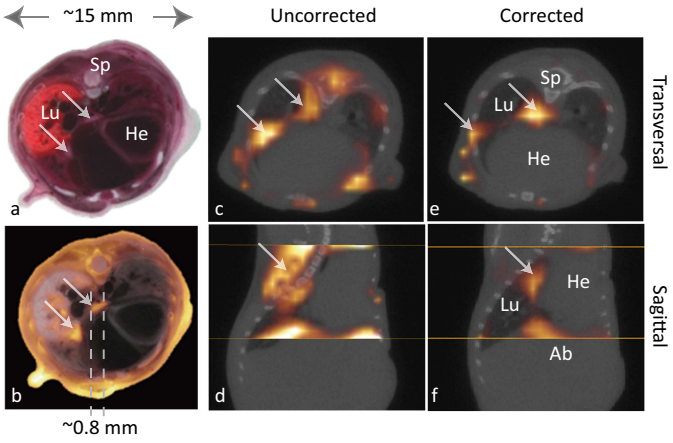

Figure 6.3: Hybrid FMT-XCT reconstruction and validation results for 4 week old K-ras. a) RGB cryoslice image. b) Validation cryoslice showing planar fluorescence in orange. c,e) Transversal slices and d,f) sagittal slices of FMT-XCT reconstruction based on c,d) uncorrected data and e,f) corrected data. (Arrows indicate tumors, Sp=Spine, Lu=Lung, He=Heart, Ab=Abdomen.)

that the background correction decreases the amount of artefacts in the reconstruction, while it does not compromise quantification ability. The in-vivo study displayed that it is possible to reconstruct small targets expressing a low signal compared to the background fluorescence level using the correction method. The pre-processing of hybrid FMT-XCT data using the described method increases the imaging capabilities of FMT-XCT, leading to a wider range of possibilities for future directions of study. In the calculation of the background fluorescence correction, we assumed a homogeneous object with homogeneous optical properties and homogeneous background fluorescence, which allowed us to use a simple calculation for the estimation of the background fluorescence. The presented method could be extended for cases in which the background fluorescence is inhomogeneous using for example the anatomical segmentation of the X-ray CT data for the development of a heterogeneous or layered homogeneous model.

7

Quantification experiments

7.1 Introduction

We performed several groups of quantification experiments with fluorescent dyes and probes in different concentrations, including phantom experiments, ex-vivo mouse experiments and in-vivo mouse experiments. The reconstructed signal strength in fluorescence tomography is generally assumed to be a linear function of probe concentration, and pico-molar concentrations can be detected [Ntziachristos and Weissleder, 2002; Graves et al., 2003]. The quantification experiments described below were carried out as part of several different studies, and are combined here to give an overview of the quantification abilities in different types of experiments.

7.2 Phantom preparation

Three types of phantoms are often used in optical imaging: agar phantoms, silicon phantoms and resin phantoms. The advantage of agar phantoms is that they are easy and fast to produce. This provides the flexibility to experiment with different shapes and different (heterogeneous) optical properties of the phantom. Agar phantoms degenerate after a limited amount of time and are therefore not reusable over a long time period. The preparation of silicon phantoms and resin phantoms takes more effort and time than the preparation of agar phantoms, but they have the advantage that they are reusable. In this work we mainly used silicon phantoms.

The recipe for creating silicon phantoms was based on an article from Baeten

et al. [2007]. Silicon (EcoflexTM 0030 Supersoft silicone rubber Part A and B, Smooth-On, Inc, Easton, PA) was used as the solid base material. To adjust the optical properties of the silicone rubber, white and black silicone pigments (Smooth-On, Inc, Easton, PA) were added to the silicon. The phantoms were modelled to obtain optical properties of $\mu_a \approx 0.2$ cm^{-1} and $\mu_s' \approx 12$ cm^{-1}. To obtain these optical coefficients for silicone rubber, 1.3 mg of white pigment and 0.13 mg of black pigment must be added for every 0.5 ml of both parts A and B (i.e. 1 ml total). First the required amounts of white and black pigment were added to an amount of Part A. The mixture was stirred until homogeneity was reached. Part B was subsequently added in a 1:1 ratio of Part A. This was mixed fully and degassed. The mold

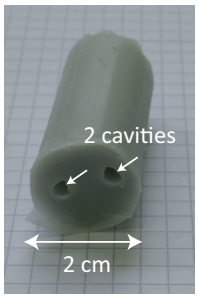

Figure 7.1: Silicon phantom of 2 cm diameter with two cylindrical cavities of 3 mm diameter.

consisted of a cylindrical syringe of 2 cm diameter. Cavities were created by fixating two cylindrical tubes of 3 mm diameter inside the syringe. We prepared a phantom with two off-center cavities (Figure 7.1). A phantom with one center cavity would not be useful for quantification experiments, because model errors often lead to artifacts that accumulate in the center and would in that case not be distinguishable from real signal. The mixture was poured into the mold and after 4 days the phantom reached its final solid state. The cavities were filled with liquid mixtures of 20 % Intralipid, 50 ppm India Ink and distilled water, and optionally a certain concentration of fluorochrome [Niedre et al., 2006]. The reduced scattering coefficient was assumed to scale linearly with the amount of Intralipid added [Flock et al., 1992], and the absorption coefficient linearly with the amount of India ink added. The cavities were closed using clay sealant (Critoseal).

7.3 Phantom experiments and ex-vivo experiments

We used the silicon phantom described above and a regular Black 6 mouse (Jackson Laboratory) for calibration of two fluorescent probes: IntegriSense 680 (Perkin Elmer), used for the investigation of lung cancer (Section 8.3) and Annexin Vivo 750 (Perkin Elmer), which was used for the study of myocardial infarction (Section 8.6).

The properties of the investigated probes are displayed in Table 7.1. Annexin Vivo was supplied as a liquid in 1 ml vials. There is one fluor to each molecule, resulting in a concentration of 1 mg/ml, and a starting concentration of 2.8 nmol/μl. IntegriSense was supplied as a powder. The standard dilution was 2 nmol /100μl in 1 x PBS (Phosphate Buffered Saline).

Table 7.1: Properties of Annexin Vivo 750 and IntegriSense 680.

Probe	Molar Weight	Excitation	Emission	Starting Concentration
Annexin Vivo 750	35,000 g/mol	755 nm	772 nm	2.8 nmol/100 ml
IntegriSense 680	1432 g/mol	675 nm	693 nm	2 nmol/100 ml

Table 7.2: Prepared mixtures for experiments [μl].

	Mix 1	Mix 2	Mix 3
Probe	12.5	25	0
Intralipid	5	5	5
Ink	0.5	0.5	0.5
Water	82.5	70	95
Total	100.5	100.5	100.5

For both probes we made similar mixtures of probe, Intralipid 20 %, India Ink and distilled water using the quantities displayed in Table 7.2. We assumed that the optical properties of the probe mixtures were close to the optical properties of the silicon phantom. The resulting concentrations of

Table 7.3: Concentrations $c1$ and $c2$ of probes in Mix 1 and Mix 2 (see Table 7.2). Mix 3 does not contain fluorescent probe.

	c1 (Mix 1)	c2 (Mix 2)	Mix 3
Annexin Vivo 750	35 nM	70 nM	0
IntegriSense 680	25 nM	50 nM	0

probe in the two mixtures for each of the probes are displayed in Table 7.3. Mix 1 had a concentration $c1$ of fluorochrome and Mix 2 a concentration $c2$, with $c2 = 2 \times c1$.

For the phantom experiments, we filled translucent tubes with the probe mixtures and placed them in the cavities of the phantom in three different configurations for both probes. We used these additional tubes instead of pouring the mixture directly into the cavity to mimic the experimental conditions of the ex-vivo mouse experiment that is described below, where a similar translucent tube is inserted in the aesophagus of a mouse. The three phantom experiment configurations were: 1) a tube with Mix 1 in one cavity, 2) a tube with Mix 2 in one cavity and 3) a tube with Mix 1 in one cavity and a tube with Mix 2 in the other cavity. The space left in the cavities was filled up with Mix 3 in all experiments, and the cavities were closed with clay sealant.

For the ex-vivo quantification experiments, we imaged a euthanized regular Black 6 mouse two times with the hybrid FMT-XCT system. Before the first measurement we inserted a tube with Mix 1 in the aesophagus of the mouse. After the mouse was imaged using the hybrid FMT-XCT system, the tube was replaced by a tube with Mix 2. In this way we could compare the quantification difference of the two mixtures without changing experimental variables related to the mouse. Mouse preparation was done by Moritz Wildgruber and Katja Kosanke from Klinikum Rechts der Isar.

Before reconstruction of the phantoms, we manually segmented both tubes based on the X-ray CT volume. For the reconstructions of the mouse measurements, we performed a regular thorax segmentation of bones, lung, heart and mixed tissue (Section 4.2.1), and additionally segmented the tube in the aesophagus as a separate region. We performed two reconstructions for all

cases, using 1) Standard Tikhonov regularization, in which we used the optical properties in the forward model, and the Identity matrix for the inversion and 2) Weighted segments regularization, in which we used a structured diagonal matrix with 1 for the tube and 4 for the remaining segments for the inversion instead of the Identity matrix (Section 4.2). For each of the obtained reconstructions we calculated the maximum reconstructed value in the tube segment.

Figure 7.2 shows the ratio $c2/c1$ of maximum values calculated for similar experiments. We calculated error estimates E over all six performed experiments using:

$$E = \sqrt{\frac{1}{N-1}\sum_{\exp=1}^{6}\left(\frac{c_2}{c_1} - 2\right)^2}. \tag{7.3.1}$$

The calculated errors are displayed in Table 7.4. Errors calculated based on the Standard Tikhonov reconstructions were larger than errors calculated based on the weighted segments reconstructions. These results confirm that the inclusion of prior information in the reconstruction results in more accurate quantification.

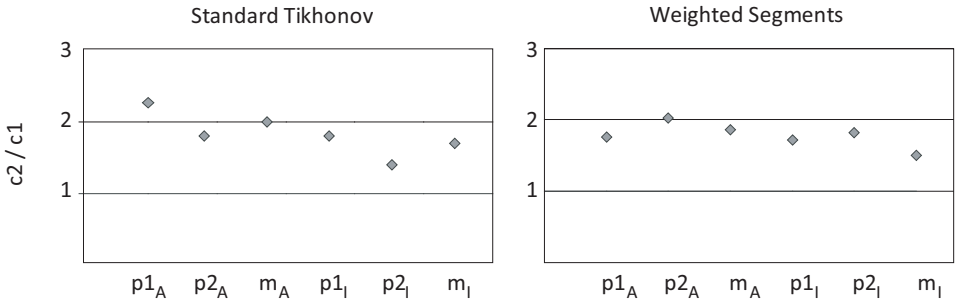

Figure 7.2: Quantification results of phantom experiments and ex-vivo experiments. Ratio c2/c1 for similar experiments, calculated based on p1: two phantom experiments with single fluorescent tube, p2: one phantom experiment with two fluorescent tubes, m: two mouse experiments. Subscript A=Annexin Vivo 750, I=IntergriSense 680.

7.4 In-vivo quantification experiment

We studied the in-vivo quantification capabilities of FMT-XCT based on a xenograft breast cancer mouse model, described in more detail in Sec-

Table 7.4: Error estimates, averaged over phantom and ex-vivo quantification experiments.

	Standard Tikhonov	Weighted Segments
Error	0.35	0.30

tion 8.2. A nude mouse was injected with 4T1 tumor cells in the neck and breast area one week prior to imaging. 24 h prior to imaging, the mouse was injected with 3 mg/kg ICG (fluorescent dye, exc: 765 nm, em: 820 nm). In-vivo imaging with the hybrid FMT-XCT system was performed under isoflurane anesthesia. After the measurement, the mouse was euthanized by an intra-peritoneal Ketamin and Xylazine injection and frozen for cryoslicing validation (see Chapter 1). The weighted segments method was used for the FMT-XCT reconstruction. Next to the anatomical segments (lungs, bones, heart and surrounding tissue), two large segments were added with a spherical shape that comprised the tumor areas and their vicinity. Weights were set to 1 for the tumor areas and 4 for the remaining regions.

The imaging results are displayed in Figure 7.3. Figures 7.3a,d show normalized trans-illumination images, obtained by dividing the acquired emission image for a source by the acquired excitation image. Images are shown for a source position scanned at the 25° and 185° rotation angle of the gantry. Figures 7.3b,e show the results of the hybrid reconstruction of the inside fluorescence distribution overlaid on the corresponding X-ray CT slices, while Figures 7.3c,f show corresponding cryoslices for validation of the reconstruction results. The signal from the neck tumor is brighter than the signal from the breast tumor in both the trans-illumination images and the reconstruction of the inside fluorescence distribution. This is confirmed by the fluorescent signals observed in the cryoslices. This example shows that the hybrid FMT-XCT system combined with hybrid reconstruction methods provides accurate quantitative reconstructions of the 3d fluorescence distribution in-vivo.

7.5 Summary and Conclusions

In this chapter we showed the quantification properties of hybrid FMT-XCT based on phantom experiments, ex-vivo experiments and an in-vivo

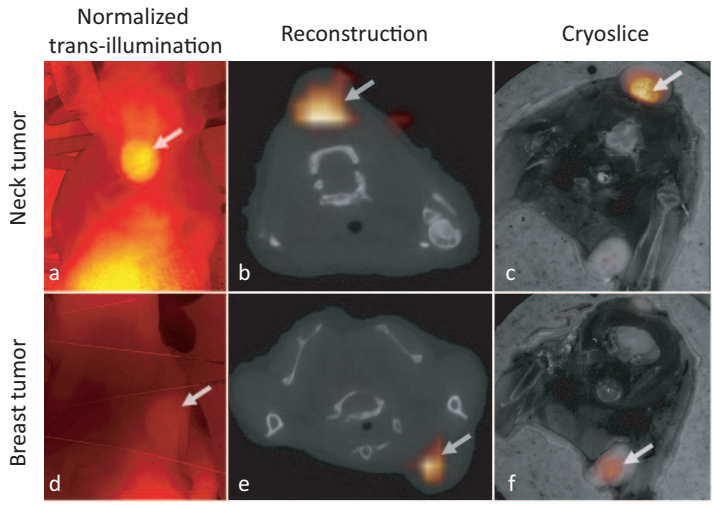

Figure 7.3: In-vivo quantification results. FMT-XCT imaging results for study of mouse with neck tumor (first row) and breast tumor (second row). a,d) Normalized trans-illumination images obtained with FMT modality. b,e) Hybrid FMT-XCT reconstruction of fluorescence distribution overlaid on corresponding X-ray CT slice. c,f) Validation cryoslices, planar fluorescence overlaid on RGB image reduced to greyscale. (Arrows indicate tumors.)

experiment. The phantom and ex-vivo results showed that quantification was improved when priors were added to the reconstruction. The in-vivo experiment demonstrated the ability to distinguish a difference in signal strength between two tumors in the same mouse. Additional quantification experiments can be found in Chapter 6, in which the effect of background fluorescence subtraction on quantification is investigated and Section 4.4, which shows results of a phantom experiment with two tubes of different size.

8

Applications

8.1 Introduction

In this chapter we show results of several animal studies performed with the hybrid FMT-XCT system and reconstructed with the hybrid FMT-XCT reconstruction method. The first group of experiments that is described is the study of a xenograft breast cancer model. The breast cancer model was imaged using several different fluorescent probes, and we show the ability of the hybrid FMT-XCT method and validation to increase the understanding of the mouse model. The second study describes a genetically modified mouse model of lung cancer. We analyzed the longitudinal development of lung tumor progression over time based on cryoslices, XCT data and hybrid FMT-XCT reconstructions. The last study of cancer that we describe is a study of a brain cancer model using fluorescent proteins. After that, we describe two more studies, a study of a mouse model of Osteogenesis Imperfecta, which was a challenging study because the mice were very fragile, and in the last section we describe a study of apoptosis after myocardial infarction.

The hybrid FMT-XCT method that was used for all animal studies is summarized below. The method consists mainly of data acquisition with the hybrid FMT-XCT system, calculation of the forward model and a step-wise inversion of the forward model, resulting in an estimate of the fluorescence distribution.

[1] In-vivo data acquisition

FMT and XCT data was acquired sequentially with the hybrid FMT-XCT system that was described in Chapter 1, using the parameters given in Chapter 3, Table 3.1, and placing the mouse in an optimal position, as was indicated in Figure 3.3. We acquired FMT-XCT white light images, emission images, excitation images and X-ray CT images for the full 360° range.

[2] Segmentation of the X-ray CT data
The X-ray CT images were reconstructed into a 3d volume using XCT software (GE Medical Systems). The 3d X-ray CT volume was segmented in anatomical regions, using methods described in Section 4.2.1. For the thorax these regions consisted of: bone, lung, heart, liver and mixed tissue. For the breast cancer study described in Section 8.2, additional segments were created to cover a tumor area. For the brain region, the segments were: brain, bone, jaw area and mixed tissue.

[3] Background fluorescence subtraction
An X-ray CT based background fluorescence subtraction was applied to reduce the effect of auto-fluorescence and residual targeted probe in the mouse (Chapter 6). The background fluorescence subtraction was applied in the K-ras study (Section 8.3).

[4] Selection of optical attenuation coefficients
The optical attenuation coefficients that were used during the calculation of the forward model are summarized in Chapter 5, Table 5.2 for the thorax region and Table 5.3 for the brain region.

[5] Calculation of the forward model
We calculated a Finite-Element-Method-based forward light propagation model, using the Diffusion Equation (Section 2.2), with the optical attenuation coefficients assigned to the nodes. The forward model calculation delivered Green's functions, out of which the weight matrix was formed.

[6] Input data selection
The normalized trans-illumination images (emission/excitation) served as the input for the reconstruction algorithm. Before the reconstruction, we removed input data that was related to regions with light propagation effects that are not included in the Diffusion Equation

(see Chapter 3). A data vector was formed based on the normalized images.

[7] First inversion
The node-based forward model was mapped to cubic voxels that were used for the inversion. We selected a voxel size based on the desired resolution and memory limits. We performed a first inversion, using Standard Tikhonov regularization with the Identity matrix as the regularization matrix. The LSQR algorithm was used for all inversions. The first inversion delivered a first estimate of the fluorescence distribution.

[8] Calculation of weights
Based on the reconstruction obtained with the first inversion, we calculated data-driven weights for each segment. The weights indicated the amount of reconstructed signal per segment, the smallest weight was assigned to the segment with the largest amount of signal and the largest weight to the segment with the least amount of signal reconstructed in the first inversion (Section 4.4).

[9] Second inversion
The weights were placed on the diagonal of a penalty matrix. Each diagonal element in the penalty matrix corresponds to one voxel in the reconstructed volume. Voxel weights were calculated based on the segment weights proportional to segment occupation. We calculated a second inversion using the diagonal penalty matrix. Using the prior information in both the forward model and the inversion resulted in an improved reconstruction result.

[10] Further inversions
Optionally, we repeated steps 7-9, we refined the weights in each cycle, this was done for the K-ras study (Section 8.3).

[11] Hybrid visualization
Finally, we used the X-ray CT data for hybrid visualization of the FMT-XCT reconstruction and anatomical information, using Amira (Visage Imaging).

We summarized the parameters used for the reconstruction in Table 8.1. The detector spacing is used for reduction of the acquired images. The voxel size is used during reconstruction. The values were selected from the

indicated range, based on the target size and size of the volume. The λ_{idx} for the first inversion indicates which regularization parameter was selected to obtain the reconstruction on which the calculation of weights was based, and the λ_{idx} for the second inversion indicates the regularization parameter that is used to obtain the final estimate of the fluorescence distribution that was used for visualization and quantification. The selected index depended on target size and noise level. The amount of LSQR iterations was set to 50 in all inversions.

Table 8.1: Reconstruction parameters.

Parameter	Setting
Detector spacing	0.8mm - 1mm
Voxel size	0.75mm^3- 1mm^3
λ_{idx} for first inversion	65 - 85
λ_{idx} for second inversion	45 - 65
N iterations	50

The method is summarized in the flowchart below. The chapter numbers indicate where to find detailed information on the different steps in the method.

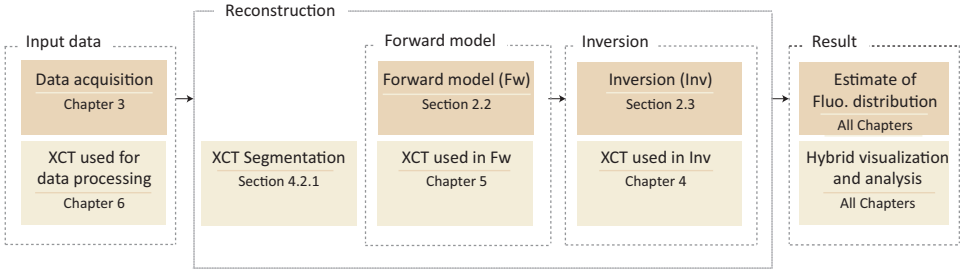

Figure 8.1: Overview of the hybrid FMT-XCT method. The X-ray CT data is used to improve all steps in the method.

An overview of the improvements obtained when using the hybrid FMT-XCT method is displayed in Figure 8.2. Transversal images from three different studies are shown, a breast cancer study (Section 8.2), bone formation study (Section 8.5) and lung cancer study (Section 8.3). The first column shows results of a reconstruction in which no prior information is

used, reconstructed using Standard Tikhonov regularization ($\mathbf{L} = \mathbf{I}$). The reconstructed fluorescence signal is overlaid on the corresponding X-ray CT slice. The second column shows the result of a reconstruction in which only the optical properties are used. This is the result of the first inversion, which is used to calculate segment weights. The third column shows results using a method that was developed for Diffuse Optical Tomography (DOT) reconstructions. In comparison this method gives results that are too smooth. Column 4 displays corresponding cryoslicing images. Planar fluorescence signal in orange is overlaid on a greyscale image of the slice. The last column displays the reconstruction obtained with the hybrid FMT-XCT reconstruction method. Compared to the reconstructions shown in the first three columns, the reconstruction result is considerably improved. These and other studies performed with the hybrid FMT-XCT method will be described in more detail below.

8.2 Analysis of the tumor microenvironment: 4T1 breast cancer model

In this first application study we describe a subcutaneous tumor model. Subcutaneous (beneath the skin) tumors are a relatively easy target for optical imaging, compared to targets deeper inside the animal. Therefore, these models are often used for evaluation of the performance of different fluorescent probes in combination with a certain disease model. In this section, we describe the analysis of a subcutaneous breast cancer model in combination with three probes with different biological targets, imaged using the hybrid FMT-XCT method and validated by cryoslicing. The animal studies that we show were investigated as part of different projects, which we combined here in order to compare different aspects of the tumor.

Breast cancer forms in the tissue of the breast. The number of new cases in the United States in 2010 was around 200.000. Since 1990, the survival rate of women diagnosed with breast cancer in the United States has been improving. This can be attributed to progress in screening and treatment. Current research is, among other aspects, aimed at early detection of breast cancer, advances of treatment and further identification of genes that are related to the disease. Examples of possible treatment advances are the development of less toxic treatments, personalized treatments, and treatments that use the immune system to enable the body itself to recognize and destroy cancer cells. (source: National Cancer Institute at the National

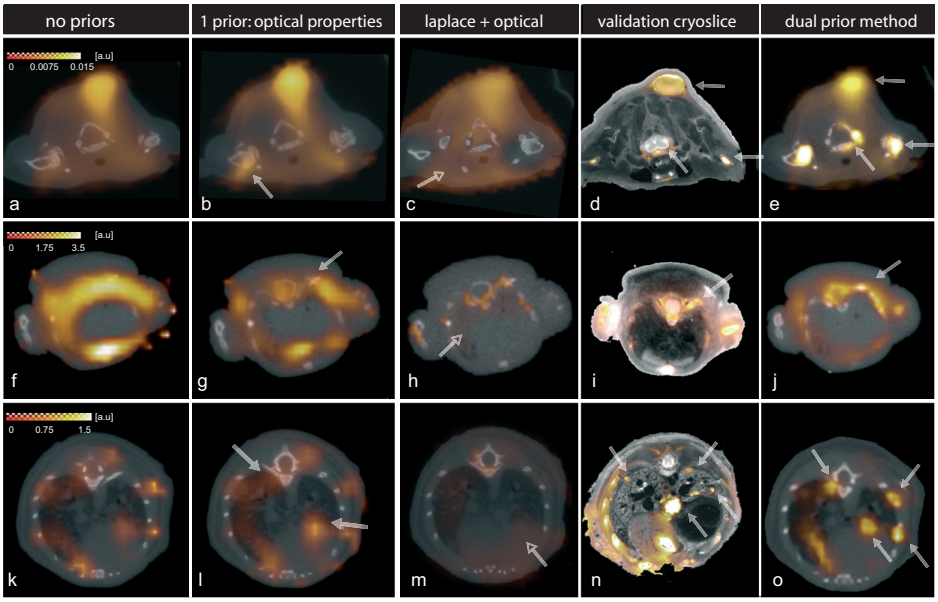

Figure 8.2: Comparison of FMT reconstruction using different reconstruction methods. Transversal slices of FMT reconstruction overlaid on corresponding XCT slices. a-e) Neck tumor study. f-j) Osteogenesis Imperfecta study. k-o) K-ras study. Column 1) Reconstruction without prior information. Column 2) Reconstruction with one prior, the optical properties, arrows indicate signals with improved quantification compared to the first column. Column 3) Reconstruction using Laplace regularization combined with the use of optical properties, arrows indicate areas that are smoothed towards an average value per segment. Column 4) Validation cryoslices, arrows indicate fluorescent signals that correspond to the signals indicated with the arrows in Column 5) Reconstruction with the hybrid FMT-XCT method.

Institutes of Health)

In this study we used the 4T1 breast cancer cell line (ATCC CRL-2539), injected subcutaneously in nude (BALB/C) mice. When 4T1 cells are injected subcutaneously in nude mice, the first stage is the development of a local subcutaneous tumor. In a later stage the tumors can become metastatic, and can spread to lung, liver, lymph nodes and brain. The development and spread of 4T1 tumor cells in mice is assumed to closely resemble the progress of human breast cancer. (source: ATCC)

The investigated subcutaneous tumors consisted not only of cancer cells. Tumors consist of a heterogeneous nutritional microenvironment that con-

tains for example blood vessels for the supply of oxygen and proteins that can cut through tissue in order to make space for growth [Siemann, 2011]. The tumor microenvironment plays an important role in the malignancy of the tumor, multiplication and metastasis [Joyce and Pollard, 2009; Hanahan and Weinberg, 2011; Whiteside, 2008]. Different aspects of the tumor microenvironment can be investigated using fluorescent probes with different biological targets. We investigated the distribution of 1) ProSense, 2) ICG and 3) an integrin targeting probe.
ProSense is a fluorescent probe activatable through cleavage by proteases. Proteases are often found in the tumor microenvironment, and are an important factor for the invasiveness and spread of the tumor. They can promote cancer cell invasion by cleavage of cell-cell junctions which facilitates cell migration [Joyce and Pollard, 2009].
ICG is an agent without a specific target, and gives information about vasculature. Tumors need blood vessels for the supply of nutrients and drain of waste products. Cancer cells can induce formation of blood vessels by sending out hypoxic- (lack of oxygen) and other signals. The vascular network formed by tumors connects at one or more sites to the existing vasculature, but is chaotic and contains unfinished and unconnected vessels [Heath and Bicknell, 2009]. Tumor vasculature plays an important role in the delivery of drugs to the tumor site [Ebos and Kerbel, 2011].
The last agent we imaged, is a hybrid modality probe that targeted integrin $\alpha_v\beta_3$. Integrins are molecules that are expressed on the cell surface, and are essential for cell migration and invasion because they are involved in the connection of cells to the extracellular matrix (tissue outside of cells that provides structure) and in the signalling for angiogenesis (formation of new blood vessels). There are many different integrins that can be upregulated or downregulated in tumors, integrin $\alpha_v\beta_3$ in particular is overexpressed in tumors [Hood and Cheresh, 2002].

8.2.1 Comparison of the distribution of fluorescent agents.

We compared the probe distribution in subcutaneous 4T1 tumors based on cryoslices. We investigated the first stage of tumor growth, the local subcutaneous tumor, in combination with the three fluorescent probes that were described above. Cells were implanted in the breast, neck or back area of the mouse approximately one week before imaging in all cases and fluorescent probes were injected 24 h before imaging.

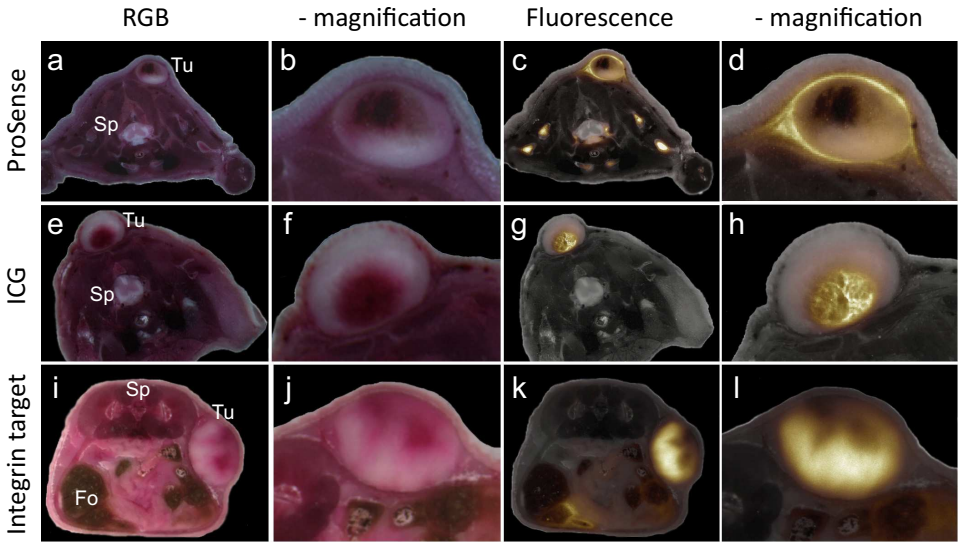

Figure 8.3: Overview of cryoslicing results obtained from nude mice with subcutaneous 4T1 tumors and three different fluorescent agents. Row 1) Slices from a mouse with a neck tumor and injected with ProSense 680. Row 2) Mouse with neck tumor and injected with ICG. Row 3) Mouse with back tumor injected with integrin targeting probe. Column 1) RGB cryoslicing image. Column 2) Magnification of RGB image. Column 3) Planar fluorescence cryoslicing image overlaid on RGB reduced to black and white. Column 4) Magnification of planar fluorescence image. (Tu=Tumor, Sp=Spine, Fo=Food.)

ProSense

The first probe that we imaged is ProSense 680 (exc: 680nm, em: 705nm, Perkin Elmer). ProSense is an activatable imaging agent that is activated by proteases such as Cathepsin B, L, S and Plasmin. Cathepsins are produced by cells, and after being expressed they can enter the blood stream. Before protease-mediated activation the probe is optically silent (it is not fluorescent) [Weissleder et al., 1999]. The results of ProSense imaging are shown in the first row of the cryoslicing overview (Figure 8.3). 4T1 cells were injected subcutaneously in the neck of the imaged nude mouse and ProSense was injected 24 hours before imaging. The RGB image (Figure 8.3a) shows a slice of the neck area of the mouse, with the subcutaneous tumor (indicated by Tu) at the top of the cryoslice and the spine (indicated by Sp) in the middle of the cryoslice. In the magnification of the tumor area (Figure 8.3b), we observe that the tumor consisted of a white area, assumed to be the tumor cell mass, and a red area, which we assumed to be a core with chaotic vasculature and necrosis. Larger vessels appeared to be sur-

rounding the tumor cell mass. The planar fluorescence image (Figure 8.3c) shows the fluorescent signal in orange, overlaid on the RGB image reduced to black and white. Based on the image of the complete slice, we observed that ProSense was accumulating in general in the tumor area and in the bone areas. In the magnification of the tumor area (Fig. 8.3d) we found that ProSense was spread throughout the tumor mass, with the highest concentrations in the surrounding vasculature, and the lowest concentrations in the core of the tumor. Because ProSense is a protease activatable probe, we inferred that proteases were overexpressed by the cells in the tumor mass compared to the surrounding tissue, after which they were possibly released into the blood stream where they distributed throughout the surrounding vasculature.

ICG

The second probe that we examined was ICG (IndoCyanineGreen). ICG is a fluorescent dye; it does not have a specific target but circulates through the bloodstream until it is secreted. The emission strength of ICG increases with concentration until reaching a certain maximum level, after which emission strength decreases with increasing ICG concentration. The excitation maximum of ICG (around 800 nm) does not exactly match the 750 nm filter settings of the cryoslicing system, but results were still satisfying. We imaged ICG at 24 hours after probe injection. The cryoslicing results are shown in the second row of Figure 8.3. 4T1 cells were injected in the nude mouse at two sites, the neck area and the breast area. In this figure we show the results for the tumor in the neck area. In the RGB image of the cryoslice (Figure 8.3e) we observed a tumor appearance similar to the tumor in Figure 8.3a. The tumor consisted of a white cell mass with a dark core, surrounded by vasculature. In the magnification of the tumor area (Figure 8.3f) we observed that the dark core was closest to the lower boundary of the tumor area vasculature, and that the red area gradually turned into white without showing a sharp border. In the planar fluorescence image of the cryoslice (Figure 8.3g), ICG appeared to be concentrated mainly in the core of the tumor. No apparent background signal in the rest of the tissue was observed. Based on the very low level of background fluorescence observed in the fluorescence image, we concluded that after 24 hours, ICG was washed out of the bloodstream, and showed only a retention effect. The dye stayed behind in the core of the tumor, while the rest of the tumor area and surrounding tissue was cleared. Because ICG travels through the blood

stream, the explanation for the observed probe distribution could be that ICG leaked into the tumor core through incomplete vasculature [Heath and Bicknell, 2009] and because the vasculature was probably chaotic and not connected at the end points, blood with fluorescent dye could flow into the core, but not exit the area. This idea was strengthened by the structures seen in the magnification of the fluorescence image (Figure 8.3h). The vasculature appeared to be denser close to the border of the tumor area, where the core vasculature could be connected to the surrounding vasculature. With the gradually decreasing redness of the core area, the strength of the ICG signal decreased as well, indicating decreasing amount of vasculature from core towards cell mass.

Integrin targeting probe

The last probe that we investigated was a probe targeting $\alpha_v\beta_3$ integrin. The probe, termed RGD-MSAP, was a combination of an RGD peptide, a radiolabel and a cyanine dye. A nude mouse with a subcutaneous 4T1 tumor grown at the back of the mouse was imaged in-vivo with SPECT-CT at a different institute, after which it was euthanized. After decay of the radioactivity, the mouse was shipped to our institute where we imaged it with our systems. The cryoslicing results are shown in the third row of Figure 8.3. In the RGB cryoslice of the back of the mouse (Figure 8.3i), the tumor is located at the right side of the mouse (indicated by Tu). It was relatively large compared to the tumors studied in combination with the first two probes, but it showed a similar combination of white cell mass and red core. In the magnification of the tumor (Figure 8.3j) we observed two core areas, of which one was more clearly connected to the surrounding vasculature. The color images have slightly different contrast compared to the previous two data sets, because of a change of camera for the cryoslicing system. The green areas in the RGB slice indicate food in the digestive system. In the planar fluorescence image (Figure 8.3k), we observed that the fluorescence signal was coming mainly from the white cell mass. A much lower level of fluorescence was observed in the cores of the tumor, and no significant signal was observed in the surrounding vasculature. By comparing the RGB magnification (Figure 8.3j) with the magnification of the planar fluorescence image (Figure 8.3l) we could correlate areas of increased fluorescence signal with areas that are relatively white in the RGB image, which indicates that the tumor cell mass is overexpressing $\alpha_v\beta_3$ integrin. A fluorescent probe that could be used to obtain similar results is IntegriSense

(Perkin Elmer), suited for cases when only optical contrast is of interest.

8.2.2 In-vivo imaging with FMT-XCT

The mice described above were imaged with FMT-XCT prior to cryoslicing. The mice injected with ProSense and ICG were imaged in-vivo with FMT-XCT under isoflurane anesthesia, after which they were euthanized by an intra-peritoneal Ketamin and Xylazine injection and frozen for the validation experiments. The mouse injected with the integrin targeting probe was imaged ex-vivo. The hybrid FMT-XCT method was used for the reconstructions, see Section 8.1 for a summary of the method. FMT-XCT imaging and validation results of the mouse injected with ProSense are displayed in Figure 8.4, showing FMT-XCT reconstructions, visualized with Amira (Visage Imaging). Good congruence between the fluorescence reconstruction and the anatomical position of the tumor is observed in Figure 8.4a. The tumor position is indicated with an arrow on the isosurface plot of the skin shown in Figure 8.4b. Figures 8.4c,d show magnified images from the reconstructed tumor area, which allow for a more detailed observation of the reconstruction. Figures 8.4e-h show data that cross-validate the FMT-XCT reconstruction. Figure 8.4e shows an FMT-XCT slice through the tumor area. The FMT signals shown in color are superimposed onto the corresponding XCT image shown in greyscale. Figure 8.4f depicts a hybrid image obtained post-mortem, after the mouse was frozen and cryosliced. In particular the fluorescence intensity observed post-mortem from the cryoslice under an epi-illumination camera is superimposed in color on a mouse photograph shown in greyscale. Figures 8.4e and 8.4f are obtained from approximately the same area of the mouse and show congruent signals; fluorescence signal is seen in the tumor area and around the spine on both images, whereas two more foci of fluorescence activity in the lower left and right parts of the slice shown are also observed on both images. Generally, the cryoslice image is obtained with higher resolution than the non-invasive FMT-XCT image. Figures 8.4g-h show correlative H&E staining of the tumor region, imaged using a microscope. After H&E staining of the slice, the cell nuclei turn purple. The dense purple cell mass represents the tumor area, populated with cancer cells. Signal localization was compared between the FMT-XCT slice, cryoslice and FMT slice reconstructed without priors (see also Figure 8.2), by calculating the area in each anatomical region that was covered by signal that was larger than half of the maximum signal in the complete slice, divided by the total area of the anatomical region (Figures

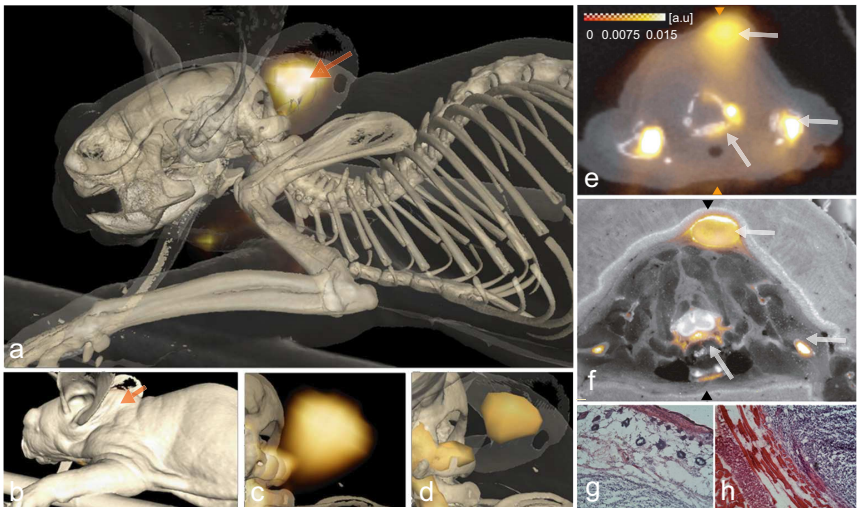

i

Signal strength	Maximum Tu/Ti	Tu/Bo	Bo/Ti	Average Tu/Ti	Tu/Bo	Bo/Ti
FMT-XCT	1.8	0.45	3.8	3.4	1.2	2.8
Cryoslice	1.5	0.88	1.6	3.5	1.9	1.8
No priors	0.85	3.9	0.22	3.2	5.5	0.59

j

Localization	Area [signal>max/2]/ Total area Tumor	Bone	Tissue
FMT-XCT	89%	43%	35%
Cryoslice	100%	75%	27%
No priors	90%	2%	34%

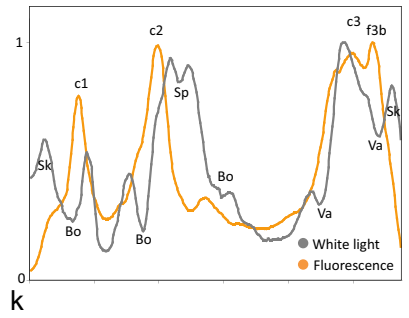

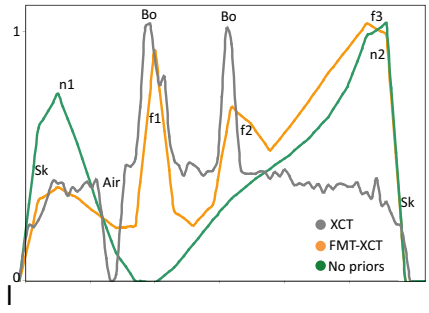

Figure 8.4: Imaging results of ProSense study. a) Thresholded 3d renderings of bones and skin based on XCT data and fluorescence signal based on FMT reconstruction. b) Isosurface of skin. c) Magnification of Figure a without skin. d) Magnification with isosurface for FMT reconstruction. e) Transversal slice of FMT reconstruction overlaid on corresponding XCT slice. f) Cryoslice of the same area. g−h) H&E staining of the tumor region. i−j) Relative signal strength and signal localization in displayed FMT-XCT slice compared to cryoslice. k) Profiles over cryoslice indicated with black triangles in Figure f, c1−c3=fluorescence peaks in cryoslice, Sk=Skin, Bo=Bone, Sp=Spine, Va=Vasculature. l) Profiles over FMT-XCT reconstruction indicated with orange triangles in Figure e, f1−f3=fluorescence peaks in FMT-XCT reconstruction, n1−n2=fluorescence peaks in reconstruction without priors, Sk=Skin, Bo=Bone. (a.u, arbitrary units.)

8.4i-j). This indicates which percentage of the anatomical region was covered by signals of relatively high intensity compared to the rest of the slice. We observed improved correspondence for the bone area between cryoslice and FMT-XCT reconstruction when prior information was used, while the correspondence for other regions remained the same. For more detailed comparison of cryoslice and reconstruction we plotted profiles over a line for the cryoslice (Figure 8.4k, position indicated by black triangles in Figure 8.4f), and reconstruction (Figure 8.4l, position indicated by orange triangles in Figure 8.4e). Anatomical features are plotted in both graphs to facilitate comparison of localization (grey lines). The same improvement for the bone areas is observed in the profiles; fluorescence peaks in the bone area are observed in the cryoslice (c1 and c2) and in the FMT-XCT reconstruction (f1 and f2), but not in the FMT reconstruction without priors (green line in Figure 8.4l).

The hybrid FMT-XCT reconstruction of the mouse injected with ICG is displayed in Figure 8.5. The reconstruction was already described in Chapter 7. This mouse had two tumor sites, the neck and breast. Next to the anatomical segments (lungs, bones, heart and surrounding tissue), two large segments were added with a spherical shape that comprised a large region that included also each tumor area. As was described in Chapter 7, there is a quantitative difference between the fluorescence signal in the two tumor areas. Figure 8.5a shows a 3d rendering of the skin of the mouse viewed from the front, the tumors are indicated by arrows. In the thresholded 3d rendering of the FMT-XCT reconstruction (Figure 8.5b) the fluorescence signal is visualized by an orange isosurface rendering. Both tumors are visible. Figure 8.5c shows a 3d rendering of the skin viewed from the back of the mouse, now more clearly displaying the tumor in the neck of the mouse. Figure 8.5d is a thresholded 3d rendering of the FMT-XCT reconstruction using the same threshold as in Figure 8.5b, while the threshold in Figure 8.5e is set to double the value of the threshold in Figure 8.5d, illustrating the quantitative difference between fluorescent signal strength at the two tumor sites.

The hybrid FMT-XCT reconstruction of the mouse injected with the dual modality probe is displayed in Figure 8.6. The bones were segmented using the automatic segmentation framework. The X-ray CT volume did not show significant other differences in contrast in the area of interest that

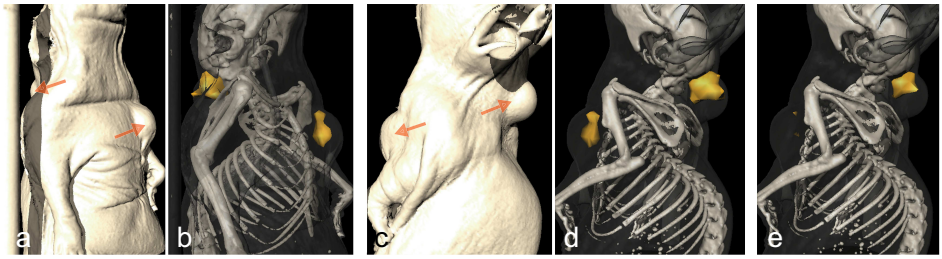

Figure 8.5: Hybrid FMT-XCT reconstruction of ICG. a) 3d rendering of skin. b) Thresholded 3d rendering of FMT-XCT reconstruction. c) 3d rendering of skin viewed from the back of the mouse. d) Thresholded 3d rendering of FMT-XCT reconstruction. e) Thresholded 3d rendering of FMT-XCT reconstruction with threshold set to double the value of the threshold in Figure d.

could be segmented using thresholding. With use of a contrast agent this could be improved in further studies. We manually added next to the bone segment a large spherical region surrounding the tumor area. We had limited information about the optical properties in this area, and therefore assigned only the optical properties determined for the bone area, and background optical properties to the rest of the tissue. The first image shows a rendering of the skin of the mouse. The tumor, indicated with an arrow, was located at the back of the mouse. The tail of the mouse is visible at the bottom of the image and the rods of the animal bed are observed at both sides of the mouse. In the hybrid rendering of FMT reconstruction and XCT volume (Figure 8.6b), the tumor was visualized using an isosurface in orange, bone structure in white, and the skin is displayed in transparent grey. The fluorescence level of the tumor area was well above the background fluorescence level.

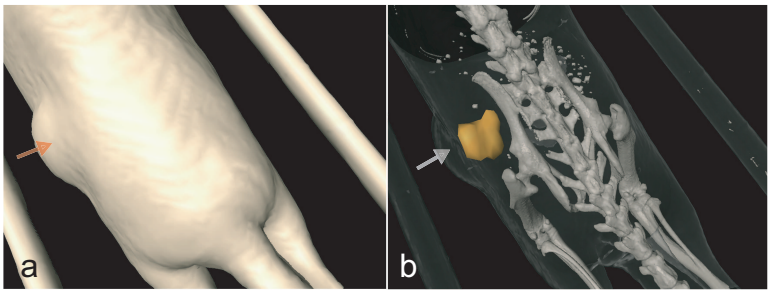

Figure 8.6: Hybrid FMT-XCT reconstruction of integrin targeting probe. a) 3d rendering of skin. b) Thresholded 3d rendering of FMT-XCT reconstruction.

8.2.3 Summary and Conclusions

In this study, we analyzed the differences in probe distribution in tumors ex-vivo based on high resolution cryoslicing images, and we visualized the accumulation of fluorescence agents in-vivo with hybrid FMT-XCT. Although the resolution of FMT-XCT was too low in order to see exactly where the probe accumulated in the way we could with ex-vivo planar fluorescence imaging, we could nevertheless assess the presence of the fluorescent agent, and in combination with the knowledge of the target of the probe and the information obtained from cryoslicing analysis, we could obtain in-vivo information about the presence and upregulation of proteases, integrins and vasculature.

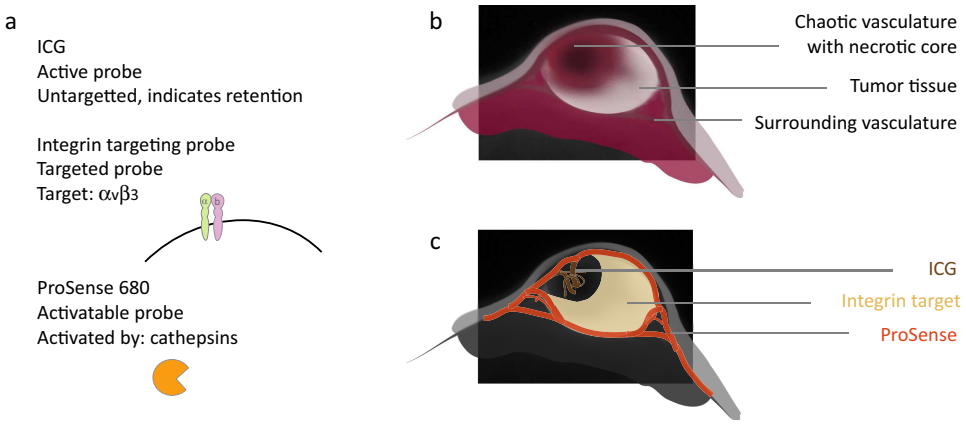

Figure 8.7: Summary of observations. a) Properties of the three investigated probes: ICG, integrin targeting probe and ProSense. b) Schematic of the main observed features of the tumor environment. c) Schematic of the different probe distributions.

We summarized the different structures of probe accumulation that were observed in the cryoslices of the three mice described above schematically in Figure 8.7. The tumor environment (Figure 8.7b) consisted in all cases of a white cell mass with a red core and surrounded by vasculature. We found that ICG, indicating retention of blood at 24 hours after injection, could be indicative of the incomplete vasculature in the core, the probe targeting $\alpha_v\beta_3$ integrin was highly expressed in the dense tumor cell mass and finally, ProSense imaging results indicated that proteases could be found in the cell mass as well, but the highest concentration of proteases was observed in the surrounding vasculature. A quantitative analysis of the

reconstruction results of the mouse injected with ProSense showed that the reconstruction of the fluorescence signal is considerably improved when using the hybrid FMT-XCT reconstruction method, compared to reconstruction without prior information.

8.3 Study of lung cancer progression: K-ras

In the second study we focussed on the early in-vivo detection of lung cancer and in-vivo monitoring of lung cancer progression over time starting from the earliest detectable stage. Lung cancer, one of the major causes of death by cancer in the world, is the uncontrolled growth of cells in the lung tissue. Lung tissue (see Figure 8.8) consists of a system of bronchi and bronchioles, with at the end of the bronchioles air spaces called alveoli that are covered by blood filled capillaries, through which the exchange of oxygen and carbon dioxide takes place. There are two main types of lung cancer: small cell lung cancer (SCLC) and non-small cell lung cancer (NSCLC). NSCLC is the most common type of lung cancer [Molina et al., 2008], and is highly correlated with smoking. Currently 70% of the patients

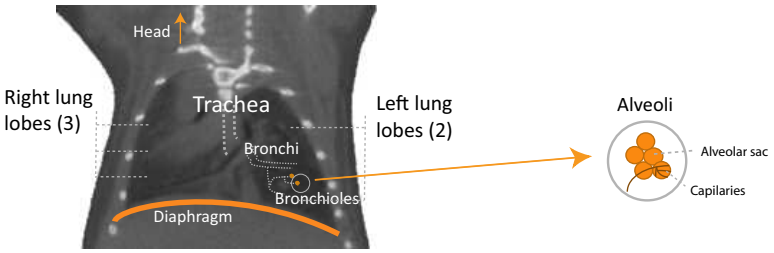

Figure 8.8: Coronal X-ray CT image of the lung area of a mouse. The main structures are indicated.

that are diagnosed with NSCLC are in a locally advanced or metastatic disease stage, treatment would benefit from earlier detection. This makes it particularly important to improve our understanding of the early stages of development of lung cancer. The detection of lung tumors with fluorescence tomography after 8 weeks of progression has been reported in [Grimm et al., 2005]. In this study we imaged NSCLC tumor development at earlier stages.

We used the K-ras mouse model for this study, a genetically modified mouse model that was created through activation of mutations in the K-ras oncogene (gene that has the potential to cause cancer). White K-ras mice (Jack-

son Laboratory) were crossed with Black 6 mice (Jackson Laboratory), resulting in mixed black and white offspring (bread by Vladimir Ermolayev at our institute), of which some were not expressing the K-ras mutation and some were expressing the mutation and developing spontaneous NSCLC lung cancer. In Figure 8.9 we compare the genetically modified K-ras with a xenograft (implantation of foreign cells) mouse model of lung cancer, LLC (Lewis Lung Carcinoma). To obtain this mouse model, LLC tumor cells were injected into the lungs of a Black 6 mouse, by first opening the mouse from the front in order to make the lungs visible, and subsequently injecting tumor cells into the lungs from the side (prepared by Katja Kosanke and Moritz Wildgruber from Klinikum Rechts der Isar). The LLC tumor model showed a quite aggressive development with many metastases. From the comparison of RGB cryoslicing images (Figure 8.9), we saw that the K-ras model developed tumors that were more integrated with lung tissue (indicated with arrows), while the LLC xenograft formed localized white cell masses. In general, xenograft mouse models are easier to produce and are therefore often studied [Deliolanis et al., 2006; Koenig et al., 2008], while genetically modified mouse models better mimic natural disease progression.

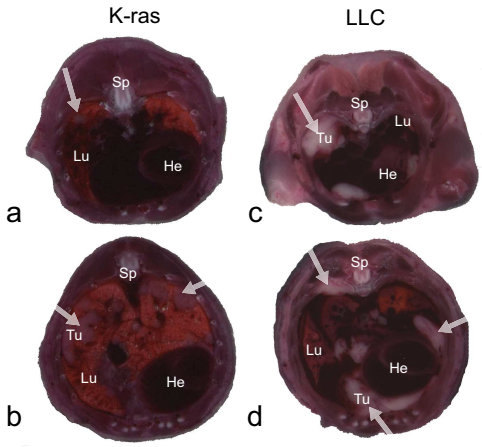

Figure 8.9: Comparison of K-ras and LLC lung cancer mouse model. a) RGB cryoslices of K-ras tumor model. b) RGB slices of LLC tumor model. (Lu=Lungs, He=Heart, Tu=Tumor, Sp=Spine, arrows indicate tumor sites.)

8.3.1 Imaging target and experimental procedure

The target that we selected for imaging tumor development was integrin $\alpha_v\beta_3$, which is overexpressed in tumors that are in the process of growth and metastasis [Hood and Cheresh, 2002]. 24h prior to imaging, the mice were injected with 2 nmol of an $\alpha_v\beta_3$ targeting fluorescent probe (IntegriSense 680, exc: 680 nm, em: 710 nm, Perkin Elmer). In-vivo FMT-XCT imaging was performed under isoflurane anesthesia, after which most of the mice were euthanized and frozen for cryoslicing validation and two mice were kept alive for further longitudinal experiments. Table 8.2 gives an overview of the number of scanned animals that are included in the analysis. All FMT-XCT data sets were acquired and reconstructed using the methods described in Section 8.1. Segment weights were calculated in the same way for all reconstructions, based on a sum of the values per region, and excluding the top and bottom slice of the reconstruction. The segment weights were automatically refined until the total change in segment weights was less than 1 %. An automatic background subtraction was applied before reconstruction, see Chapter 6.

Table 8.2: K-ras experiment overview. The number of mice that was imaged for each age group is indicated. 2 mice were imaged at multiple timepoints.

Kras	FMT-XCT	Cryoslicing
4w	2	3
adult	3	3
4w+7w	1	1
4w+9w	1	1

8.3.2 Tumor detection in adult K-ras mice

We established the imaging procedure for the K-ras mouse model based on the late stage of development (adult: 16-20 weeks old). In this stage of the disease, the tumor nodules have a size that is well within the detection limits of FMT-XCT (>1 mm). A full set of cryoslicing data for an adult K-ras mouse is displayed in Appendix A.1 for reference. FMT-XCT imaging results of an adult K-ras mouse are displayed in Figure 8.10. Figures 8.10a-b depict imaging and validation findings from three consecutive transversal

(axial) slices of the FMT-XCT reconstruction overlaid on the corresponding XCT slices (Figure 8.10a) revealing several fluorescence lesions in the mouse lung. Similar signals are observed in the corresponding cryoslices (Figure 8.10b) obtained from approximately the same region as the FMT-XCT images. Regions were approximate because placement of the lung of the mouse changed between the FMT-XCT measurement and the validation experiment due to the inherent difficulty of keeping the lung in the exact same position between in-vivo and ex-vivo experiments and the overall ability to accurately register virtual and actual sections. Figure 8.10c shows a 3d rendering of the FMT-XCT reconstruction together with the segmented bones and skin based on the XCT volume. Lung tissue is indicated in a semi-transparent green color, whereby fluorescence signal indicative of tumor is indicated in orange. In all slices arrows indicate lesions that show on both FMT-XCT reconstruction and corresponding cryoslices.

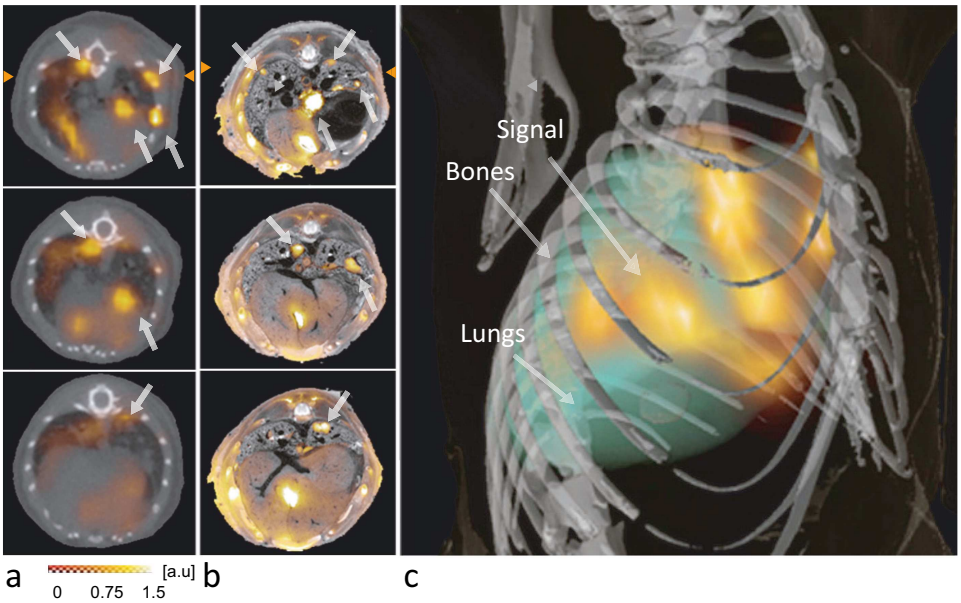

Figure 8.10: Hybrid 3d visualization of lung tumor study. a) Transversal slices of FMT reconstruction overlaid on corresponding XCT slices. b) Transversal cryoslices for validation of FMT reconstruction. c) Hybrid 3d rendering of FMT-XCT reconstruction. (a.u, arbitrary units.)

Comparison of Figures 8.10a and 8.10b shows that the reconstructed tumors are generally larger in area than the tumors seen in the cryoslice. The re-

sults of a quantitative analysis (Figure 8.11) show that the lung area covered with relatively intense signals was overestimated in the FMT-XCT reconstruction compared to the cryoslice. This could be explained by the fact that a single FMT-XCT slice contains more "background signals" compared to a cryoslice, since, due to diffusion, FMT-XCT samples a larger volume per slice compared to epi-illumination imaging. Regardless, comparison of profiles over a cryoslice and corresponding slice of the FMT-XCT reconstruction shown in Figure 8.12 shows an improved localization of signals when using priors. See for example signals c3 and f3 compared to the artifactual appearance of fluorescence peak n3 without using priors. These findings further confirm the in-vivo imaging ability of the FMT-XCT method and show superior performance compared to stand-alone FMT, while simultaneously displaying the limitation in resolution of in-vivo FMT-XCT imaging compared to ex-vivo planar fluorescence imaging of cryoslices.

	Area [signal>max/2]/ Total area			
Localization	Lungs	Bones	Heart+Liver	Tissue
FMT-XCT	45%	12%	18%	21%
Cryoslice	24%	68%	52%	65%
No priors	27%	0%	36%	17%

Figure 8.11: Quantification of lung tumor study. Ratio of area covered with signal compared to area not covered with signal.

8.3.3 Tumor progression over time

We analyzed the progression of NSCLC over time based on measurements of a group of K-ras mice of several ages, between 2 week old and adult mice. The fluorescence contrast of tumor/background observed in the 2 week old mice was not enough for FMT-XCT imaging. We analyzed the tumor development from 4 week old to adult mice based on cryoslices of the mice (Figure 8.13), focussing on features that are important for FMT-XCT reconstruction: target size and level of background fluorescence. In the adult K-ras mouse (Figure 8.13, last row), the tumor targets are around 2 mm, which is much larger than the maximum resolution that can be achieved with optical tomography. The target is also easily distinguished from the background fluorescence. In the young K-ras mouse of 4 weeks old, (Figure 8.13, first row), the targets are around 0.8 mm, which is close to the maximum resolution that is expected to be achievable. Not only are the targets relatively

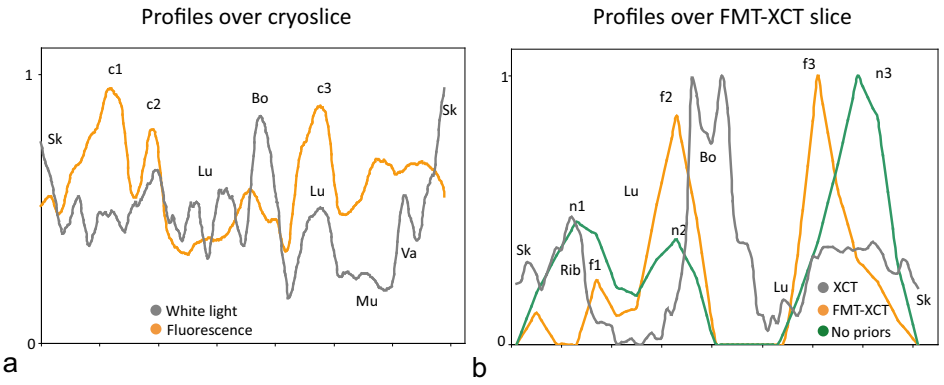

Figure 8.12: Quantification of lung tumor study. a) Profiles over cryoslice indicated with orange triangles in Figure 8.10b, c1-c3=fluorescence peaks in cryoslice, Sk=Skin, Lu=Lung, Bo=Bone, Va=Vasculature, Mu=Muscle. b) Profile over FMT-XCT reconstruction indicated with orange triangles in 8.10a, f1-f3=fluorescence peaks in FMT-XCT reconstruction, n1-n3=fluorescence peaks in reconstruction without priors, Sk=Skin, Bo=Bone, Lu=Lung. (a.u, arbitrary units).

small, the targets are not easily distinguished from the background fluorescence level either. A mouse with an age of 7 weeks (Figure 8.13, middle row), which is around the age that mice stop growing in length, shows an intermediate target size.

Using the knowledge obtained from the cryoslicing analyses, we investigated the detectability of tumors in-vivo with FMT-XCT. Figure 8.14 shows coronal slices of in-vivo measurements with X-ray CT acquired with the hybrid FMT-XCT system for 5 different mice. In the two week old K-ras mouse (Figure 8.14a), tumors are not distinguishable on X-ray CT. From age 4 week old and further (Figures 8.14b-e), we could observe small tumor nodules at the borders of the lung area. Magnifications of the lung border area are shown in the lower right corners. In case the tumors were located away from the borders of the lung, we could not distinguish them from normal lung tissue in the X-ray CT volume.

We further investigated the in-vivo progression over time based on the FMT-XCT reconstructions for the group of mice. Figure 8.15 shows the observed development of lung cancer in the measured K-ras mice. Both in-vivo and cryo-sliced measurements are shown as tumor to muscle ratio and showed an increasing trend from 4 weeks old towards adult mice (Figure 8.15a, average per group indicated by orange line). The ratios were calculated from

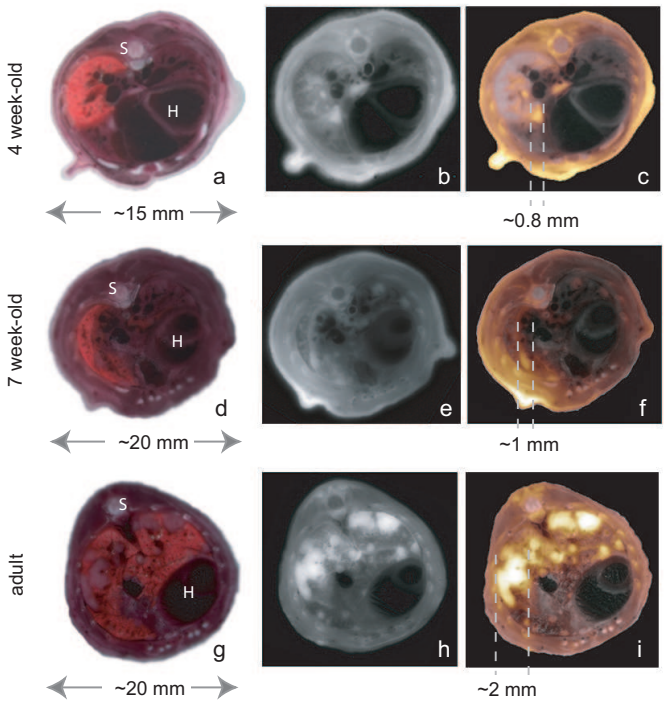

Figure 8.13: Cryoslice analysis of target size and background fluorescence for K-ras mice of different ages. Column 1) RGB color images. Column 2) Planar fluorescence images. Column 3) Composite of column 1 and 2. a-c) 4 week old K-ras. d-f) 7 week old K-ras. g-i) Adult K-ras. (H=Heart, S=Spine.)

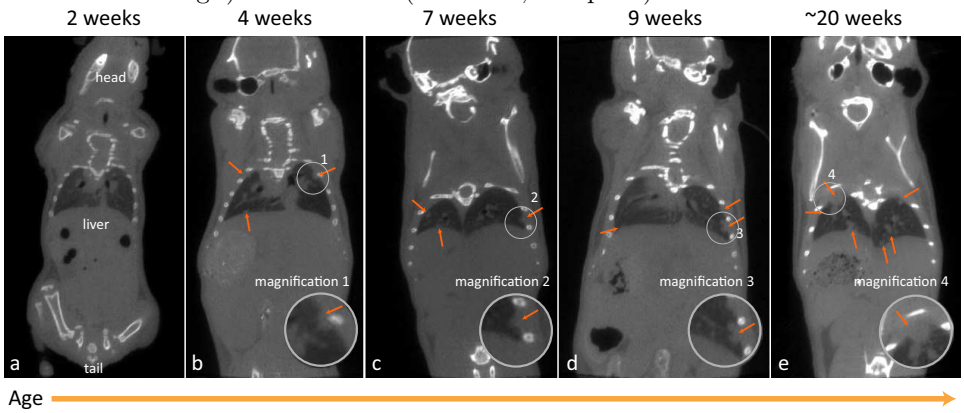

Figure 8.14: Coronal in-vivo X-ray CT slices of K-ras mice of different ages. a) 2 week old K-ras. b) 4 week old K-ras. c) 7 week old K-ras. d) 9 week old K-ras. e) Adult K-ras. Recognized tumors are indicated with orange arrows. Magnifications of the tumor areas are displayed in the lower right corner for age 4 weeks to adult.

the reconstructions in the following way: for the K-ras mice the maximum reconstructed value in the lung was divided by the averaged value for the surrounding tissue of all slices in the reconstructed volume, excluding top and bottom slice. For the controls (in absence of lesions) the average lung value was divided by the average reconstructed tissue value. For the calculation of the ratios based on the cryoslice data, we analyzed 2-4 slices per mouse. For the K-ras mice we calculated the maximum value of the lesions observed in the slice divided by the average value in the muscle area in the back of the mouse. The average ratio over all analyzed slices represents one data point per mouse. For the control mice, in absence of lesions, we calculated the average value of the lung area in the slice divided by the average value in the muscle area. Plotted in Figure 8.15 are the data points per mouse and a trend line. Cryoslicing data points are indicated by closed symbols, FMT-XCT data points are indicated by open symbols. The mice that were followed in-vivo during growth are indicated by dotted lines, and confirm the increase in observed signal. The FMT-XCT reconstruction of an adult mouse (Figure 8.15b) and corresponding cryoslice (Figure 8.15c) further illustrate the congruence between in-vivo and ex-vivo imaging.

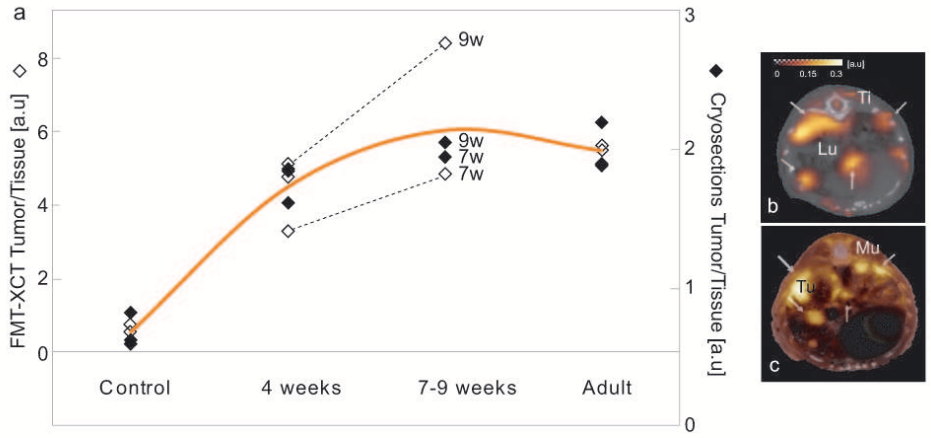

Figure 8.15: Lung tumor study as a function of mouse/tumor growth. a) Graph of ratio indicating tumor to tissue or muscle for K-ras, lung to tissue or muscle for control. Each data point corresponds to one value calculated for a mouse. The dotted lines connect points belonging to the same mouse. b) Transversal slice of FMT reconstruction for adult K-ras overlaid on corresponding XCT slice, Lu=Lung, Ti=Tissue. c) Validation cryoslice, Tu=Tumor, Mu=Muscle. (a.u, arbitrary units.)

8.3.4 Summary and Conclusions

In this section we displayed imaging results of a K-ras lung cancer model. We showed the detection ability based on an adult mouse and analyzed the disease progression based on in-vivo FMT-XCT results and validated by ex-vivo cryoslicing. This study showed the ability of FMT-XCT to image a complex mouse model and monitor changes in disease progression over time. A quantitative analysis of the reconstruction results similar to the analysis performed for the breast cancer study with ProSense showed that the reconstruction of the fluorescence signal is also in this case considerably improved when using the hybrid FMT-XCT reconstruction method, compared to reconstruction without prior information. Future imaging studies could be focussed on evaluating treatments, and monitoring the recovery process over time.

8.4 Imaging brain cancer using fluorescent proteins

Fluorescent proteins (FP) are an extremely versatile tool for the visualization of biological structures and events inside the cell. Any organism from single cells to whole animals can be genetically engineered to express a fluorescent protein. A cell can be engineered to express a fluorescent protein when it is transfected with a piece of DNA that encodes the protein. This class of fluorescent agents enables accurate and localized monitoring of disease progression [Shaner et al., 2005]. In this study we used fluorescent proteins to image brain cancer development. FMT combined with XCT has been used before to study the brain area of mice for the study of Amyloid-β plaques that are related to Alzheimers disease [Hyde et al., 2009a]. FMT combined with MRI has been used to study brain cancer development [McCann et al., 2009]. Deliolanis et al. [Deliolanis et al., 2011, 2009] previously imaged a brain cancer mouse model expressing the fluorescent protein mCherry with stand-alone FMT. In this study we have used a recently developed fluorescent protein called iRFP [Filonov et al., 2011] that has excitation/emission peaks in the near-infrared range (exc: 695 nm, em: 710 nm) and has increased brightness compared to red FPs. We demonstrate for the first time its use in FMT by imaging an iRFP expressing glioma brain tumor.

8.4.1 Experimental procedure

Two weeks before imaging, brain cancer cells (U87 cell line) expressing iRFP were stereotactilly injected in the brain of nude mice by Nikolaos Deliolanis. In-vivo FMT-XCT imaging at two consecutive timepoints was performed under isoflurane anesthesia, 2 weeks and 3 weeks after injection. The 680 nm laser and filter settings were used for illumination. A rectangular grid of 3 x 7 source positions with a spacing of 2 mm was scanned for each of the 18 selected projection angles (every 20 degrees). Illumination times were set to 0.1 s for the excitation measurement and 2 s for the emission measurement. After the measurement at the 3 week time point, the mice were euthanized and prepared for the cryoslicing validation experiments. The 3d X-ray CT volume was segmented into 4 anatomical regions: brain (area inside skull), bones, jaw area (area below skull, excluding bones) and mixed tissue (remaining area).

8.4.2 Imaging results

We first investigated tumor development based on the trans-illumination images obtained with the FMT-XCT system, and the validation cryoslices of the mice. Composite trans-illumination images were obtained by summation of all 21 normalized trans-illumination images for one projection angle ($-5°$), see Figure 8.16. The cryoslicing images were acquired at the 3 week timepoint. Tumor locations are indicated by arrows. The mice are ordered according to tumor depth. A localized bright signal was observed in all cases. The depth at which the tumor developed depends on the site of injection. We observed that all mice display an increased signal strength from the time point 2 weeks to 3 weeks after injection, but the increase is not equally strong for all mice. Tumors that were injected in the upper and middle brain area (m2-m4) show the largest increase in signal strength.
These observations are confirmed by the quantitative analysis of FMT-XCT reconstructions (Figure 8.17). FMT-XCT reconstructions for two time points for the three mice that showed the largest signal increase are shown. For display purposes, the reconstruction results are scaled to the maximum in each slice. The maximum reconstructed values in the tumor slice for each mouse and time point are displayed in Figure 8.17j (diamonds), together with the average over all mice (grey bars). A 3d rendering of mouse m3 is displayed in Figure 8.18, visualized with Amira (Visage Imaging). An isosurface of the fluorescent signal is indicated in green. The anatomical

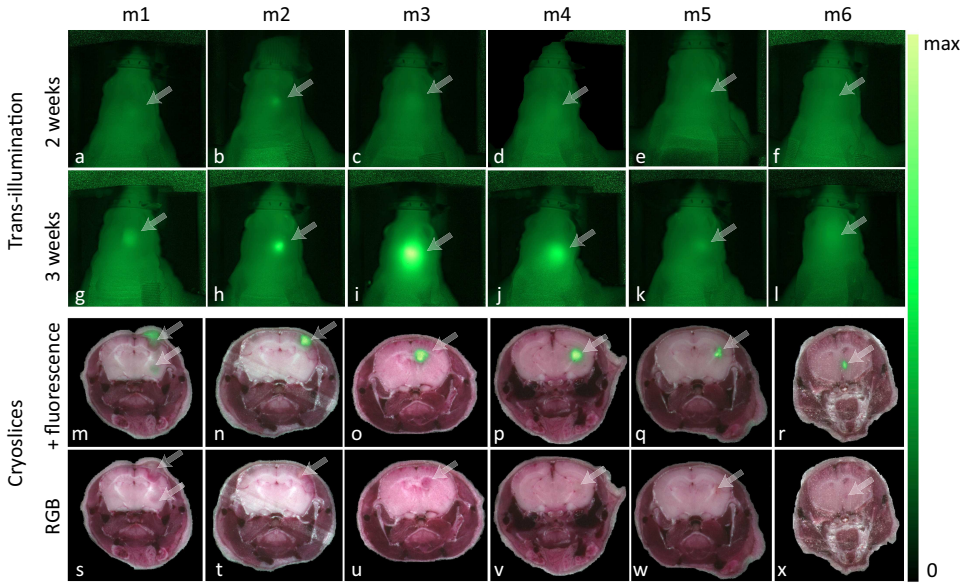

Figure 8.16: Trans-illumination images (a-l) and cryoslices (m-x) of brain cancer study for 6 mice (m1-m6). The tumor locations are indicated with arrows. Mice are ordered according to tumor depth.

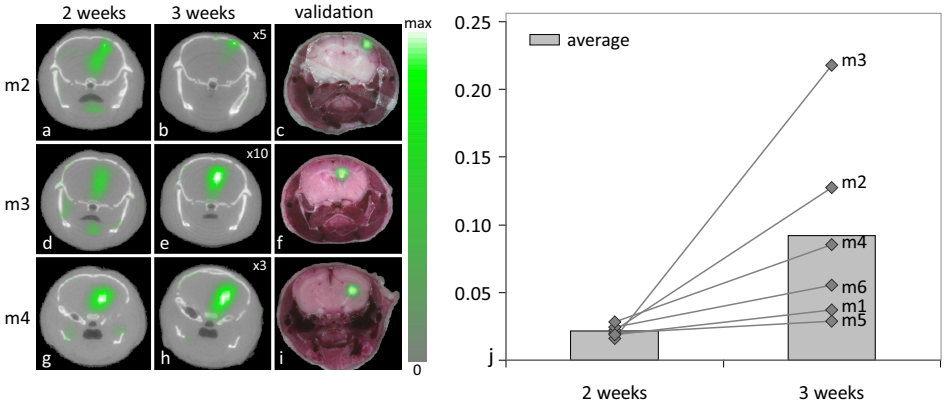

Figure 8.17: FMT-XCT results of brain cancer imaging. a-i) FMT-XCT imaging results at 2 weeks (a,d,g) and 3 weeks (b,e,h) after injection, and validation cryoslices (c,f,i) at 3 weeks after injection, for m2 (a-c), m3 (d-f) and m4 (g-i). j) Quantitative results of FMT-XCT reconstructions, corresponding to mouse m1-m6 in Figure 8.16. The maximum reconstructed value for each mouse in the tumor slice of the FMT-XCT reconstruction is plotted (diamonds), and the average over all mice for the 2 week and 3 week time point is displayed (bars).

structures are based on the X-ray CT volume. The needle-hole through

which the cells were injected in the brain is visible in the skull. The location of the reconstructed fluorescence signal corresponds well with the injection point.

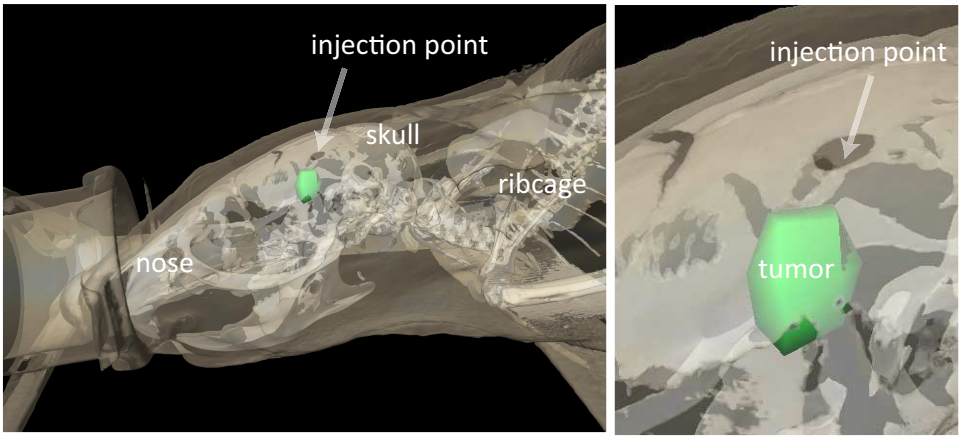

Figure 8.18: 3d FMT-XCT rendering of brain cancer imaging. a) 3d visualization of mouse m3, fluorescence signal from tumor indicated in green, anatomical structures are based on the XCT volume. b) Magnification of Figure a.

8.4.3 Summary and Conclusions.

In this study, we showed the imaging capabilities of FMT-XCT to resolve the fluorescent signal expressed by fluorescent proteins. The successful results of this study indicate a promising direction of disease research with great detail. Among many potential applications, FPs can serve as signal to monitor tumor size and location with FMT in various areas of the body and additionally monitor disease progress and therapy response. One of the applications that would be interesting for model development is the transfection of lung cancer cells with fluorescent proteins, in order to obtain a lung cancer model with very localized targets and a high signal to background ratio.

8.5 Imaging the bone structure of a mouse model of Osteogenesis Imperfecta

Osteogenesis imperfecta (OI) is an inheritable genetic disorder that is characterized by bones that break easily. The cause of the disease is an inad-

equate amount of bone collagen [Rauch and Glorieux, 2004], a protein in the connective tissue that works as a glue to connect cells to each other. When there is a lack of collagen, or the collagen is defect, the process of bone forming can not be performed well. There are several more and less severe forms of OI. Type I, the most common type, is the mildest form. It is characterized by, among other symptoms, easily fractured bones, near normal or slightly shorter stature and dental problems. Type II is the most severe form, often fatal in a very early stage, with severe bone deformity with many fractures, a very small stature and under-developed lungs. In between type I and type II are several moderate forms that are characterized by easily fractured bones and bone deformity, smaller statue, spinal curvature and possible respiratory problems. In this study we investigated a mouse model of Osteogenesis Imperfecta [Lisse et al., 2008] provided by Christian Cohrs and prof. Martin Hrabé de Angelis from the Institute of Genetic Engineering at the Helmholtz Centre Munich. The mouse model, called Aga2, has a genetic mutation that leads to changes in type I collagen. Some of the mice were found to survive longer than others [Thiele, 2009], and a division was made in a mild and a severe phenotype of the disease. In this study we investigated the mouse model with the hybrid FMT-XCT system at two ages, 6 and 9 days old (Figure 8.19). We show the diverse imaging capabilities of the hybrid FMT-XCT system for investigating the disease model.

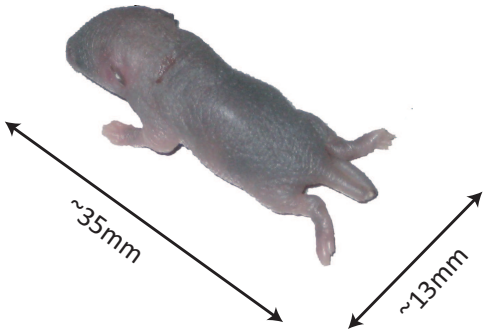

Figure 8.19: Picture of Aga2 baby mouse.

8.5.1 Analysis of ribcage deformation

Based on the X-ray CT data (Figure 8.20), mice that had the genetic disorder could be easily distinguished from mice that were healthy. Healthy mice had smooth continuous ribcages, and the spine had the original shape. Aga2

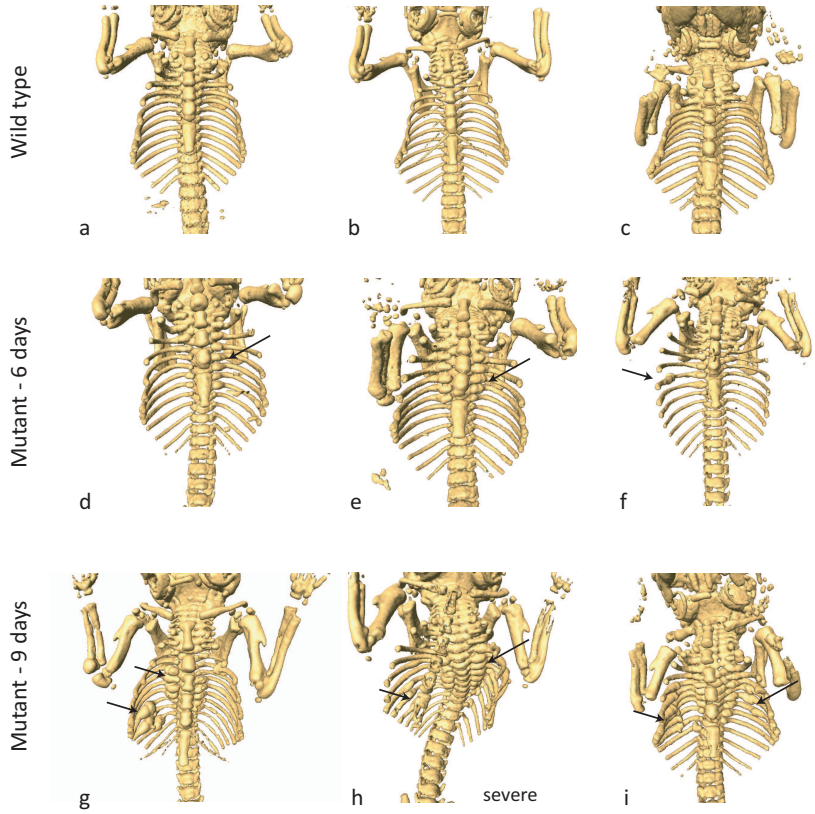

Figure 8.20: Overview of X-ray CT renderings of the ribcages of the imaged mice. Row 1) Healthy Aga2 mice. Row 2) Aga2 mutant mice at day 6. Row 3) Aga2 mutant mice at day 9.

mutant mice at day 6 showed primarily thickened areas next to the spine, in the upper part of the spine close to the head, and none or a small amount of areas of increased thickness in the remaining part of the ribcage. The areas of increased thickness were assumed to be the result of bones that have been broken and remodeled. Aga2 mutant mice at day 9 displayed increased bone thickness next to the spine, and several clusters of breakages spread over the ribcage. The mouse displayed in Figure 8.20h could be considered as the severe phenotype.

8.5.2 FMT-XCT Imaging results

FMT-XCT imaging was performed on 9-day old mice administered with a biphosphonate fluorescent agent (OsteoSense 680, exc: 680nm, em: 705nm, Perkin Elmer). Figure 8.21a depicts three consecutive transversal slices

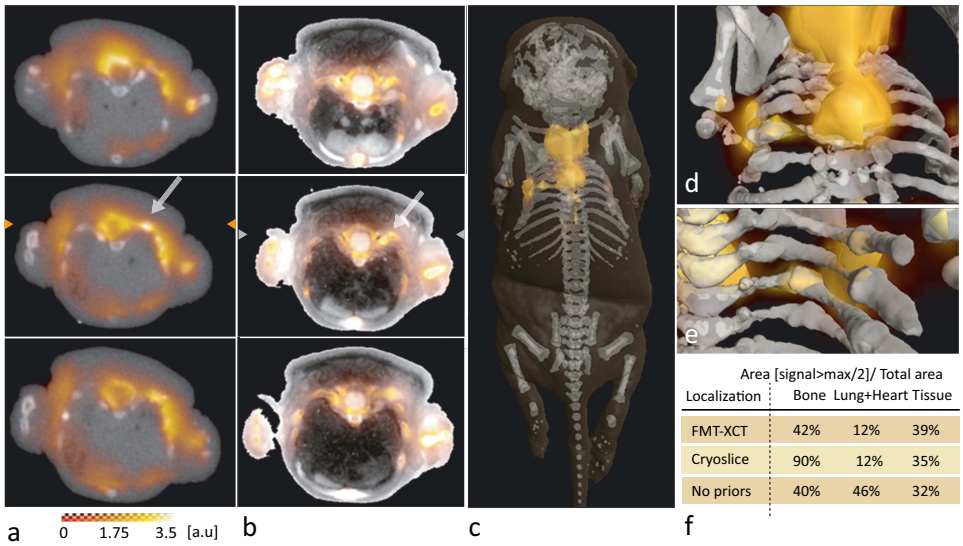

Figure 8.21: FMT-XCT reconstruction and validation results. a) Slices of FMT reconstruction overlaid on XCT slices. b) Validation cryoslices. c) Thresholded 3d rendering of bones and skin based on XCT data and fluorescence signal based on FMT reconstruction. d) Magnification of b without skin layer. e) View from the front. f) Quantification of signal localization in displayed FMT-XCT slice compared to cryoslice. (a.u, arbitrary units.)

of the FMT reconstruction overlaid on the corresponding XCT slices and Figure 8.21b shows corresponding cryoslicing validation images. The images capture in this case a fractured rib that is visible on the X-ray CT slice and it shows a congruent increased fluorescence intensity on the FMT reconstruction (indicated by arrows). The findings are confirmed by corresponding increased signals observed on the cryoslice. In a 3d rendering of the FMT reconstruction visualized together with the XCT data (Figure 8.21d), a signal congruent with the upper spine and thorax bones is visible and shown magnified on Figure 8.21e, showing the co-registration accuracy. The quantitative analysis of signal localization (Figure 8.21f) shows that artifacts in lung and heart region were decreased when prior information was used compared to stand-alone FMT reconstruction. By comparing the profiles over the cryoslice (Fig. 8.22a) and reconstruction (Figure 8.22b), we find that fluorescence peaks c1 and c2 in Figure 8.22a are observed in the profile over the FMT-XCT reconstruction (Figure 8.22b, f1 an f2, orange line) as well. In the reconstruction without priors (green line in Figure 8.22b), instead of two separate peaks we observed one broader peak that captures both signals.

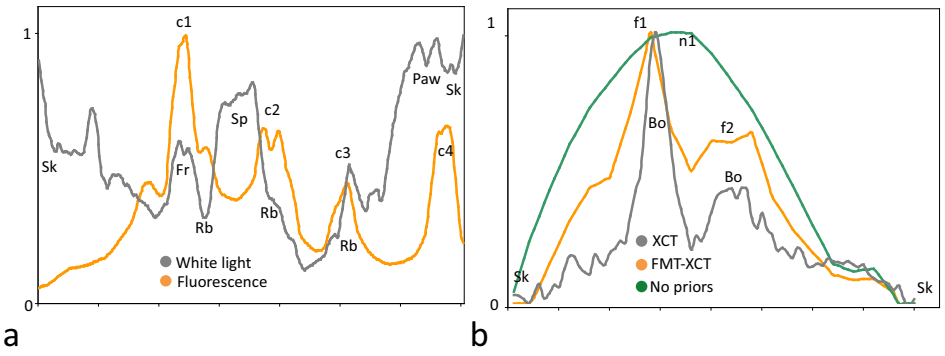

Figure 8.22: Quantification results. a) Profiles over cryoslice indicated with grey triangles in Figure 8.21b, c1-c4=fluorescence peaks in cryoslice, Sk=Skin, Fr=Fracture, Sp=Spine, Rb=Rib. b) Profiles over FMT-XCT reconstruction indicated with orange triangles in Figure 8.21a, f1-f2=fluorescence peaks in FMT-XCT reconstruction, n1=fluorescence peak in reconstruction without priors, Sk=Skin, Bo=Bone.

8.5.3 Summary and Conclusions

The free space implementation of FMT-XCT enabled in-vivo imaging of a very fragile mouse model, showing the versatility of hybrid FMT-XCT. In vivo imaging of this mouse model would be impossible in systems where the mice are placed in a vertical arrangement, or need to be compressed (see Chapter 1), because it would lead to lethal fractures. The X-ray CT renderings gave us detailed information on the location and amount of broken bones in the ribcage. The FMT-XCT reconstruction results demonstrated that significant imaging improvements are gained by the utilization of XCT information in the FMT inversion. We note that there have been no hard priors involved in the studies, i.e. there have been no assumptions on the presence of fluorescence on certain bone regions; instead only data based constraints have been employed. By comparison, stand-alone FMT shows significant inaccuracy compared to the signals seen by the hybrid FMT-XCT method.

8.6 Multiscale imaging of apoptosis after myocardial infarction

Heart failure causes a large amount of deaths each year. A better understanding of myocardial infarction (MI) could lead to improved diagnostic strategies and technology and new therapies [Leuschner and Nahrendorf, 2011]. In the study described below, we investigated the course of programmed cell death (apoptosis) after MI in mice in-vivo with FMT-XCT, and evaluated a potential treatment for vulnerable patients. Myocardial infarction has been imaged in the past using many different imaging modalities [Sosnovik et al., 2007]. This study is the first in which FMT-XCT is used to study MI. The study is ongoing, results are preliminary.

Following myocardial infarction, myocardial ischemia (insufficient blood supply) results in death of cardiomyocytes (muscle cells) via apoptosis (programmed cell death) and necrosis (cell death due to external factors). Consecutive myocardial remodeling can lead to progressive dilation of the left ventricle (LV, see Figure 8.23) and progressive heart failure. Apoptosis is the major form of cell death following myocardial ischemia [Abbate et al., 2006; Kajstura et al., 1996]. Apoptosis is a reversible process, and therefore a good target for therapy [Leuschner and Nahrendorf, 2011]. The myocardial injury induces an inflammatory response, involving several cell types that move from the spleen and bone marrow to the heart for repair [Cimini et al., 2007].

One of the cell types involved in the repair process are c-kit$^+$ cells that are recruited from the bone marrow [Cimini et al., 2007]. Cimini et al. compared wild type Kit$^{+/+}$ mice with mutant Kit^W/Kit^{Wv} mice in which c-kit$^+$ cell mobilization from the bone marrow was impaired, based on echocardiography and several ex-vivo analysis techniques. The hearts of the mutant mice showed more rapid ventricular dilation and heart failure after MI compared to wild type mice. After the mutants received transplantation of bone marrow cells from wild type Kit$^{+/+}$ mice by injection in the tail vein, the mutants showed similar characteristics compared to the wild type mice [Fazel et al., 2005].

In this study we investigated the progression of apoptosis after myocardial infarction over time, and the effect of treatment with c-kit$^+$ cardioprotective cells over time. The study was initiated by Moritz Wildgruber from

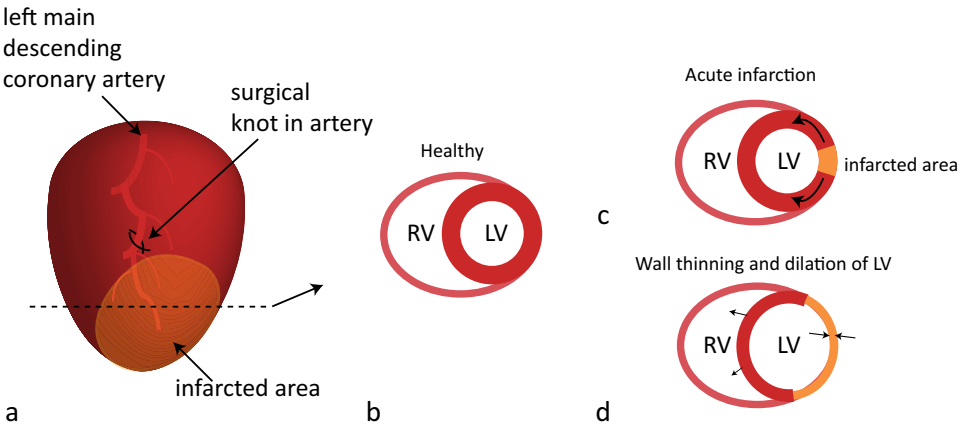

Figure 8.23: Heart schematic. a) 3d schematic, indicating the main artery that can be blocked by surgery to induce an infarct. b) Cross section of healthy heart with Right Ventricle (RV) and Left Ventricle (LV). c) Cross section of heart with infarcted region, which expands over time. d) Cross section of heart with signs of dilation and heart wall thinning after MI. Images inspired by [Abbate et al., 2006].

Klinikum Rechts der Isar.

8.6.1 Experimental setup

We investigated the progression of apoptosis after MI for three groups of mice (control mice, c-kit deficient mutant mice, and treated mutants as in [Cimini et al., 2007]), and over three time points (6h, 1d and 7d post infarction), see Table 8.3. We measured the mice in-vivo with FMT-XCT, and compared the quantitative signal over time and between groups. We expected a prolonged apoptosis rate for the mutants compared to the wild type mice, and the treated mutants were expected to show characteristics similar to the wild type mice. Ex-vivo validation was based on cryoslicing and histology. All mice were prepared by Moritz Wildgruber and Katja Kosanke from Klinikum Rechts der Isar. The surgical procedure consisted of ligation of the left anterior descending artery. First the chest wall was opened from the front, a knot was tied in one of the main arteries that provide blood to the heart and afterwards the incisions were closed. This procedure left signs of the knot inside the heart, and a scar on the chest wall [Ahn et al., 2004]. The group of control mice consisted of $\mathrm{Kit}^{+/+}$ mice. The second group of investigated mice were genetically modified $\mathrm{Kit}^{W}/\mathrm{Kit}^{Wv}$ mutant mice that lacked the c-kit gene that plays a decisive role in recovery after myocardial infarction, as described above. The last group that we

Table 8.3: Mouse models used for the study of myocardial infarction.

Mouse model	Description	Contrast agents
Kit $^{+/+}$	Control mice Black mice, surgically induced myocardial infarction	Annexin Vivo 750 (Perkin Elmer) ExiTron nano 12000 (Viscover)
Kit ^{W}/Kit ^{Wv}	Mutant mice White mice missing c-kit receptor, surgically induced myocardial infarction	
Reconstitued Kit ^{W}/Kit ^{Wv}	Mutant mice with treatment Mutant mice with transplanted cells from Kit $^{+/+}$ mice	

investigated were Kit^{W}/Kit^{Wv} mutant mice that were reconstituted with c-kit^{+} cardioprotective cells, by injecting cells from healthy mice into the tail vein. All mice underwent the described surgical procedure to induce a heart infarct. The fluorescent probe we used was Annexin Vivo 750 (Perkin Elmer), which targets apoptosis using the process shown in Figure 8.24. When a cell becomes apoptotic, it expresses phosphatidyl serine at the outer cell membrane. Annexin V is a binding protein with a high affinity for phosphatidyl serine, and can therefore be used to target apoptosis. We injected a CT contrast agent, described above in Section 3.3, in order to visualize the two heart chambers. Cryoslices showing the probe distribution of Annexin Vivo 750 in a healthy Kit$^{+/+}$ mouse are displayed in Figure 8.25, which shows that the background signal from Annexin Vivo consists of the presence of a low concentration of probe in the tissue surrounding the lung and in the heart wall, and a high concentration in the liver.

We used the hybrid FMT-XCT reconstruction methods described in Section 8.1 for all reconstructions. During detector selection areas with black skin were excluded for the Kit$^{+/+}$ mice, areas with scar tissue were excluded for all mice. The segmentation consisted of the regions: lung, bones, heart, liver and mixed tissue. Because the liver signal was quite strong we segmented the liver region as well. We set the weight for mixed tissue to 4, and calculated proportional weights for the remaining segments.

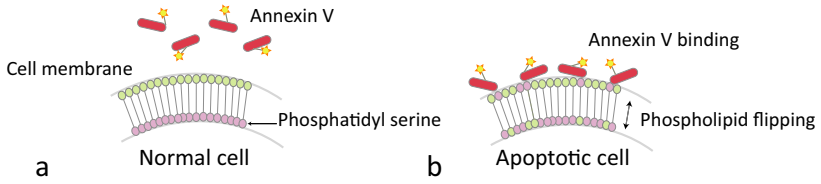

Figure 8.24: Annexin binding to apoptotic cells. a) Normal cell. b) Apoptotic cell with phosphatidyl serin flipping and Annexin V binding. (Based on http://www.rndsystems.com/product_detail_objectname_annexin_v_kits.aspx)

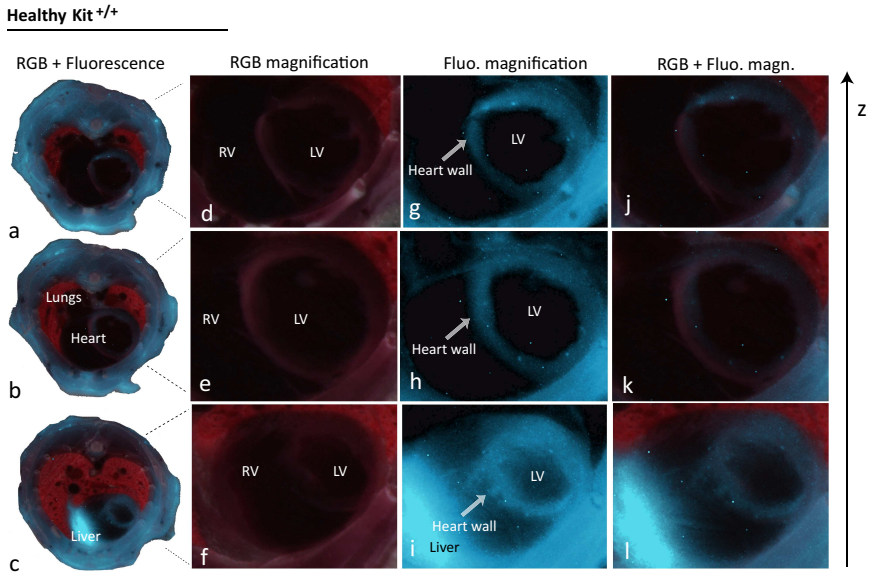

Figure 8.25: Cryoslices of Annexin Vivo 750 distribution in a healthy Kit$^{+/+}$ mouse (mouse m56). a-c) Fluorescence in cyan overlaid on RGB color slices. d-l) Magnification of heart area. d-f) RGB image. g-i) Fluorescence image. j-l) Overlay of fluorescence on RGB image. (RV=Right Ventricle, LV=Left Ventricle.)

8.6.2 Imaging results

We analyzed the imaging results obtained from in-vivo FMT-XCT reconstruction and ex-vivo cryoslicing for three time-points, 6h, 1d and 7d after myocardial infarction.

The first group we describe is the control group, which in this experiment consisted of regular Kit$^{+/+}$ mice with a surgically induced myocardial in-

farct.

Cryoslicing results of a mouse that was imaged 6 hours after the coronary artery was blocked by the surgical procedure described above is shown in Figure 8.26. The fluorescence signal includes a bright spot, close to the site of the surgery (Figure 8.26a). Additionally there is signal from the scar at the skin side of the mouse. The infarcted area is visible in the second and third cryoslice of the mouse (Figures 8.26b-c). The infarcted area is recognized as a very bright spot.

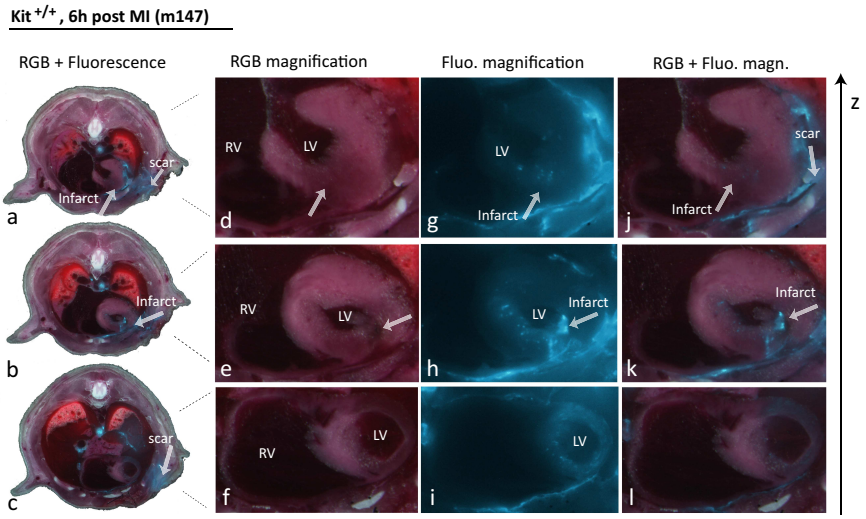

Figure 8.26: Cryoslices of Kit$^{+/+}$, 6h post MI (mouse m147). a-c) Fluorescence in cyan overlaid on RGB color slices. d-l) Magnification of heart area. d-f) RGB image. g-i) Fluorescence image. j-l) Overlay of fluorescence on RGB image. (RV=Right Ventricle, LV=Left Ventricle.)

Figure 8.27 shows cryoslicing results of a mouse that was imaged 1d after MI. Based on these images we can see that there is still a signal from the scar (Figure 8.27a). And the infarcted area is recognized as a spot which is less bright than the signal observed at 6h after MI (Figure 8.27b-c). In the last slice we observe a signal from the liver (Figure 8.27d).

Figure 8.28 shows cryoslicing results of a mouse 7d after MI. In these images we can see that the signal from the scar has further decreased in brightness. The infarcted area is now found much lower in the mouse, in a slice close to the liver. Furthermore the infarcted area is no longer a bright spot, but

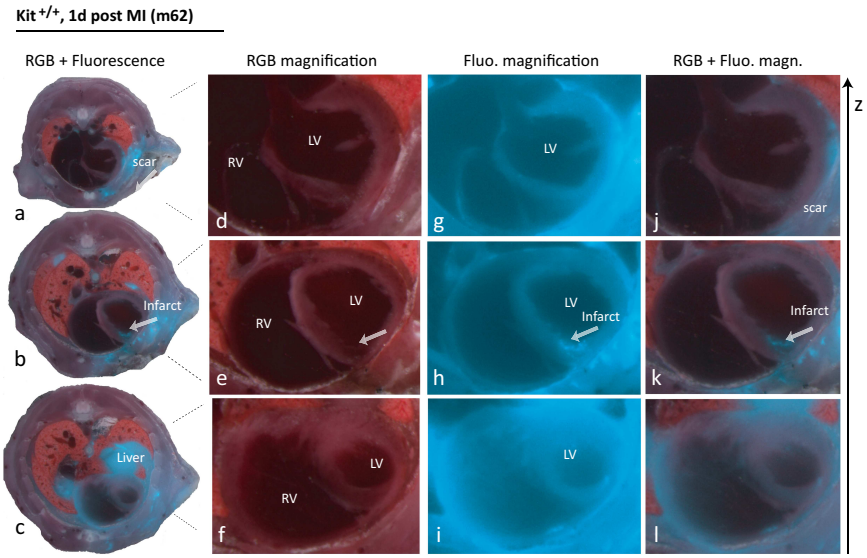

Figure 8.27: Cryoslices of Kit$^{+/+}$, 1d post MI (mouse m62). a-c) Fluorescence in cyan overlaid on RGB color slices. d-l) Magnification of heart area. d-f) RGB image. g-i) Fluorescence image. j-l) Overlay of fluorescence on RGB image. (RV=Right Ventricle, LV=Left Ventricle.)

forms a larger signal that has spread throughout the heart wall.

Multiscale imaging results for a mouse imaged 7d post MI are displayed in Figure 8.29. The first row shows results of the FMT-XCT reconstruction. The fluorescent signal is indicated in cyan. Slices are shown in three directions, transversal (axial), sagittal and coronal. Figures 8.29d-f show results of correlative cryoslicing. The infarcted area is indicated with an orange arrow. During cryoslicing we saved a slice for histological H&E staining. The slice saved for histology corresponds exactly with the slice imaged with the cryoslicing system. We took images of the stained slice using a zoom camera system that is being developed by Karin Radrich. In Figure 8.29e, we overlaid the picture of the H&E staining onto the RGB image taken with the cryoslicing system, showing the correspondence of anatomical features between the two images. In Figure 8.29f, we additionally included the fluorescence signal from the cryoslice. We observed that the fluorescence signal corresponds with the light purple area in the H&E stained slice, indicated with an orange arrow. The H&E slice is shown magnified in Figure 8.29g. The infarcted area is indicated. We took additional images of the slice using larger magnification settings (Figure 8.29h-k), which provide more details

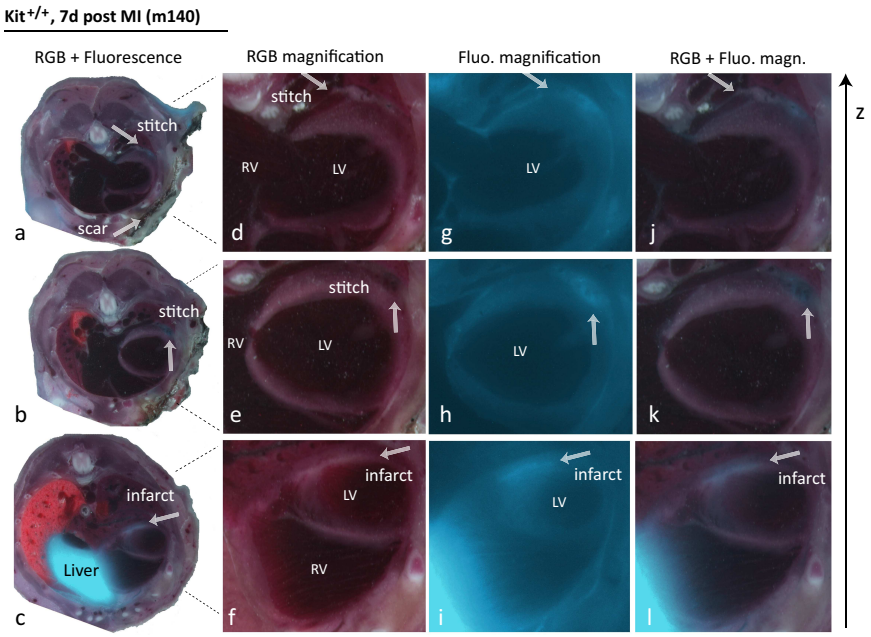

Figure 8.28: Cryoslices of Kit$^{+/+}$, 7d post MI (mouse m140). a-c) Fluorescence in cyan overlaid on RGB color slices. d-l) Magnification of heart area. d-f) RGB image. g-i) Fluorescence image. j-l) Overlay of fluorescence on RGB image. (RV=Right Ventricle, LV=Left Ventricle.)

on the structures present in the heart wall. This type of analysis could be used to improve the understanding of disease models on different scales, while providing the context of the bigger picture.

The second group of mice that we describe are the mutant Kit^{W}/Kit^{Wv} mice. These mice, as described above are compromised in their ability to recover from myocardial infarction. Figure 8.30 shows cryoslicing results of a mutant imaged 1d after myocardial infarction. The signal from the infarcted region is visible in all three displayed slices. The spot that indicates the infarct is very bright compared to the background signal. The signal is also much brighter than the signal from the scar.

Figure 8.31 shows cryoslicing results of a mutant imaged 7d after myocardial infarction. The signal from the infarcted region is visible in the lower slice. The signal is still brighter than the background signal, but is more spread throughout the heart wall.

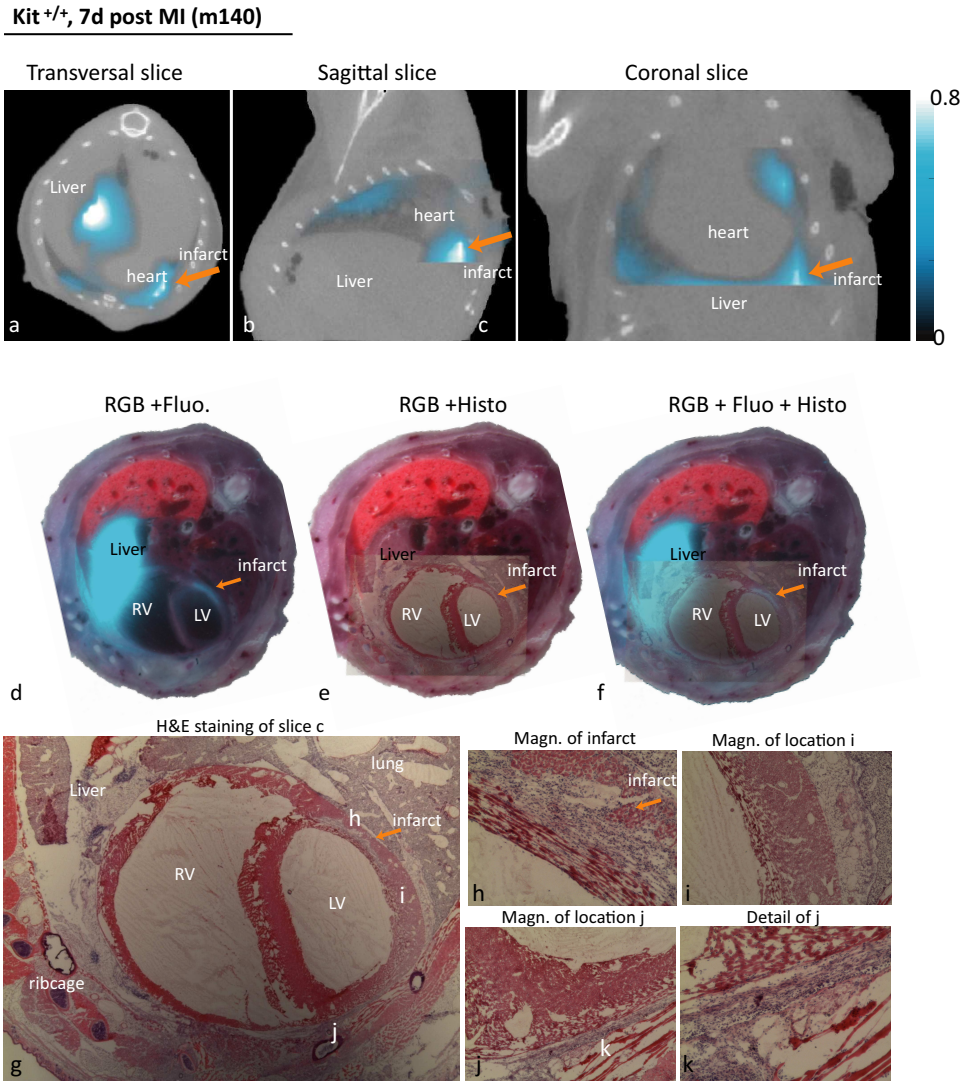

Figure 8.29: Multiscale imaging of Kit$^{+/+}$, 7d post MI (mouse m140). a-c) FMT-XCT reconstruction results. a) Transversal slice. b) Sagittal slice. c) Coronal slice. d-f) Cryoslicing and H&E composites. d) RGB cryoslice, overlaid with planar fluorescence signal in cyan. e) RGB cryoslice, overlaid with image of H&E staining of the same slice. f) Overlay of H&E staining on composite RGB and fluorescence cryoslice. g-k) images of H&E staining. g) Image of heart. h) Magnification of Figure g, location indicated by h in Figure g. i) Magnification of Figure g, location indicated by i in Figure g. j) Magnification of Figure g, location indicated by j in Figure g. k) Magnification of Figure j, location indicated by k in Figure j. (RV=Right Ventricle, LV=Left Ventricle.)

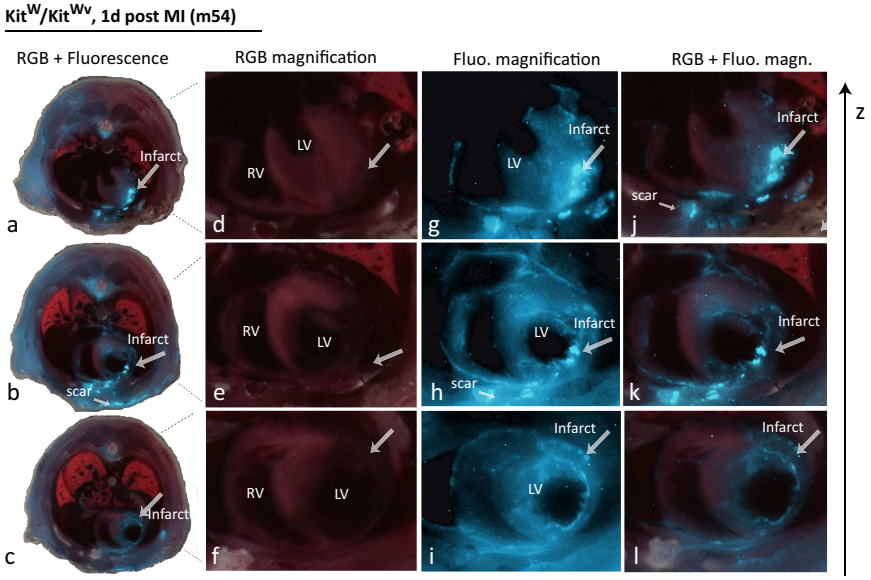

Figure 8.30: Cryoslices of mutant Kit^{W}/Kit^{Wv}, 1d post MI (mouse m54). a-c) Fluorescence in cyan overlaid on RGB color slices. d-l) Magnification of heart area. d-f) RGB image. g-i) Fluorescence image. j-l) Overlay of fluorescence on RGB image. (RV=Right Ventricle, LV=Left Ventricle.)

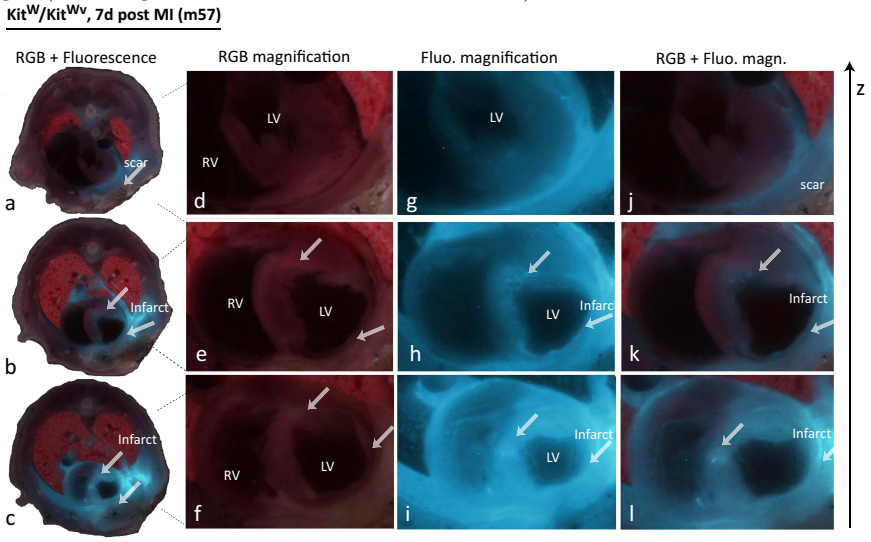

Figure 8.31: Cryoslices of mutant Kit^{W}/Kit^{Wv}, 7d post MI (mouse m57). a-c) Fluorescence in cyan overlaid on RGB color slices. d-l) Magnification of heart area. d-f) RGB image. g-i) Fluorescence image. j-l) Overlay of fluorescence on RGB image. (RV=Right Ventricle, LV=Left Ventricle.)

For the last group of mice, the treated mutants, we show cryoslicing results at 1d after myocardial infarction (Figure 8.32). The signal strength from the infarcted area is similar to the signal strength observed in the $Kit^{+/+}$ mice. It is approximately equal to the strength of the liver signal. This provides a complex reconstruction problem, however using the segmentation of the X-ray CT volume we were still able to provide a quantitative comparison of the reconstruction results.

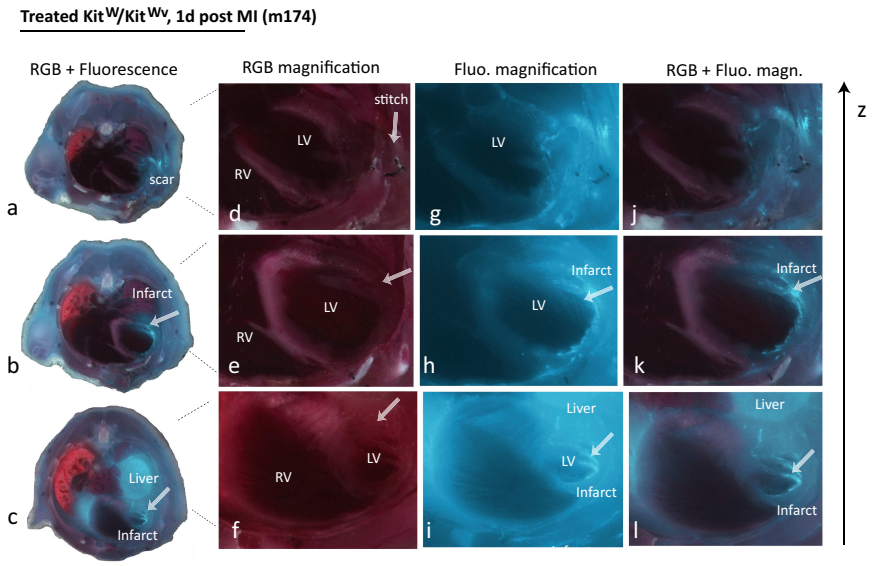

Figure 8.32: Cryoslices of mutant Kit^{W}/Kit^{Wv} with treatment, 1d post MI (mouse m174). a-c) Fluorescence in cyan overlaid on RGB color slices. d-l) Magnification of heart area. d-f) RGB image. g-i) Fluorescence image. j-l) Overlay of fluorescence on RGB image. (RV=Right Ventricle, LV=Left Ventricle.)

Figure 8.33 displays the results of FMT-XCT reconstructions for all groups. Figures 8.33a-i display transversal slices for one mouse per group and time point. The first row displays imaging results for the $Kit^{+/+}$ group. The signal evolves from a spot towards a broader signal. The second row displays the results for the Kit^{W}/Kit^{Wv} mutant mice, showing a similar development. The last row shows results from the mutant mice that received treatment. Figure 8.33j shows the number of mice for each group that were included in the analysis. In the ongoing study we will complete the groups by performing additional measurements. Figure 8.33 displays the quantitative analysis of the FMT-XCT reconstruction results. We used the segmentation of the X-

ray CT volume for the calculation of the ratio of maximum reconstructed value in the heart over average value reconstructed in the lung. We used a ratio and not an absolute measure because the mice had different sizes and skin color, which could affect the absolute reconstructed values. The signal generally decreases over time until the 7d time point. Overall, we can see from the quantitative analysis that the fluorescent signal in the mutant Kit^{W}/Kit^{Wv} mice is significantly higher than the signal observed both for the $Kit^{+/+}$ and treated mutants. The signal for the $Kit^{+/+}$ group and the treated mutants group is comparable.

8.6.3 Summary and conclusions

In this study, we showed imaging results of apoptosis after myocardial infarction. We imaged three groups of mice ($Kit^{+/+}$, mutant Kit^{W}/Kit^{Wv}, and treated Kit^{W}/Kit^{Wv}) at three time points (6h, 1d and 7d after MI). We analyzed the signal progression based on ex-vivo cryoslices and in-vivo FMT-XCT reconstruction results. We performed a multiscale analysis for a mouse that was imaged 7d post MI, using additional correlative H&E staining. A quantitative analysis of the FMT-XCT reconstruction results showed that Kit^{W}/Kit^{Wv} mutant mice develop a prolonged and increased apoptosis rate following myocardial infarction as measured in-vivo with FMT-XCT. Increased apoptosis of cardiomyoctes may be the beginning of a cascade leading to adverse myocardial remodeling and progressive heart failure. The results are preliminary and will be completed with additional experiments.

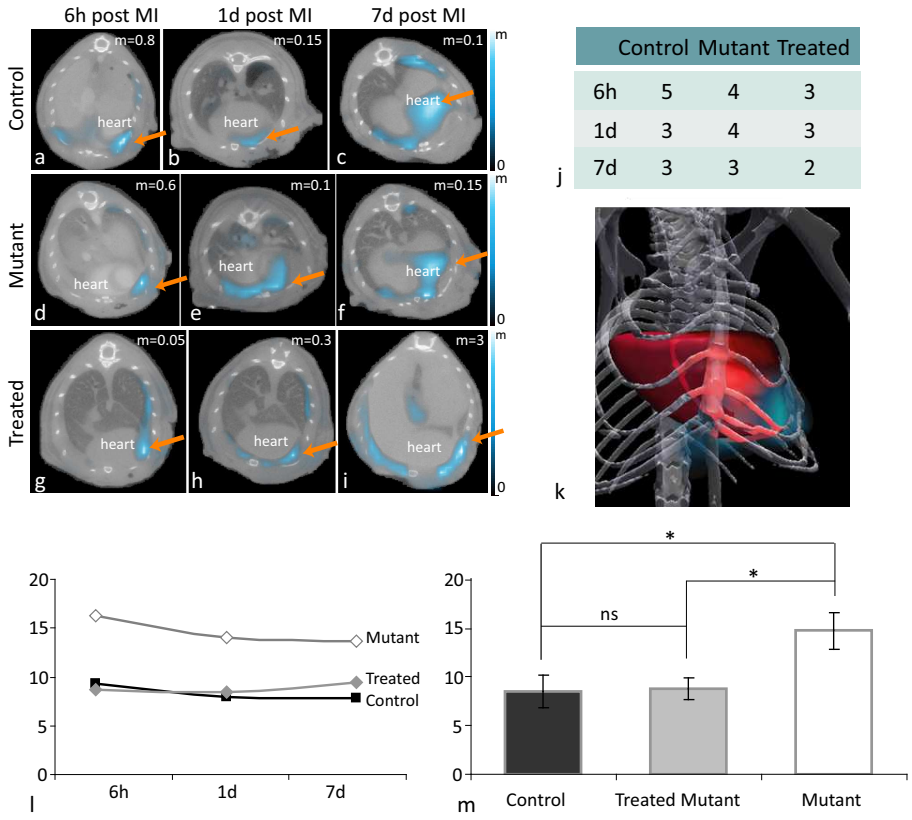

Figure 8.33: FMT-XCT reconstruction results for all groups. FMT-XCT reconstruction of a-c) $Kit^{+/+}$, d-f) Kit^{W}/Kit^{Wv} mutants, g-i) treated Kit^{W}/Kit^{Wv} mutants. j) Number of mice per group included in the analysis. k) 3d visualization of Annexin Vivo 750 signal, 7d post MI in Kit^{W}/Kit^{Wv} mutant. l) Quantitative analysis of reconstruction results. The average ratio per time group of the maximum in the heart divided by the average reconstructed value in the lung is plotted, assuming that the maximum indicates the infarcted area. m) Total average per group. The results of a statististical analysis of the difference between the averages is indicated (ns=not significant, $*$=P<0.05). Results are preliminary.

9

Conclusions and recommendations for future work

We developed hybrid FMT-XCT methods for the reconstruction of the fluorescence distribution in small animals. The methods employ the X-ray CT data to improve the FMT reconstruction results. We performed phantom, ex-vivo and in-vivo mouse experiments in parallel with the development of hybrid methods. Validation of the in-vivo results with ex-vivo planar fluorescence imaging played an important role during the development of the methods. In order to obtain an optimal reconstruction of the fluorescence distribution, we found that prior information should be used in both the calculation of the forward model of light propagation and during the inversion of the forward model. The X-ray CT information was additionally used for pre- and post-processing of the data and the reconstructed fluorescence distribution.

An important condition that we set when investigating different methods to improve the reconstruction of the fluorescence distribution was that the methods need to be stable, robust to imperfect experimental conditions, and able to provide reliable results for a wide range of applications. We used the LSQR method for inversion, a robust method with good numerical properties which facilitates the use of a regularization matrix. We developed a step-wise reconstruction method that leads to an estimation of the fluorescence distribution after two inversions of the forward model. For the second inversion we employed a structural regularization matrix that is shaped as a diagonal matrix, a matrix shape that has many advantages in terms of man-

ageability, speed and stability. We added prior information to the forward model in the form of optical properties, estimated per anatomical region by means of a variational analysis in which an optimal match was sought between cryoslicing validation images and FMT-XCT reconstruction. In our approach, the optical property estimates need to be optimized once for each anatomical region after which they are stored in a table. For subsequent studies the same optical properties can be assigned in a table-lookup manner, leading to a memory-efficient, but accurate method of including the light propagation properties in the calculation of the forward model. For increased sensitivity, we developed a data-driven method for the estimation of background fluorescence. By making several homogeneity assumptions with regard to the background fluorescence level, we could use a linear relationship between background fluorescence and normalized Born ratio values. Using the X-ray CT data, we could estimate the background fluorescence in a fully data-driven way.

The developed hybrid FMT-XCT methods have many advantages, as shown by the different animal studies that we performed. First, the study of a breast cancer model using multiple fluorescent probes showed the ability to discern different aspects of the tumor environment based on the imaging results obtained with the hybrid FMT-XCT methods and validation. A second advantage of FMT-XCT is that it is a non-invasive method that allows in-vivo monitoring of animals. Because the used near-infrared light is not harmful for the animals, mice could be imaged multiple times during disease progression. We performed several longitudinal studies, of a K-ras lung cancer model and a brain cancer model, in which we explored the ability to evaluate tumor growth over time. Third, hybrid FMT-XCT enables quantitative analysis. For example, in the myocardial infarction study we quantitatively analyzed the development of apoptosis after myocardial infarction, and correlated the results with histology. Finally, we have shown the versatility of the approach and the ability to resolve small targets in the study of a mouse model of Osteogenesis Imperfecta, which was a challenging study because the mice were very fragile and small. Overall, we demonstrated the improved imaging performance of hybrid FMT-XCT over stand-alone FMT, by making a direct quantitative comparison with the reconstruction result that would have been obtained with stand-alone FMT. The improvements are explicitly demonstrated for the breast cancer, K-ras and Osteogenesis Imperfecta study. These studies have shown that the de-

veloped methods are indeed applicable under a wide range of experimental conditions, and provide accurate and quantitative results.

The improvements obtained when using the developed hybrid reconstruction methods are not limited to application with hybrid FMT-XCT systems. Hybrid implementation of FMT with other modalities such as MRI, or using two separate systems with a good co-registration method could benefit from the hybrid reconstruction methods in the same way.

By combining FMT with XCT in one hybrid system we have overcome a major limitation of FMT, which is the lack of anatomical reference. Remaining limitations include limited resolution and limited penetration depth. The maximum resolution that can be obtained is about 8 mm. However, even though smaller targets can not be resolved at a higher resolution, they can be detected when the signal is very specific for the target. This can be achieved for example by using fluorescent proteins as was demonstrated in the brain cancer study. The penetration depth is limited, but enough to image small animals. Although the system we are using in this thesis can not be used to scan humans, results can be translated to the clinic in other ways, using for example multi-modality probes.

Several improvements of the hybrid FMT-XCT methods could be implemented in the future.

- In this research we used a rectangular source grid for FMT illumination, positioned based on white light images of the mouse. When the X-ray CT scan is performed before the acquisition setup of the FMT measurement, we could use the X-ray CT data to define a source pattern that exactly illuminates the anatomical region of interest. The source pattern could be further optimized based on a calculation of the model resolution.

- The structural information that we used in this research was a segmentation of the X-ray CT volume in large anatomical regions. The structural information could be refined when the information content of the X-ray CT data is increased, for example by using CT contrast agents. Furthermore, the resolution of the X-ray CT could be improved by taking into account the respiratory movement [Namati et al., 2006]. We assumed that the optical attenuation coefficients are constant over an anatomical region, and that the change in optical properties from

mouse to mouse is negligible. More detailed anatomical information could be used to improve the forward model by estimating a more detailed map of optical properties and it could also benefit the inversion by providing a basis for a more detailed structural penalty matrix.

- The X-ray CT information could be used in the forward model calculation to increase the resolution of the Finite Element Mesh in the region of interest [Joshi et al., 2004]. In the same way the resolution of the inversion could be made dependent on the X-ray CT volume. For example the voxel size along the boundary of the mouse could be increased while the voxels in the region of interest or in the region that is covered by a larger part of the measurements could be decreased.

- Several extensions of the implemented LSQR method are possible. For example a preconditioner could be included in order to increase stability or as an additional means to incorporate prior information [Calvetti and Somersalo, 2005]. The preconditioner could be used to incorporate data reliability information, when it is shaped as a vector that is related to the possible error in the data based on a noise estimate [Hyde et al., 2007].

- We could use the first inversion as initial guess for the second inversion using the Generalized LSQR algorithm [Reichel and Ye, 2006].

- In order to compensate for errors in the model, we could implement total least squares methods. The regularization term can be included in these methods by combining regularized total least squares with truncated total least squares and when this is combined with the LSQR algorithm this could lead to a memory efficient method [Hansen and O'Leary, 1998; Fierro et al., 1997; Golub et al., 1999; Beck and Ben-Tal, 2006].

In conclusion, we observed that the hybrid system not only allows anatomical localization of the fluorescence signal, but generally resulted in the most accurate FMT performance offered to-date. We expect that hybrid FMT-XCT will advance as an important imaging method that will be increasingly used for pre-clinical investigations. The hybrid FMT-XCT method with increased performance in terms of accuracy and contrast could find diverse biomedical applications in studying disease mechanisms and development of drugs and therapies.

List of Publications

Published papers

I. Angelique Ale, Vladimir Ermolayev, Eva Herzog, Christian Cohrs, Martin Hrabé De Angelis and Vasilis Ntziachristos, FMT-XCT: In vivo animal studies with hybrid fluorescence molecular tomography - X-ray computed tomography, Nature Methods, 2012.

II. Angelique Ale, Ralf B. Schulz, Athanasios Sarantopoulos and Vasilis Ntziachristos, Imaging performance of a hybrid x-ray computed tomography-fluorescence molecular tomography system using priors, Medical Physics, Volume 37, Issue 5, Pages 1976-1986, 2010, cover paper.

III. Ralf B. Schulz, Angelique Ale, Athanasios Sarantopoulos, Marcus Freyer, Eric Soehngen, Marta Zientkowska and Vasilis Ntziachristos, Hybrid System for Simultaneous Fluorescence and X-Ray Computed Tomography, IEEE Transactions on Medical Imaging, Volume 29, Issue 2, Pages 465-473, 2010.

IV. Marcus Freyer, Angelique B.F. Ale, Ralf B. Schulz, Marta Zientkowska, Karl Hans Englmeier and Vasilis Ntziachristos, Fast automatic segmentation of anatomical structures in x-ray computed tomography images to improve fluorescence molecular tomography reconstruction, Journal of Biomedical Optics, Volume 15, Issue 3, Pages 036006-1-8, 2010.

V. Andreas Buehler, Eva Herzog, Angelique Ale, Bryan A. Smith, Vasilis Ntziachristos and Daniel Razansky, High resolution tumor targetting in living mice by means of multispectral optoacoustic tomography (MSOT), EJNMMI Res. 2012 Apr 1;2:14.

VI. Thomas Pyka, Ralf B. Schulz, Angelique Ale and Vasilis Ntziachristos, Revisiting the normalized Born approximation: effects of scattering, Optics Letters, Volume 36, Issue 22, 2011.

VII. Lu Zhou, Birsen Yazici, Angelique B.F. Ale and Vasilis Ntziachristos, Performance evaluation of adaptive meshing algorithms for fluorescence diffuse optical tomography using experimental data, Optics Letters, Vol. 35, Issue 22, Pages 3727-3729, 2010.

Papers submitted or in preparation

VIII. Nikos Deliolanis, Angelique Ale, Stefan Morscher, Karin Schaefer, Daniel Razansky and Vasilis Ntziachristos, NIR reporter gene imaging with fluorescence and opto-acoustic tomography, submitted.

IX. Karin Radrich, Angelique Ale, Vladimir Ermolayev and Vasilis Ntziachristos, Improving limited-projection-angle Fluorescence Molecular Tomography using a co-registered X-ray Computed Tomography scan, submitted.

X. Vladimir Ermolayev, Angelique Ale, Athanasios Sarantopoulos and Vasilis Ntziachristos, Early recognition of lung cancer in K-ras mouse model using integrin targeted imaging, submitted.

XI. Angelique Ale, Frank Siebenhaar*, Katja Kosanke*, Michaela Aichler, Karin Radrich, Sina Heydrich, Matthias Schiemann, Tibor Schuster, Isabella Bielicki, Rickmer Braren, Peter B. Noel, Marcus Maurer, Axel K. Walch, Ernst J. Rummeny, Vasilis Ntziachristos and Moritz Wildgruber, Cardioprotective pluripotent c-kit+ cells attenuate apoptosis after acute myocardial infarction in mice - in-vivo assessment with Fluorescence Molecular Imaging, in preparation.

XII. Angelique Ale, Nikos Deliolanis, Vladimir Ermolayev and Vasilis Ntziachristos, Hybrid background fluorescence subtraction, in preparation.

XIII. Vladimir Ermolayev, Pouyan Mohajerani, Angelique Ale, Nikolaos Deliolanis, Susanta K. Sarkar, Marina Backer, Joseph M. Backer and Vasilis Ntziachristos, Non-invasive in vivo and ex vivo Imaging and Quantification

of scVEGF/Cy Distribution in Tumor Xenografts, in preparation.

XIV. Vladimir Ermolayev, Christian Cohrs, Pouyan Mohajerani, Angelique Ale, Martin Hrabé de Angelis and Vasilis Ntziachristos, Non-invasive in vivo imaging of internal hemorrhages in Aga2/+ mutant mice, in preparation.

Acknowledgements

I would like to thank professor Vasilis Ntziachristos for excellent ideas and supervision, and the great access to opportunities like speaking at conferences, publishing papers, and materializing research results.
Special thanks go to Maximilian Koch for his technical expertise and help with the hybrid FMT-XCT system. I would like to thank Athanasios Sarantopoulos for developing the cryoslicing system and help with experiments. I would like to thank Nikolaos Deliolanis for discussions, suggestions and cooperation. For the jointly carrying out of animal experiments, I would further like to thank Eva Herzog and Vladimir Ermolayev, cooperation partners Moritz Wildgruber, Katja Kosanke, Christian Cohrs and prof. Hrabé de Angelis. For lab assistance I would like to thank Claudia Mayerhofer, Sarah Glasl, Florian Jurgeleit and Uwe Klemm. I would like to thank Susanne Stern, Sylvia Weinzierl and Zsuzsi Öszi for help with the many forms and regulations.
I would like to thank all IBMI colleagues for drinks, barbecues and Oktoberfest parties. In particular I would like to thank Adrian Taruttis, Athanasios Sarantopoulos, Murad Omar, Karin Radrich, Niels Harlaar, Wendy Kelder, Nicolas Bezière, Rui Ma, Stephan Kellnberger, Saskia Björn, Andreas Murr and Claudia Mayerhofer for good times. I would like to thank my dear beloved friends George Themelis and Veronika Erben and wish them a lot of happiness with their starting family. I would like to thank the people I met during conferences for interesting discussions, in particular Frauke Alves, Vito Lorusso and Mark Niedre. Finally, I would like to thank Douwe Jan Bonthuis, family and friends for support, visits to Munich and unforgettable Biergarten experiences.

I wish the new colleagues working on the FMT-XCT project all the best with progress of their work.

A

Appendix

A.1 Cryoslices of adult K-ras

We display for reference a complete stack of cryoslices of an adult K-ras mouse. Figure A.1 shows planar RGB and planar fluorescence images overlaid on the RGB slices for the complete lung area. The lungs of the adult K-ras mouse showed several larger tumors (indicated by T) of about 1.2 mm diameter, and many smaller tumor nodules (indicated by t), distributed throughout the lung, often located close to the interface of lung and surrounding tissue.

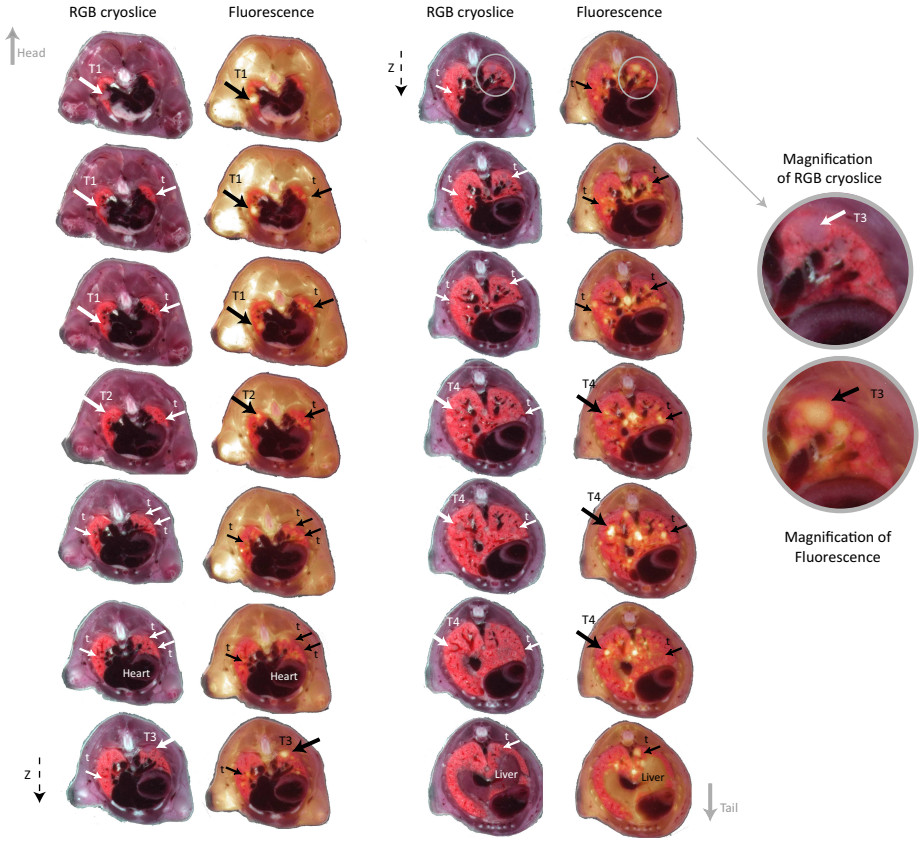

Figure A.1: Cryoslices of an adult K-ras mouse, arranged from head to tail. RGB color images displayed on the left, planar fluorescence images overlaid on RGB color images on the right. Arrows indicate tumors. T1-T4 indicate larger tumors, while t indicates smaller tumors. Heart and liver positions are indicated on two cryoslices. Fluorescence colormap scaled according to illumination times.

List of Figures

List of Tables

References

Abbate, A., Bussani, R., Amin, M. S., Vetrovec, G. W., and Baldi, A., 2006, Acute myocardial infarction and heart failure: role of apoptosis.: Int J Biochem Cell Biol, **38**, no. 11, 1834–1840.

Ahn, D., Cheng, L., Moon, C., Spurgeon, H., Lakatta, E. G., and Talan, M. I., Mar 2004, Induction of myocardial infarcts of a predictable size and location by branch pattern probability-assisted coronary ligation in c57bl/6 mice.: Am J Physiol Heart Circ Physiol, **286**, no. 3, H1201–H1207.

Alexandrakis, G., Rannou, F. R., and Chatziioannou, A. F., Sep 2005, Tomographic bioluminescence imaging by use of a combined optical-pet (opet) system: a computer simulation feasibility study.: Phys Med Biol, **50**, no. 17, 4225–4241.

Arridge, S. R., 1999, Optical tomography in medical imaging: Inverse Problems, **15**, no. 2, R41–R93.

Baeten, J., Niedre, M., Dunham, J., and Ntziachristos, V., 2007, Development of fluorescent materials for diffuse fluorescence tomography standards and phantoms: Optics Express, **15**, no. 14, 8681–8694.

Baeten, J., Haller, J., Shih, H., and Ntziachristos, V., Mar 2009, In vivo investigation of breast cancer progression by use of an internal control.: Neoplasia, **11**, no. 3, 220–227.

Bangerth, W., Hartmann, R., and Kanschat, G., 2007, Deal ii - a general-purpose object-oriented finite element library: ACM T. Math. Software, **33**, 1–24.

Barber, W. C., Lin, Y., Nalcioglu, O., Iwanczyk, J. S., Hartsough, N. E., and Gulsen, G., Feb 2010, Combined fluorescence and x-ray tomography

for quantitative in vivo detection of fluorophore.: Technol Cancer Res Treat, **9**, no. 1, 45–52.

Beck, A., and Ben-Tal, A., 2006, On the solution of the tikhonov regularization of the total least squares problem: SIAM J. Optim, **17**, 98–118.

Beek, J. F., van Staveren, H. J., Posthumus, P., Sterenborg, H. J., and van Gemert, M. J., Nov 1997, The optical properties of lung as a function of respiration.: Phys Med Biol, **42**, no. 11, 2263–2272.

Bockisch, A., Freudenberg, L. S., Schmidt, D., and Kuwert, T., 2009, Hybrid imaging by spect/ct and pet/ct: Proven outcomes in cancer imaging: Seminars in Nuclear Medicine, **39**, no. 4, 276–289.

Brooksby, B., Jiang, S. D., Dehghani, H., Pogue, B. W., Paulsen, K. D., Weaver, J., Kogel, C., and Poplack, S. P., 2005, Combining near-infrared tomography resonance imaging to study in vivo and magnetic resonance imaging to study in vivo breast tissue: implementation of a laplacian-type regularization to incorporate magnetic resonance structure: Journal of Biomedical Optics, **10**, no. 5.

Calvetti, D., and Somersalo, E., 2005, Priorconditioners for linear systems: Inverse Problems, **21**, 1397–1418.

Chang, J., Graber, H. L., and Barbour, R. L., 1997, Luminescence optical tomography of dense scattering media: J Opt Soc Am A Opt Image Sci Vis, **14**, no. 1, 288–99.

Chang, J., Graber, H. L., and Barbour, R. L., Jun 1998, Improved reconstruction algorithm for luminescence optical tomography when background lumiphore is present.: Appl Opt, **37**, no. 16, 3547–3552.

Cheong, W.-F., Prahl, S. A., and Welch, A. J., 1990, A review of the optical properties of biological tissues: IEEE Journal of Quantum Electronics, **26**, 12.

Cherry, S. R., 2009, Multimodality imaging: Beyond pet/ct and spect/ct: Seminars in Nuclear Medicine, **39**, no. 5, 348–353.

Cimini, M., Fazel, S., Zhuo, S., Xaymardan, M., Fujii, H., Weisel, R. D., and Li, R.-K., Sep 2007, c-kit dysfunction impairs myocardial healing after infarction.: Circulation, **116**, no. 11 Suppl, I77–I82.

Davis, S. C., Dehghani, H., Wang, J., Jiang, S., Pogue, B. W., and Paulsen, K. D., 2007, Image-guided diffuse optical fluorescence tomography implemented with laplacian-type regularization: Optics Express, **15**, no. 7, 4066–4082.

Davis, S. C., Pogue, B. W., Springett, R., Leussler, C., Mazurkewitz, P., Tuttle, S. B., Gibbs-Strauss, S. L., Jiang, S. S., Dehghani, H., and Paulsen, K. D., 2008, Magnetic resonance-coupled fluorescence tomography scanner for molecular imaging of tissue: Rev Sci Instrum, **79**, no. 6, 064302.

Deliolanis, N., Lasser, T., Niedre, M., Soubret, A., and Ntziachristos, V., 2006, In-vivo lung cancer imaging in mice using 360 degrees free-space fluorescence molecular tomography.: Conf Proc IEEE Eng Med Biol Soc, **1**, 2370–2372.

Deliolanis, N. C., Dunham, J., Wurdinger, T., Figueiredo, J.-L., Tannous, B. A., Bakhos, T., and Ntziachristos, V., 2009, In-vivo imaging of murine tumors using complete-angle projection fluorescence molecular tomography.: J Biomed Opt, **14**, no. 3, 030509.

Deliolanis, N. C., Wurdinger, T., Pike, L., Tannous, B. A., Breakefield, X. O., Weissleder, R., and Ntziachristos, V., 2011, In vivo tomographic imaging of red-shifted fluorescent proteins.: Biomed Opt Express, **2**, no. 4, 887–900.

Ebos, J. M. L., and Kerbel, R. S., Apr 2011, Antiangiogenic therapy: impact on invasion, disease progression, and metastasis.: Nat Rev Clin Oncol, **8**, no. 4, 210–221.

Fazel, S., Tang, G. H. L., Angoulvant, D., Cimini, M., Weisel, R. D., Li, R.-K., and Yau, T. M., Jun 2005, Current status of cellular therapy for ischemic heart disease.: Ann Thorac Surg, **79**, no. 6, S2238–S2247.

Fierro, R. D., Golub, G. H., Hansen, P. C., and O'Leary, D. P., 1997, Regularization by truncated total least squares: SIAM J. Sci. Comput., **18**, 1223–1241.

Filonov, G. S., Piatkevich, K. D., Ting, L.-M., Zhang, J., Kim, K., and Verkhusha, V. V., Aug 2011, Bright and stable near-infrared fluorescent protein for in vivo imaging.: Nat Biotechnol, **29**, no. 8, 757–761.

Flock, S. T., Jacques, S. L., Wilson, B. C., Star, W. M., and van Gemert, M. J., 1992, Optical properties of intralipid: a phantom medium for light propagation studies.: Lasers Surg Med, **12**, no. 5, 510–519.

Freudenberg, L. S., Rosenbaum, S. J., Beyer, T., Bockisch, A., and Antoch, G., 2007, Pet versus pet/ct dual-modality imaging in evaluation of lung cancer: Radiologic Clinics of North America, **45**, no. 4, 639–44.

Freyer, M., Ale, A. B. F., Schulz, R. B., Zientkowska, M., Englmeier, K. H., and Ntziachristos, V., 2010, Fast automatic segmentation of anatomical structures in x-ray computed tomography images to improve fluorescence molecular tomography reconstruction: Journal of Biomedical Optics, **15**, no. 3, 036006.

Gao, M., Lewis, G., Turner, G. M., Soubret, A., and Ntziachristos, V., Sep 2005, Effects of background fluorescence in fluorescence molecular tomography.: Appl Opt, **44**, no. 26, 5468–5474.

Giovanella, L., and Lucignani, G., 2010, Hybrid versus fusion imaging: are we moving forward judiciously?: European Journal of Nuclear Medicine and Molecular Imaging, **37**, no. 5, 973–979.

Golestani, R., Wu, C., Tio, R. A., Zeebregts, C. J., Petrov, A. D., Beekman, F. J., Dierckx, R. A. J. O., Boersma, H. H., and Slart, R. H. J. A., 2010, Small-animal spect and spect/ct: application in cardiovascular research: European Journal of Nuclear Medicine and Molecular Imaging, **37**, no. 9, 1766–1777.

Golub, G. H., Hansen, P. C., and O'Leary, D. P., 1999, Tikhonov regularization and total least squares: SIAM J. Matrix Anal. Appl., **21**, 185–194.

Graves, E. E., Ripoll, J., Weissleder, R., and Ntziachristos, V., May 2003, A submillimeter resolution fluorescence molecular imaging system for small animal imaging.: Med Phys, **30**, no. 5, 901–911.

Grimm, J., Kirsch, D. G., Windsor, S. D., Kim, C. F. B., Santiago, P. M., Ntziachristos, V., Jacks, T., and Weissleder, R., Oct 2005, Use of gene expression profiling to direct in vivo molecular imaging of lung cancer.: Proc Natl Acad Sci U S A, **102**, no. 40, 14404–14409.

Guven, M., Yazici, B., Intes, X., and Chance, B., 2005, Diffuse optical tomography with a priori anatomical information: Physics in Medicine and Biology, **50**, no. 12, 2837–2858.

Hadamard, J., 1923, Lectures on cauchy's problem in linear partial differential equations: Yale University Press, New Haven, CT.

Hanahan, D., and Weinberg, R. A., Mar 2011, Hallmarks of cancer: the next generation.: Cell, **144**, no. 5, 646–674.

Hansen, P. C., and O'Leary, D. P., 1998, Regularization algorithms based on total least squares: Technical Report, UM Computer Science Department; CS-TR-3684 UMIACS; UMIACS-TR-96-65.

Hansen, C., 1998, Rank-deficient and discrete ill-posed problems: SIAM, Philadelphia.

Heath, V. L., and Bicknell, R., Jul 2009, Anticancer strategies involving the vasculature.: Nat Rev Clin Oncol, **6**, no. 7, 395–404.

Hiltunen, P., Calvetti, D., and Somersalo, E., 2008, An adaptive smoothness regularization algorithm for optical tomography: Opt Express, **16**, no. 24, 19957–77.

Hood, J. D., and Cheresh, D. A., Feb 2002, Role of integrins in cell invasion and migration.: Nat Rev Cancer, **2**, no. 2, 91–100.

Huebner, K. H., 2001, The finite element method for engineers: Wiley-IEEE.

Hyde, D., Miller, E., Brooks, D. H., and Ntziachristos, V., Jul 2007, A statistical approach to inverting the born ratio.: IEEE Trans Med Imaging, **26**, no. 7, 893–905.

Hyde, D., de Kleine, R., MacLaurin, S. A., Miller, E., Brooks, D. H., Krucker, T., and Ntziachristos, V., 2009a, Hybrid fmt-ct imaging of amyloid-beta plaques in a murine alzheimer's disease model: Neuroimage, **44**, no. 4, 1304–1311.

——— 2009b, Performance dependence of hybrid x-ray computed tomography/fluorescence molecular tomography on the optical forward problem: Journal of the Optical Society of America a-Optics Image Science and Vision, **26**, no. 4, 919–923.

Hyde, D., Miller, E. L., Brooks, D. H., and Ntziachristos, V., Feb 2010, Data specific spatially varying regularization for multimodal fluorescence molecular tomography.: IEEE Trans Med Imaging, **29**, no. 2, 365–374.

Intes, X., Maloux, C., Guven, M., Yazici, B., and Chance, B., 2004, Diffuse optical tomography with physiological and spatial a priori constraints: Physics in Medicine and Biology, **49**, no. 12, N155–N163.

Jacques, S. L., and Pogue, B. W., 2008, Tutorial on diffuse light transport: Journal of Biomedical Optics, **13**, no. 4, 041302.

Johns, M., Giller, C., German, D., and Liu, H., Jun 2005, Determination of reduced scattering coefficient of biological tissue from a needle-like probe.: Opt Express, **13**, no. 13, 4828–4842.

Joshi, A., Bangerth, W., and Sevick-Muraca, E., Nov 2004, Adaptive finite element based tomography for fluorescence optical imaging in tissue.: Opt Express, **12**, no. 22, 5402–5417.

Joyce, J. A., and Pollard, J. W., Apr 2009, Microenvironmental regulation of metastasis.: Nat Rev Cancer, **9**, no. 4, 239–252.

Judenhofer, M. S., Wehrl, H. F., Newport, D. F., Catana, C., Siegel, S. B., Becker, M., Thielscher, A., Kneilling, M., Lichy, M. P., Eichner, M., Klingel, K., Reischl, G., Widmaier, S., Rocken, M., Nutt, R. E., Machulla, H. J., Uludag, K., Cherry, S. R., Claussen, C. D., and Pichler, B. J., 2008, Simultaneous pet-mri: a new approach for functional and morphological imaging: Nature Medicine, **14**, no. 4, 459–465.

Kajstura, J., Cheng, W., Reiss, K., Clark, W. A., Sonnenblick, E. H., Krajewski, S., Reed, J. C., Olivetti, G., and Anversa, P., Jan 1996, Apoptotic and necrotic myocyte cell deaths are independent contributing variables of infarct size in rats.: Lab Invest, **74**, no. 1, 86–107.

Kak, A. C., and Slaney, M., 2001, Principles of computerized tomographic imaging: SIAM.

Kaufmann, P. A., and Di Carli, M. F., 2009, Hybrid spect/ct and pet/ct imaging: The next step in noninvasive cardiac imaging: Seminars in Nuclear Medicine, **39**, no. 5, 341–347.

Kepshire, D., Mincu, N., Hutchins, M., Gruber, J., Dehghani, H., Hypnarowski, J., Leblond, F., Khayat, M., and Pogue, B. W., 2009a, A microcomputed tomography guided fluorescence tomography system for small animal molecular imaging: Rev Sci Instrum, **80**, no. 4, 043701.

——— 2009b, Imaging of glioma tumor with endogenous fluorescence tomography: Journal of Biomedical Optics, **14**, no. 3, 030501.

Kilmer, M. E., and O'Leary, D. P., 2001, Choosing regularization parameters in iterative methods for ill-posed problems: SIAM J. Matrix Anal. Appl., **22**, 1204–1221.

Kinahan, P. E., Hasegawa, B. H., and Beyer, T., 2003, X-ray-based attenuation correction for positron emission tomography/computed tomography scanners: Seminars in Nuclear Medicine, **33**, no. 3, 166–179.

Koenig, A., Herv, L., Josserand, V., Berger, M., Boutet, J., Silva, A. D., Dinten, J.-M., Pelti, P., Coll, J.-L., and Rizo, P., 2008, In vivo mice lung tumor follow-up with fluorescence diffuse optical tomography.: J Biomed Opt, **13**, no. 1, 011008.

Lasser, T., and Ntziachristos, V., Aug 2007, Optimization of 360 degrees projection fluorescence molecular tomography.: Med Image Anal, **11**, no. 4, 389–399.

Leblond, F., Davis, S. C., Valdes, P. A., and Pogue, B. W., 2010, Pre-clinical whole-body fluorescence imaging: Review of instruments, methods and applications: Journal of Photochemistry and Photobiology B-Biology, **98**, no. 1, 77–94.

Leuschner, F., and Nahrendorf, M., Mar 2011, Molecular imaging of coronary atherosclerosis and myocardial infarction: considerations for the bench and perspectives for the clinic.: Circ Res, **108**, no. 5, 593–606.

Levine, M., and Julian, J., 2009, Imaging pet-ct imaging in non-small-cell lung cancer: Nature Reviews Clinical Oncology, **6**, no. 11, 619–620.

Lin, Y. T., Yan, H., Nalcioglu, O., and Gulsen, G., 2009, Quantitative fluorescence tomography with functional and structural a priori information: Applied Optics, **48**, no. 7, 1328–1336.

Lisse, T. S., Thiele, F., Fuchs, H., Hans, W., Przemeck, G. K. H., Abe, K., Rathkolb, B., Quintanilla-Martinez, L., Hoelzlwimmer, G., Helfrich, M., Wolf, E., Ralston, S. H., and de Angelis, M. H., 2008, Er stress-mediated apoptosis in a new mouse model of osteogenesis imperfecta: Plos Genetics, **4**, no. 2, e7.

Matcher, S. J., Cope, M., and Delpy, D. T., 1997, In vivo measurements of the wavelength dependence of tissue-scattering coefficients between 760 and 900 nm measured with time-resolved spectroscopy: Applied Optics, **36**, no. 1, 386–396.

McCann, C. M., Waterman, P., Figueiredo, J.-L., Aikawa, E., Weissleder, R., and Chen, J. W., Apr 2009, Combined magnetic resonance and fluorescence imaging of the living mouse brain reveals glioma response to chemotherapy.: Neuroimage, **45**, no. 2, 360–369.

Milstein, A. B., Oh, S., Webb, K. J., Bouman, C. A., Zhang, Q., Boas, D. A., and Millane, R. P., 2003, Fluorescence optical diffusion tomography: Appl Opt, **42**, no. 16, 3081–94.

Molina, J. R., Yang, P., Cassivi, S. D., Schild, S. E., and Adjei, A. A., May 2008, Non-small cell lung cancer: epidemiology, risk factors, treatment, and survivorship.: Mayo Clin Proc, **83**, no. 5, 584–594.

Nahrendorf, M., Zhang, H. W., Hembrador, S., Panizzi, P., Sosnovik, D. E., Aikawa, E., Libby, P., Swirski, F. K., and Weissleder, R., 2008, Nanoparticle pet-ct imaging of macrophages in inflammatory atherosclerosis: Circulation, **117**, no. 3, 379–387.

Namati, E., Chon, D., Thiesse, J., Hoffman, E. A., de Ryk, J., Ross, A., and McLennan, G., Dec 2006, In vivo micro-ct lung imaging via a computer-controlled intermittent iso-pressure breath hold (iibh) technique.: Phys Med Biol, **51**, no. 23, 6061–6075.

Niedre, M. J., Turner, G. M., and Ntziachristos, V., 2006, Time-resolved imaging of optical coefficients through murine chest cavities: Journal of Biomedical Optics, **11**, no. 6, 064017.

Ntziachristos, V., and Weissleder, R., 2001, Experimental three-dimensional fluorescence reconstruction of diffuse media by use of a normalized born approximation: Optics Letters, **26**, no. 12, 893–895.

Ntziachristos, V., and Weissleder, R., May 2002, Charge-coupled-device based scanner for tomography of fluorescent near-infrared probes in turbid media.: Med Phys, **29**, no. 5, 803–809.

Ntziachristos, V., Yodh, A. G., Schnall, M., and Chance, B., 2000, Concurrent mri and diffuse optical tomography of breast after indocyanine green enhancement: Proc Natl Acad Sci U S A, **97**, no. 6, 2767–72.

Ntziachristos, V., Tung, C. H., Bremer, C., and Weissleder, R., 2002a, Fluorescence molecular tomography resolves protease activity in vivo: Nat Med, **8**, no. 7, 757–60.

——— 2002b, In vivo tomographic imaging of near-infrared fluorescent probes.: Mol Imaging, **1**, no. 2, 82–88.

Ntziachristos, V., Ripoll, J., Wang, L. H. V., and Weissleder, R., 2005, Looking and listening to light: the evolution of whole-body photonic imaging: Nature Biotechnology, **23**, no. 3, 313–320.

Ntziachristos, V., Leroy-Willig, A., and Tavitian, B., Eds., 2007, Textbook of in vivo imaging in vertebrates John Wiley & Sons Ltd.

Ntziachristos, V., 2006, Fluorescence molecular imaging.: Annu Rev Biomed Eng, **8**, 1–33.

Ntziachristos, V., Aug 2009, Optical imaging of molecular signatures in pulmonary inflammation.: Proc Am Thorac Soc, **6**, no. 5, 416–418.

Ntziachristos, V., 2010, Going deeper than microscopy: the optical imaging frontier in biology: Nature Methods, **7**, no. 8, 603–614.

O'Leary, M. A., Boas, D. A., Li, X. D., Chance, B., and Yodh, A. G., 1996, Fluorescence lifetime imaging in turbid media: Opt Lett, **21**, no. 2, 158–60.

Paige, C., and Saunders, M., 1982a, Lsqr: An algorithm for sparse linear equations and sparse least squares: ACM T. Math. Software, **8**, no. 1.

——— 1982b, Algorithm 583 lsqr: Sparse linear equations and least squares problems: ACM T. Math. Software, **8**, no. 2.

Patterson, M. S., Chance, B., and Wilson, B. C., Jun 1989, Time resolved reflectance and transmittance for the non-invasive measurement of tissue optical properties.: Appl Opt, **28**, no. 12, 2331–2336.

Pyka, T., Schulz, R., Ale, A., and Ntziachristos, V., 2011, Revisiting the normalized born approximation: in review.

Rauch, F., and Glorieux, F. H., Apr 2004, Osteogenesis imperfecta.: Lancet, **363**, no. 9418, 1377–1385.

Raymond, S. B., Kumar, A. T., Boas, D. A., and Bacskai, B. J., 2009, Optimal parameters for near infrared fluorescence imaging of amyloid plaques in alzheimer's disease mouse models: Phys Med Biol, **54**, no. 20, 6201–16.

Reichel, L., and Ye, Q., 2006, A generalized lsqr algorithm: Numerical Linear Algebra Applications.

Riklund, K. A., 2010, Pet/ct: nuclear medicine imaging in the future: Radiation Protection Dosimetry, **139**, no. 1-3, 8–11.

Salas, S. L., Hille, E., and Etgen, G. J., 2003, Calculus, one and several variables: J. Wiley & Sons, (lecture notes georgia tech linear algebra: numerical methods, version august 12, 2000, chapter 3) edition.

Sarantopoulos, A., Themelis, G., and Ntziachristos, V., Oct 2011, Imaging the bio-distribution of fluorescent probes using multispectral epi-illumination cryoslicing imaging.: Mol Imaging Biol, **13**, no. 5, 874–885.

Schulz, R. B., Ale, A., Sarantopoulos, A., Freyer, M., Soehngen, E., Zientkowska, M., and Ntziachristos, V., 2010, Hybrid system for simultaneous fluorescence and x-ray computed tomography: Ieee Transactions on Medical Imaging, **29**, no. 2, 465–473.

Shaner, N. C., Steinbach, P. A., and Tsien, R. Y., Dec 2005, A guide to choosing fluorescent proteins.: Nat Methods, **2**, no. 12, 905–909.

Siemann, D. W., 2011, Tumor microenvironment: John Wiley & Sons Ltd.

Sosnovik, D. E., Nahrendorf, M., Deliolanis, N., Novikov, M., Aikawa, E., Josephson, L., Rosenzweig, A., Weissleder, R., and Ntziachristos, V., Mar 2007, Fluorescence tomography and magnetic resonance imaging of myocardial macrophage infiltration in infarcted myocardium in vivo.: Circulation, **115**, no. 11, 1384–1391.

Soubret, A., and Ntziachristos, V., 2006, Fluorescence molecular tomography in the presence of background fluorescence: Physics in Medicine and Biology, **51**, no. 16, 3983–4001.

Soubret, A., Ripoll, J., and Ntziachristos, V., 2005, Accuracy of fluorescent tomography in the presence of heterogeneities: Study of the normalized born ratio: Ieee Transactions on Medical Imaging, **24**, no. 10, 1377–1386.

Srinivasan, S., Pogue, B. W., Dehghani, H., Jiang, S. D., Song, X. M., and Paulsen, K. D., 2004, Improved quantification of small objects in near-infrared diffuse optical tomography: Journal of Biomedical Optics, **9**, no. 6, 1161–1171.

Tan, Y. Y., and Jiang, H. B., 2008, Diffuse optical tomography guided quantitative fluorescence molecular tomography: Applied Optics, **47**, no. 12, 2011–2016.

Thiele, F., 2009, Development of an osteoblast cell culture system for functional characterization and comparative analyses of mouse models with bone phenotypes and systemic investigation of an osteogenesis imperfecta disease model: Ph.D. thesis, Technical University Munich.

Townsend, D. W., 2008, Dual-modality imaging: Combining anatomy and function: Journal of Nuclear Medicine, **49**, no. 6, 938–955.

Wehrl, H. F., Sauter, A. W., Judenhofer, M. S., and Pichler, B. J., 2010, Combined pet/mr imaging - technology and applications: Technology in Cancer Research & Treatment, **9**, no. 1, 5–20.

Weissleder, R., and Ntziachristos, V., 2003, Shedding light onto live molecular targers: Nature Medicine, **9**, no. 1, 123–128.

Weissleder, R., Tung, C. H., Mahmood, U., and Bogdanov, A., Apr 1999, In vivo imaging of tumors with protease-activated near-infrared fluorescent probes.: Nat Biotechnol, **17**, no. 4, 375–378.

Whiteside, T. L., Oct 2008, The tumor microenvironment and its role in promoting tumor growth.: Oncogene, **27**, no. 45, 5904–5912.

Yalavarthy, P. K., Pogue, B. W., Dehghani, H., Carpenter, C. M., Jiang, S. D., and Paulsen, K. D., 2007a, Structural information within regularization matrices improves near infrared diffuse optical tomography: Optics Express, **15**, no. 13, 8043–8058.

——— 2007b, Weight-matrix structured regularization provides optimal generalized least-squares estimate in diffuse optical tomography: Medical Physics, **34**, no. 6, 2085–2098.

Zhang, Q., Brukilacchio, T. J., Li, A., Stott, J. J., Chaves, T., Hillman, E., Wu, T., Chorlton, M., Rafferty, E., Moore, R. H., Kopans, D. B., and Boas, D. A., 2005, Coregistered tomographic x-ray and optical breast imaging: initial results: J Biomed Opt, **10**, no. 2, 024033.